

Search for Higgs boson pair-production in the $bb\tau\tau$
final state using proton-proton collisions at $\sqrt{s} = 13$
TeV data with the ATLAS detector

Zhiyuan Li

November 23, 2021



UNIVERSITY OF
LIVERPOOL



Contents

1	Introduction	1
2	Theory and Motivation	2
2.1	The Standard Model and the Higgs boson	2
2.2	Beyond the Standard Model	2
3	The ATLAS experiment at the Large Hadron Collider	3
3.1	The Large Hadron Collider	3
3.1.1	The LHC Accelerator Complex	3
3.1.2	Luminosity and pileup	5
3.1.3	Operation schedule	7
3.2	The ATLAS Detector	10
3.2.1	Coordinate system	12
3.2.2	Magnets	14
3.2.3	Inner detector	15
3.2.4	Calorimeter system	17
3.2.5	Muon Spectrometer	20
3.2.6	Trigger system	22
4	Data and Monte Carlo samples	23
5	Object Reconstruction	24
5.1	Track and vertex reconstruction	24
5.2	Electron	26
5.2.1	Reconstruction	26
5.2.2	Identification	28
5.3	Muon	29
5.3.1	Reconstruction	29
5.3.2	Identification	31
5.4	Jet	31
5.4.1	Reconstruction	31

5.4.2	Calibration	33
5.4.3	Identification of heavy quark flavoured jets	34
5.5	Hadronically decaying τ lepton	35
5.5.1	Reconstruction	36
5.5.2	Identification	37
5.5.3	Anti- τ_{had} definition	38
5.6	Missing transverse energy	39
5.7	Overlap removal	39
6	Charm jet mis-tagging calibration	41
6.1	Calibration methods for b jet and light jet	41
6.2	Calibration method for c jet	42
6.3	Data and Monte Carlo samples	44
6.4	Kinematic Likelihood Fitter	46
6.5	Maximising likelihood	47
6.6	Event selection	47
6.6.1	Standard selection	47
6.6.2	Low- p_T selection	48
6.6.3	High- p_T selection	49
6.6.4	Combined selection	51
6.7	Systematic uncertainties	52
6.7.1	Experimental uncertainties	52
6.7.2	Modelling uncertainties	53
6.8	Under-estimation of $t\bar{t} +$ Heavy flavour background	54
6.9	Results	55
6.9.1	Overview	55
6.9.2	b -tagging algorithms output distribution	56
6.9.3	Efficiencies and Scale Factors	59
7	Search for Higgs boson pair production in the $b\bar{b}\tau_{lep}^+\tau_{had}^-$channel	64
7.1	Data and Monte Carlo Simulation	65
7.1.1	Data samples	65
7.1.2	Simulated event samples	65
7.2	Event Selection	69
7.2.1	Trigger selection	69
7.2.2	Event preselection	70
7.2.3	Multivariate signal extraction	71
7.2.4	$Z +$ HF control region	74
7.3	Background estimation	75

7.3.1	Fake- τ backgrounds in the $\tau_{\text{lep}}\tau_{\text{had}}$ channel	76
7.4	Multivariate analysis	86
7.5	Systematic uncertainties	86
7.6	Results	86
8	Summary	95
A	Supplementary material for c jet calibration	109
A.1	Additional plots for kinematic variables	109
A.1.1	Standard selection	109
A.1.2	Low- p_{T} selection	115
A.2	High- p_{T} selection	118
A.3	Combined selection	125
A.4	Experimental uncertainties	132

Chapter 1

Introduction

Chapter 2

Theory and Motivation

2.1 The Standard Model and the Higgs boson

2.2 Beyond the Standard Model

Chapter 3

The ATLAS experiment at the Large Hadron Collider

3.1 The Large Hadron Collider

The Large Hadron Collider [1] is the world's largest and most powerful particle accelerator. It started operation in 2008 and retains its crucial role in the many accelerators in the world. The collider is located in a ring tunnel of circumference 26.7 km, which lies beneath the French-Swiss border near Geneva, with superconducting magnets along the tunnel to keep the particle beam in direction and a large number of accelerating structures to boost the beam to the desired energy. Inside the tunnel, *bunches* of up to 1.15×10^{11} protons travelling at close to the speed of light in opposite direction are collided 40 million times per second at four cross points, around which are positioned four main detectors: ATLAS (A Toroidal LHC ApparatuS) [2], CMS [3] (Compact Muon Solenoid), ALICE (A Large Ion Collider Experiment) [4] and LHCb (b stands for beauty) [5].

3.1.1 The LHC Accelerator Complex

The proton beams colliding in the LHC are designed to carry energy of the order of a few TeV. To reach such high energy, a series of acceleration is required for the beams before entering the LHC ring. The protons are supplied by the injector chain Linac 2 — Proton Synchrotron Booster (PSB) — Proton Synchrotron (PS) — Super Proton Synchrotron (SPS), as shown in Figure 3.1.

The protons are produced by stripping off the electrons from hydrogen gas in an electric field. Linac 2, the first accelerator in the chain, is a linear accelerator which accelerates the protons to an energy of 50 MeV. They then enter the PSB, which accelerates the protons to 1.4 GeV, followed by the PS, where they reach 25 GeV. The

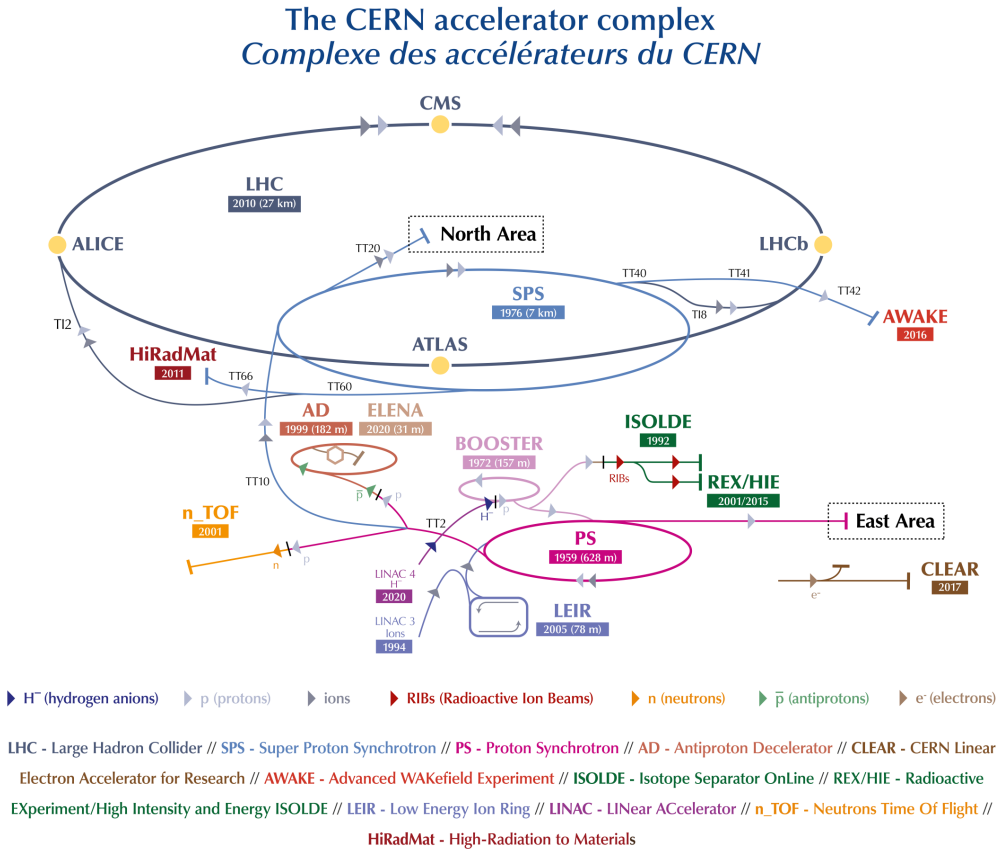


Figure 3.1: The LHC is the last ring (dark blue line) in a complex chain of particle accelerators. The smaller machines are used in a chain to help boost the particles to their final energies and provide beams to a whole set of smaller experiments.

series of radio frequency cavities in the PS splits the beam into discrete bunches of protons of 25 ns spacing. These bunches are then accelerated to 450 GeV in the SPS, from which they are finally injected into the beam pipes of the LHC. Each proton beam contains 2808 bunches, arranged in “trains” with 72 bunches each “carriage” of a gap of around 320 ns between each carriage. The beams are required to have well defined transverse and longitudinal emittance.

The beam pipes are kept at ultra-high vacuum, a vacuum thinner than interstellar void, maintained for 24 km of low-temperature section and 3 km of room-temperature section. For the low temperature section, the vacuum is achieved by pumping in 9000 m³ of cryogenic gas, which later will be condensed and adhered to the surface of the beampipe. For the room temperature section, the vacuum is achieved by use of non-evaporable getter (NEG) that absorbs residue gas particles when heated. More residue is absorbed by an ion pumper.

The beam pipes are installed in the existing tunnel that was constructed between

1984 and 1989 for the Large Electron-Positron Collider (LEP) [6], which lies between 45 m and 170 m below the surface on a plane inclined at 1.4% sloping towards the Léman lake. There are advantages and disadvantages for a proton-proton collider, compared to the electron-positron collider like LEP or proton-anti-proton collider. For the LHC, two rings are needed to accommodate the two counter-rotating beams, unlike particle-antiparticle colliders that can have both beams sharing the same phase space in a single ring, and therefore sharing the same magnets, same radio frequency cavities, etc. However, LHC is able to achieve very high collision energy which is not possible using electron-positron colliders, neither linear nor circular ones. This is due to the fact that in a circular electron collider, synchrotron radiation lost is proportional to the Lorentz factor $\gamma = E/m$ to the power of four, where E and m are the energy and mass of the particle, respectively. Since electrons are about 2000 times lighter than protons, synchrotron radiation lost is at the order of 10^{13} faster for electrons than for protons. For linear electron-positron collider, an extremely long acceleration section is required with current technologies, which makes it an impractical option. As for the proton-anti-proton collider, it would not be possible to achieve such high luminosity using anti-proton beams, since it is much more difficult to produce anti-protons than to produce protons. In addition, at high energies the proton anti-proton collider starts losing one of its advantages of having higher cross section, which is due to the quark sea and anti-quarks in protons become more “visible” at high energies (more details in the parton model section).

As explained above, two separate rings are required to accomodate the two beam pipes, while the internal diameter of the tunnel is only about 3.8 m. It's technically challenging to install them in such small space. LHC therefore adopted the twin-bore magnet design [7], as shown in Figure 3.2. It was first proposed by John Blewett at the Brookhaven laboratory in 1971 due to cost considerations [8], but in the case of the LHC the overriding reason for adopting this solution is the lack of space in the tunnel.

3.1.2 Luminosity and pileup

Luminosity is an important measure of a collider's performance. It comes closely to the number of events generated per second, given by:

$$N = \mathcal{L}\sigma,$$

where σ is the scattering cross section for the event under study and \mathcal{L} is the machine luminosity. For the cross-section, it is more common to use barn as the unit, where

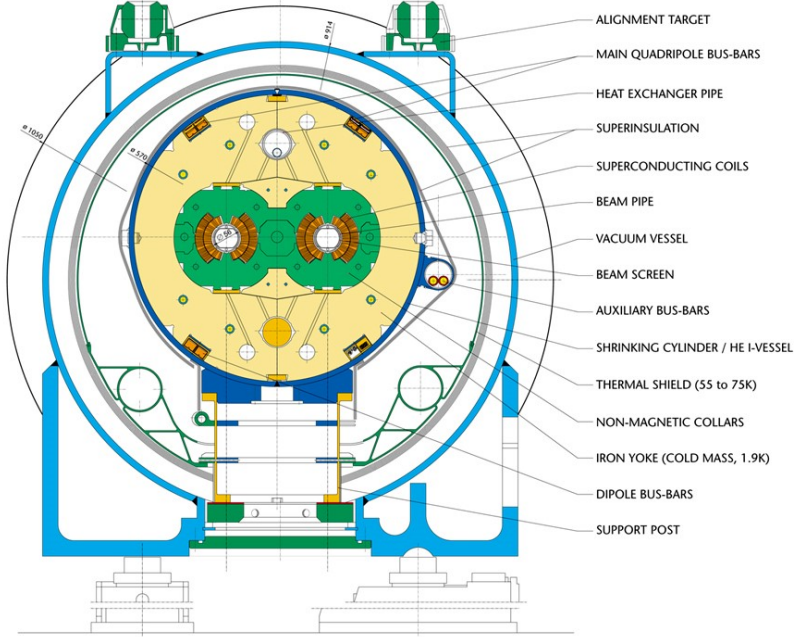


Figure 3.2: Double-bore magnet configuration of the LHC superconducting magnets [7].

$1\text{b} = 10^{-28} \text{ m}^2 = 10^{-24} \text{ cm}^2$, since particle interactions usually have very small cross-sections. The machine luminosity depends on the beam parameters and can be written for a Gaussian beam distribution as:

$$\mathcal{L} = \frac{N_b^2 n_b f_{rev} \gamma_r}{4\pi \epsilon_n \beta^*} F,$$

where N_b refers to the number of protons per bunch, n_b is number of bunches per beam, f_{rev} is the revolution frequency, γ_r is the relativistic gamma factor, ϵ_r is the normalised transverse beam emittance, β^* is the beta function at the collision point which describes the size of the beam, and F refers to the geometric luminosity reduction factor due to the crossing angle at the interaction point. While the instantaneous luminosity measures the rate of collisions (per unit cross-section), the total number of collisions (per unit cross-section) is measured by the integrated luminosity L , given by:

$$L = \int \mathcal{L} dt,$$

which is the integral of the instantaneous luminosity over time.

The two general purpose experiments, ATLAS and CMS are both aiming at a peak luminosity of $\mathcal{L} = 10^{34} \text{ cm}^2 \text{s}^{-1}$ for proton proton collision, which corresponds to about one billion pp collisions per second. The instantaneous luminosity was much improved at real-time operations reaching about twice the nominal (from 2015 to

2018) thanks to the effort of the LHC experts.

Another important parameter for the LHC experiments is the pileup, which is a measure of the number of inelastic pp interactions that occur per bunch crossing. Higher pileup gives more luminosity (for a fixed number of bunches) but makes physics analysis more difficult due to the signals in the detector from the additional interactions. The distribution of the recorded luminosity over the pileup is shown in Figure 3.3 for operations from 2015 to 2018 (Run 2), where the $\langle\mu\rangle$ stands for the mean number of interactions per bunch crossing. There are two main sources of pileup: in-time pileup and out-of-time pileup. The former refers to the additional proton-proton collisions occurring in the same bunch-crossing as the collision of interest. The latter refers to the additional proton-proton collisions occurring in bunch-crossings just before and after the collision of interest.

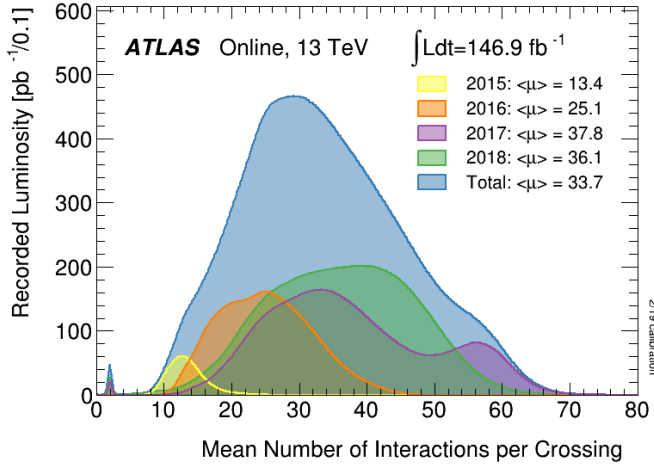


Figure 3.3: Shown is the luminosity-weighted distribution of the mean number of interactions per crossing for the data collected by the ATLAS from 2015 to 2018. All data recorded by ATLAS during stable beams is shown, and the integrated luminosity and the mean μ value are given in the figure.

3.1.3 Operation schedule

The LHC operation and shutdown schedule is shown in Figure 3.4. Following the downtime after an incident in one of the main dipole circuits during the first commissioning in 2008 [9], the operation restarted at lower beam energy to minimise the risk. Therefore, the first proton run (2010-2013) [10] was carried out at 3.5–4 TeV per beam (centre of mass energy 7–8 TeV). Furthermore, a bunch spacing of 50 ns was used instead of the nominal 25 ns, with peak luminosity of $0.8 \times 10^{34} \text{ cm}^{-2}\text{s}^{-1}$, and pileup larger than nominal.

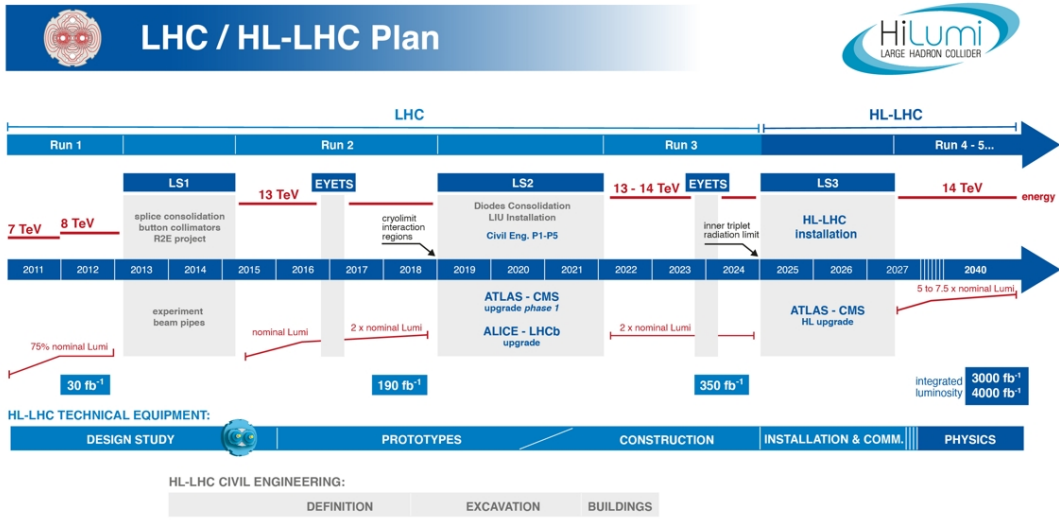


Figure 3.4: LHC operation schedule and luminosity targets.

In Run 1, the LHC delivered about 30 fb^{-1} of proton data and important physics results, most notably the discovery of the Higgs boson [11, 12]. Run 1 was followed by a long shutdown (LS1, 2013–2014) with a large number of consolidation and upgrade activities [13]. The bus-bar splices between the superconducting magnets were improved, in order to make sure that the LHC could operate at higher energy without risk of repeating the 2008 incident.

Run 2 (2016-2018) was carried out at 6.5 TeV per beam (center of mass energy 13 TeV) [14]. As shown in Figure 3.5, out of the 156 fb^{-1} of data LHC has delivered at 13 TeV centre of mass energy, the ATLAS detector has recorded 147 fb^{-1} and 139 fb^{-1} of data is certified to be good quality data. The 156 fb^{-1} data accounts for the luminosity delivered from the start of stable beams until the LHC requests ATLAS to put the detector in a safe standby mode to allow a beam dump or beam studies. The recorded luminosity is slightly smaller than the delivered luminosity, due to the inefficiency of the Data Acquisition and the so called “warm start”: when the stable beam flag is raised, the tracking detectors undergo a ramp of the high-voltage and, for the pixel system, turning on the pre-amplifiers. More details of the ATLAS detector can be found in the following sections. The recorded data is checked carefully to exclude possible hardware or software issues. This is achieved by monitoring detector-level quantities and reconstructed collision event characteristics at key stages of the data processing chain. This procedure led to high efficiency of good quality data: 95.6% [15].

In this thesis the 139 fb^{-1} data recorded by the ATLAS detector of Run 2 is used.

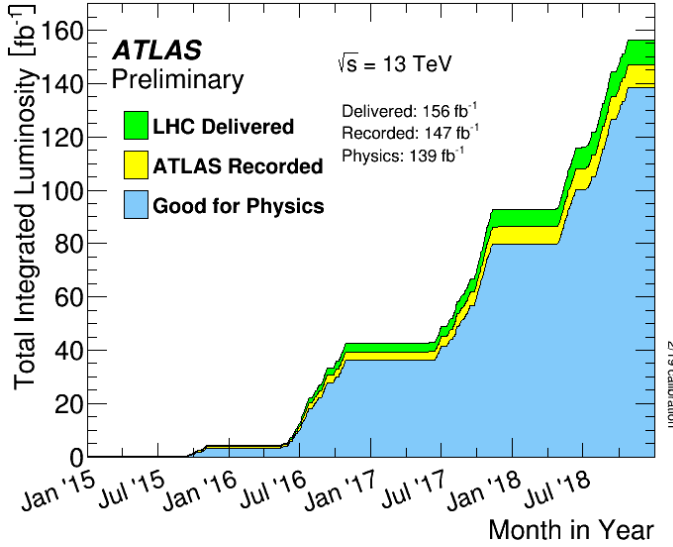


Figure 3.5: Cumulative luminosity versus time delivered to ATLAS (green), recorded by ATLAS (yellow), and certified to be good quality data (blue) during stable beams for pp collisions at 13 TeV centre-of-mass energy in Run 2.

The nominal bunch spacing of 25 ns was used, with slightly less bunches (2500) per beam. The LHC experts have continually improved the running scenario to increase the luminosity, and during Run 2 the luminosity surpassed the designed luminosity by a factor of 2. As well as improving the instantaneous luminosity, the availability of the machine was dramatically improved during Run 2 which is an important factor enabling the high efficiency of good quality data as mentioned above. During Run 2, the machine was providing physics collisions during 50% of the allocated physics time, which is very impressive for a super conducting collider.

The operation of CERN’s accelerators is subject to scheduled shutdowns to allow important repair and upgrade work to take place. The present shutdown, LS2, is devoted to preparations for Run 3 of the LHC, which will have an integrated luminosity equal to the two previous runs combined, and for the High-Luminosity LHC (HL-LHC), the successor to the LHC, which will begin operation at the end of 2027, and eventually generate 10 times the integrated luminosity of all Run 1, 2 and 3 combined!

The LS2 schedule has had to be modified due to the COVID-19 pandemic, which the new schedule anticipates that the first test beams will circulate in the LHC at the end of September 2021, four months later than the date planned before the COVID-19 crisis, to give the LHC’s main experiments – ATLAS, CMS, ALICE and LHCb – time to prepare their own upgrade. Run 3 of the LHC will begin at the start of March 2022. The third long shutdown (LS3) will begin at the start of 2025 and end

in mid-2027. This is when the equipment for the HL-LHC and its experiments will be installed.

3.2 The ATLAS Detector

ATLAS is one of the two general purpose detectors built for probing proton-proton collision. This detector represents the work of a large collaboration of several thousand physicists, engineers, technicians, and students over a period of fifteen years of dedicated design, development, fabrication, and installation. The overall layout of the detector is shown in Figure 3.6 [2]. It has the shape of a cylinder, 46 m long, 25 m in diameter, and sits in a cavern 100 m below ground. The ATLAS detector weighs 7000 tonnes, similar to the weight of the Eiffel Tower. The detector itself is a many-layered instrument designed to detect some of most energetic particles ever created on earth. It consists of six different detecting subsystems wrapped concentrically in layers around the collision point of nearly 4π solid angle coverage to record the trajectory, momentum, and energy of particles, allowing them to be individually identified and measured. These six subsystems are the pixel detector [16], the semiconductor tracker (SCT) [17], the transition radiation tracker (TRT) [17], the electromagnetic (EM) calorimeter [18], the hadronic calorimeter [19] and the muon spectrometer (MS) [20]. The first three sub-detectors are collectively known as the inner detector (ID), described in section 3.2.3, and it is used for tracking charged particles. The electromagnetic and the hadronic calorimeter, described in section 3.2.4, are responsible for measuring the energies of the electromagnetic and hadronic particles respectively. The MS, described in section 3.2.5, is a unique sub-detector used for measuring the momentum of muons leaving the calorimeters.

A huge magnet system bends the paths of the charged particles so that their momenta can be measured as precisely as possible.

The high interaction rates, radiation doses, particle multiplicities and energies, as well as the requirements for precision measurements have set stringent standards on the design of the ATLAS detector. Therefore the ATLAS detector is designed to fufiled the following requirements:

- Fast, radiation-resistant electronics and sensor elements and high detector granularity. This is due to the high frequency of collisions, high particle fluxes and high radiation environment of the detector.
- Large acceptance in polar angle with almost full azimuthal angle coverage, due to the geometry of the detector (more details in section 3.2.1).

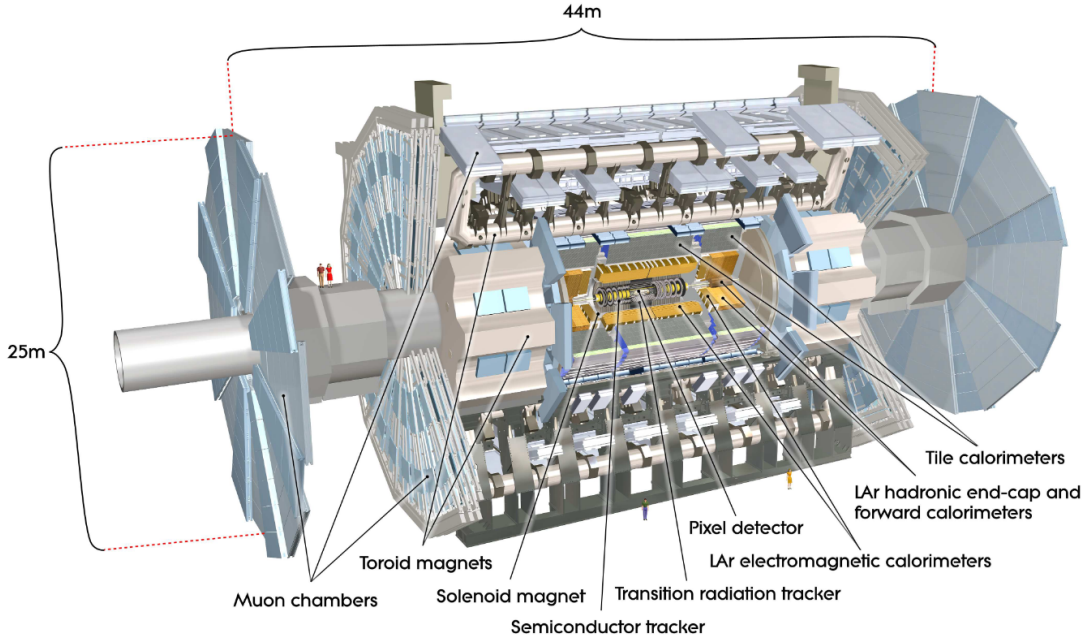


Figure 3.6: Cut-away view of the ATLAS detector. The dimensions of the detector are 25 m in height and 44 m in length. The overall weight of the detector is approximately 7000 tonnes. The figure is taken from reference [2].

- Good energy resolution calorimetry, as required to enable accurate physical object reconstruction. The high resolution of energy can be obtained with very good electromagnetic calorimetry for electron and photon identification and measurements, complemented by full-coverage hadronic calorimetry for accurate jet and missing transverse energy measurements.
- Tracking of precision in the ID, as required to provide high momentum resolution and to allow the reconstruction of secondary vertices to identify b -hadrons and τ -leptons.
- Good muon identification and momentum resolution over a wide range of momenta and the ability to determine unambiguously the charge of high- p_T muons in the muon spectrometer.
- Trigger system with high efficiency on low p_T objects with sufficient background rejection, which is a prerequisite to achieve an acceptable trigger rate for most physics processes of interest.

The main performance goals of the detector are listed in Table 3.1.

Detector component	Required resolution	η coverage	
		Measurement	Trigger
Tracking	$\sigma_{p_T}/p_T = 0.05\% p_T \oplus 1\%$	± 2.5	None
EM calorimetry	$\sigma_E/E = 10\% /E \oplus 0.7\%$	± 3.2	± 2.5
Hadronic calorimetry barrel and end-cap forward	$\sigma_E/E = 50\% /E \oplus 3\%$	± 3.2	± 3.2
	$\sigma_E/E = 100\% /E \oplus 10\%$	$3.1 < \eta < 4.9$	$3.1 < \eta < 4.9$
Muon spectrometer	$\sigma_{p_T}/p_T = 10\% \text{ at } p_T = 1 \text{ TeV}$	± 2.7	± 2.4

Table 3.1: General performance goals of the ATLAS detector. The units for energy of the particle, E and transverse momentum, p_T (detailed definition in section 3.2.1) are in GeV [2]. Note that, for high- p_T muons, the muon-spectrometer performance is independent of the inner-detector system.

3.2.1 Coordinate system

The ATLAS coordinate system is a right-handed Cartesian system with the nominal interaction point defined as the origin of the coordinate system, while the beam direction defines the z -axis and the x - y plane is transverse to the beam direction. The positive x -axis is defined as pointing from the interaction point to the centre of the LHC ring and the positive y -axis is defined as pointing upwards, as shown in Figure 3.7.

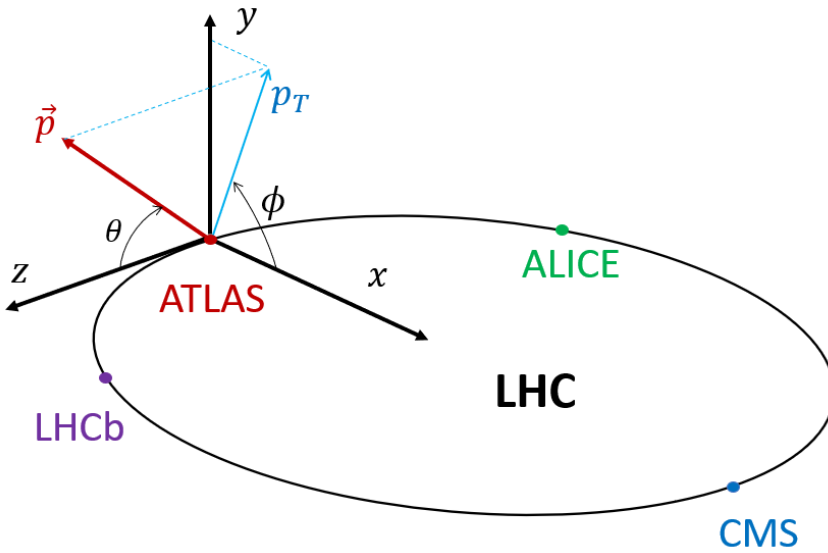


Figure 3.7: Illustration of the coordinate system used at the ATLAS experiment in the geographical context of the LHC.

The azimuthal angle ϕ is measured as usual around the beam axis, and the polar angle θ is the angle from the beam axis. In high energy physics, it's more common

to use the pseudorapidity instead of the polar angle θ , defined as:

$$\eta = -\ln \tan(\theta/2).$$

In the case of highly relativistic particles (which is the common case in high energy physics), the pseudorapidity approaches the rapidity,

$$y = 1/2 \ln[(E + p_z)/(E - p_z)],$$

where E is the energy of the particle, m is its mass and p_z is the momentum along the z -axis. There are two main reasons for using pseudorapidity rather than the polar angle θ nor the rapidity. The reason for using pseudorapidity but not θ is that the rapidity is invariant under Lorentz transformation, while capturing the characteristic of the particle direction of travel: $y \rightarrow \pm\infty$ when the particle is travelling close to the beam pipe (positive for along the beam pipe, negative for the opposite direction) and $y \rightarrow 0$ when p_z is small. The reason for using pseudorapidity but not rapidity is that due to the limited angle coverage of the detector, it's usually hard to determine the total energy and the momentum along the z -axis, especially when the direction of the particles are close to the beam pipe. While the pseudorapidity is determined only by the polar angle, which is much easier and faster to compute. Another commonly used variable, transverse momentum p_T , is defined as the momentum of a particle transverse to the beam direction (z -direction):

$$\vec{p}_T = (p_x, p_y).$$

The reason for using transverse momentum is that, because the partons that make up a proton share the momentum, the initial longitudinal momentum is unknown; we do know, however, that the initial transverse momentum was zero. And hence we can look for the missing transverse momentum, defined as

$$\vec{E}_T^{miss} = - \sum_i \vec{p}_{Ti}$$

for visible particles i , where E_T^{miss} is the magnitude of \vec{E}_T^{miss} (Confusingly E_T^{miss} is commonly called missing transverse energy or MET. Missing transverse energy is equivalent to missing transverse momentum only if the missing particle(s) were massless.). Finally, the distance ΔR in the pseudorapidity-azimuthal angle space is defined as:

$$\Delta R = \sqrt{\Delta\eta^2 + \Delta\phi^2},$$

where R is the radial distance from the particle position to the interaction vertex.

3.2.2 Magnets

ATLAS has a unique hybrid system of four large superconducting magnets [21]. This magnetic system is 22 m in diameter and 26 m in length, with a stored energy of 1.6 GJ. Figure 3.8 shows the real scale of the magnets system compared to a person. Figure 3.6 shows the general layout, the four main layers of detectors and the four superconducting magnets which provide the magnetic field over a volume of approximately 12000 m³.



Figure 3.8: A picture showing the real size magnets compared to a person.

The spatial arrangement of the coil windings is shown in Figure 3.9. The ATLAS magnet system consists of two parts:

- a solenoid, which is aligned on the beam axis and provides a 2 T axial magnetic field in the z -direction for the ID. Because the magnet is located in front of the EM calorimeter, it is imperative to minimise possible interactions between the magnet and the particles being studied. This is achieved by embedding over 9 km of niobium-titanium superconductor wires into strengthened, pure aluminum strips, which is capable to provide such powerful magnetic field in just 4.5 cm thickness.
- A barrel toroid and two end-cap toroids, which produce a toroidal magnetic field of approximately 0.5 T and 1 T for the muon detectors in the central and end-cap regions, respectively. The barrel toroid generates the magnetic field

in the central zone of the muon spectrometer, along the tangential direction of the circumferences centered on the z -axis (ϕ direction). The end-cap toroids are two smaller toroids designed to provide the magnetic field in the forward areas of the muon spectrometer. This magnet configuration provides a field is mostly orthogonal to the muon trajectories.

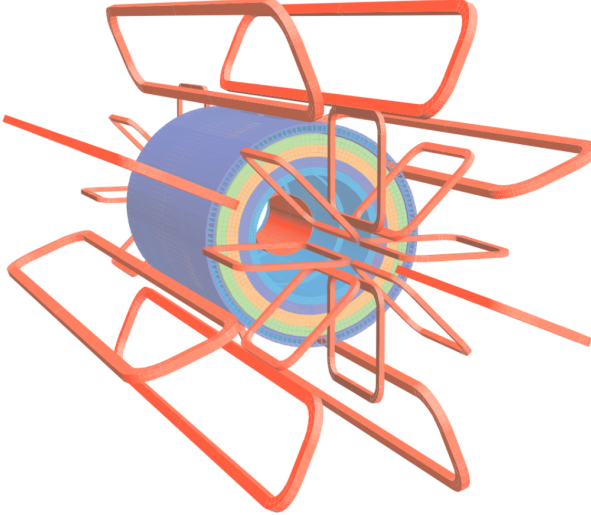


Figure 3.9: Geometry of magnet windings and tile calorimeter steel. Image taken from [2].

3.2.3 Inner detector

The inner detector (ID) is the closest sub-detector to the beam line, designed to track the early trajectories of charged particles for momentum calulations and locat their primary and secondary vertices with extremely high precision. The ID is required to deal with large numbers of tracks promptly, where 1000 particle collisions are taking place every 25 ns. The ID has full coverage in azimuthal angle ϕ and $|\eta| < 2.5$ acceptance in pseudorapidity. As mentioned briefly above, it consists of three parts: the pixel detector and the insertable B-Layer (IBL) [22] (as one part), the semiconductor tracker and the transition radiation tracker. The layout of the ID is shown in figure 3.10, with a charge track (in red) traversing the sensors and structural elements.

3.2.3.1 Pixel detector and IBL

The silicon pixel detector is the closest ATLAS component to the collision. It is composed of layers of silicon pixels and designed to have a very high granularity

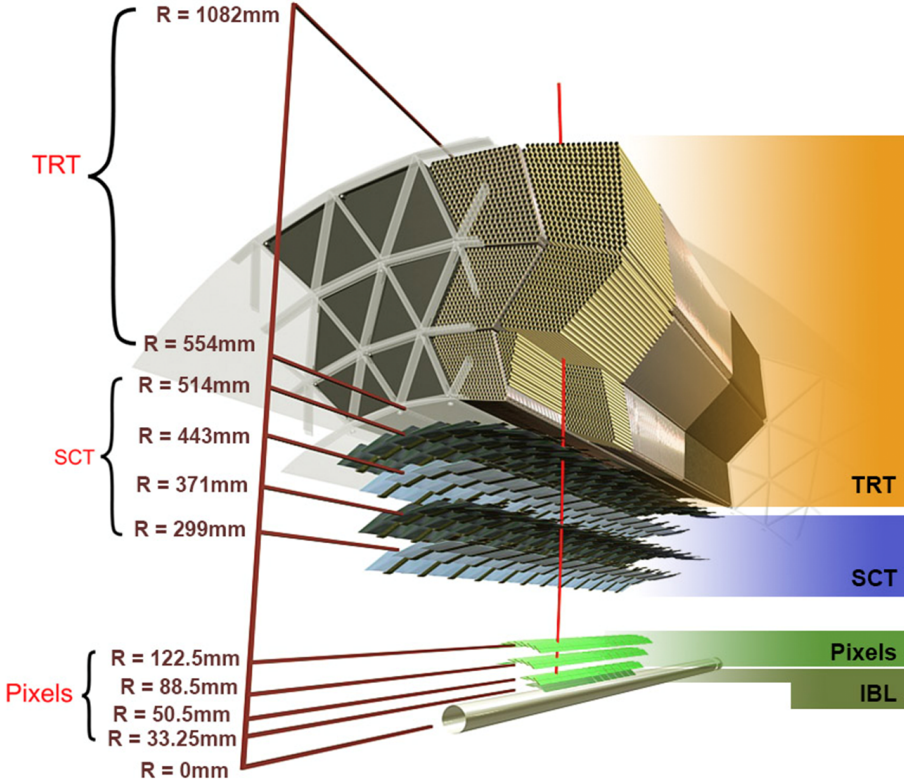


Figure 3.10: Cut-away view of the inner detector. Image taken from [23].

for reconstructing primary and secondary interaction vertices. The detector layers are formed of silicon sensor modules and in total there are approximately 92 million pixels (consequently, 92 million readout channels) in the system. It consists of three cylindrical layers in the barrel region, positioned at the radial distances of 50.5, 88.5 and 122.5 mm, and of disks perpendicular to the beams in the end-caps at the longitudinal distances of 49.5, 58.0 and 65.0 mm. In 2014, during the first LHC long shutdown, a fourth pixel layer was installed inside the existing detector, the insertable B-Layer (IBL) at a radius of 33 mm from the beam axis. The new pixel layer provides an additional space point very close to the interaction point, which significantly improves the identification of jets coming from b -quark hadronisation (b jets). Particles with $|\eta| < 2.5$ traverses the four layers usually produce four space-points. The pixel detector provides a resolution of $\sigma_\phi = 10 \mu\text{m}$ in the bending direction ($R - \phi$), and a resolution of $\sigma = 115 \mu\text{m}$ in the $z(R)$ direction in the barrel (end-cap) region.

3.2.3.2 Semiconductor tracker

The next constituent of the inner detector is the SCT. It is a silicon microstrip detector with over six million readout channels, which surrounds the pixel detector and covers the region of radius between 299 mm and 560 mm. It consists of four layers of strips located axially on the beam direction in the barrel region and placed along the z -direction in the end-cap region. This configuration allows the particles along the beam pipe to be constructed. Each layer of strips is glued back to back with an angle of 40 mrad to form a two-sided module and make possible the measurement of the second coordinate. The sensors are $285 \mu\text{m}$ thick and are constructed of high-resistivity n-type bulk silicon with p-type implants. Readout strips are positioned every $80 \mu\text{m}$, providing a spatial resolution of $\sigma_\phi = 17 \mu\text{m}$ in the bending direction ($R - \phi$) and $\sigma_\phi = 580 \mu\text{m}$ in the z (barrel) and R (end-cap) direction.

3.2.3.3 Transition radiation tracker

The outermost part of the inner detector is the TRT, which covers the radial region between 563 mm and 1066 mm. It is a straw drift tube tracker, which consists of modules of 4 mm diameter polyimide straws, filled with a mixture of gas of 70% Xe, 27% CO₂ and 3% O₂ and a gold-plated tungsten wire in the centre. The straws are interleaved with propylene fibres (foils) in the barrel (end-cap) region. With a spatial resolution of $\sigma_\phi = 130 \mu\text{m}$, the TRT measures the track position only in the bending direction ($R - \phi$). This is because when a charged particle passes through a straw tube, electrons from the gas are liberated through ionisation; under high voltage, these electrons then drift toward the wire in the centre, where a current flow is created and registered as a hit. Since a hit can happen on any location along the wire, the information of the z position of the particle is lost. In addition, the TRT provides capability of distinguishing electrons from other charged particles. When a highly-relativistic charged particle traverses the polymer straws interfacce, the particle emits transition radiation which is then absorbed by the Xeon gas. The intensity of the radiation depends on the gamma factor of the particle (strongest for lighter particles), hence this information can be exploited for electron identification.

3.2.4 Calorimeter system

Calorimeters are used to measure the energy of both charged and neutral particles. The ATLAS calorimeters [24], as shown in Figure 3.11, are consists of three major components, the Electromagnetic calorimeter, the Hadronic calorimeter and the Forward calorimeter (FCal). The fine granularity of the EM calorimeter is ideal for

precision measurements of electrons and photons; the coarser granularity of hadronic calorimeter is sufficient for the hadronic jet reconstruction; the FCal provides coverage of large pseudorapidity region: these calorimeters cover the range $|\eta| < 4.9$. All the three calorimeters are sampling calorimeters. Sampling calorimeters use different material the absorber and the active part: the absorber (or passive material) is responsible for producing particle showers where the active part then measures their energy. Note well the a fraction of total particles energy deposited in the passive material and it's not measured; the overall energy must be deduced from the definite measurements taken in the active detector layers.

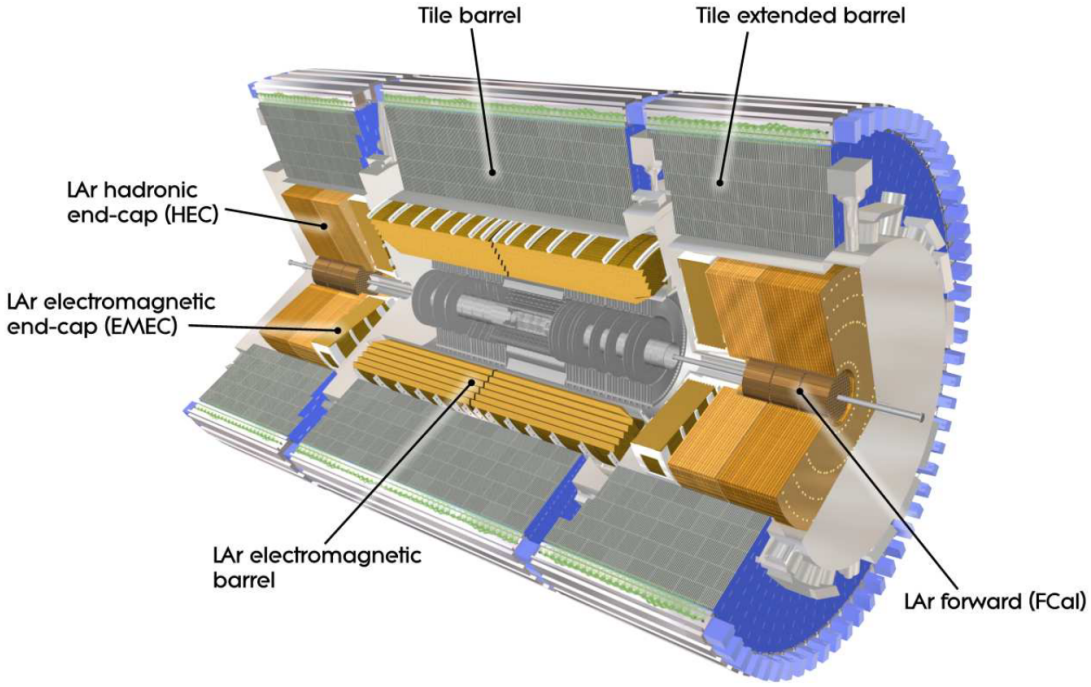


Figure 3.11: Cut-away view of the ATLAS calorimeter system. Image taken from [24].

The electromagnetic and hadronic showers must be contained in the calorimeter to ensure precise measurement of the total energy of the particle and to avoid punch-through into the muon system. The calorimeter depth is hence an important design consideration. The thickness of the calorimeter is measured in radiation length X_0 , which is the mean length of a material over which an electron will lose all but $1/e$ of its initial energy through radiative processes; and nuclear interaction length λ , which is the mean distance travelled by a hadronic particle before undergoing an inelastic nuclear interaction. The total thickness of the EM calorimeter is greater than 22 radiation lengths (X_0) in the barrel and greater than $24 X_0$ in the end-caps. The total thickness of the calorimeters, including 1.3λ from the outer support, is 11λ at $\eta = 0$ and has been shown both by measurements and simulations to be sufficient

to reduce punch-through well below the irreducible level of prompt or decay muons.

3.2.4.1 Electromagnetic calorimeter

The EM calorimeter is a lead-Liquid argon (lead-LAr) detector [18] with accordion-shaped (as shown in Figure 3.12) kapton electrodes and lead absorber plates over its full coverage, while using liquid argon (LAr) as the active material. The lead thickness in the absorber plates has been optimised as a function of η in terms of EM calorimeter performance in energy resolution. The EM calorimeter is divided into a barrel part ($|\eta| < 1.475$) and two end-cap components ($1.375 < |\eta| < 3.2$), each housed in their own cryostat. Additional material needed to instrument and cool the detector creates a “crack” region at $1.375 < |\eta| < 1.52$, where the energy resolution is significantly degraded.



Figure 3.12: A figure of the accordion-shaped electrodes.

The barrel calorimeter consists of two identical half-barrels, separated by a small gap (4 mm) at $z = 0$. Each end-cap calorimeter is mechanically divided into two coaxial wheels: an outer wheel covering the region $1.375 < |\eta| < 2.5$, and an inner wheel covering the region $2.5 < |\eta| < 3.2$.

The calorimeter has three layers along the transverse direction: a pre-sampler with very high granularity in η , in order to reconstruct the neutral pions decaying to two photons and particles which already starts showering in the inner detector. The pre-sampler is followed by longer towers of relatively high granularity, which is the major part of detecting EM showers, and responsible for measuring the η and ϕ coordinates of the particles. The last layer detects showers generated from particles other than electrons or photons that start showering inside the EM calorimeter before leaving it.

3.2.4.2 Hadronic calorimeter

The Hadronic calorimeter is comprised of the Tile Hadronic calorimeter (HCAL) and the LAr hadronic end-cap calorimeter (HEC). The HCAL is placed directly outside the EM calorimeter envelope. Its barrel covers the region $|\eta| < 1.0$, and its two extended barrels the range $0.8 < |\eta| < 1.7$. It is using steel as the absorber and scintillating tiles as the active material. It is segmented in depth in three layers, approximately 1.5, 4.1 and 1.8 λ thick for the barrel and 1.5, 2.6, and 3.3 λ for the extended barrel. The total detector thickness at the outer edge of the tile-instrumented region is 9.7λ at $\eta = 0$.

The HEC is similar to the construction to the ECAL, using LAr as the active material, but instead of using lead it uses copper as the absorber. It consists of two independent wheels per end-cap, located directly behind the end-cap electromagnetic calorimeter and sharing the same LAr cryostats. The HEC covers the range of $1.5 < |\eta| < 3.2$, slightly overlapping with the forward calorimeter which will be described in the following paragraph (around $|\eta|= 3.1$) and the tile calorimeter ($|\eta| < 1.7$). This overlap is to reduce the drop in material density at the transition between the different calorimeters.

3.2.4.3 Forward calorimeter

The Forward Calorimeter (FCal) covers $3.1 < |\eta| < 4.9$ and is approximately 10 interaction lengths deep. It consists of three modules in each end-cap: the first, made of copper, is optimised for electromagnetic measurements, while the other two, made of tungsten, measure predominantly the energy of hadronic interactions. All three modules use LAr as active material. Due to high particle fluxes and energies in the forward region, the calorimeter must contain relatively long showers in the small volume allowed by design constraints, and thus must be very dense.

3.2.5 Muon Spectrometer

The muon spectrometer is the outermost and largest sub-detector of ATLAS. A cut-away view of the MS is illustrated in Figure 3.13. It fully covers the calorimeter system and occupies a large part of the ATLAS cavern. It is based on the magnetic deflection of muon tracks in the large superconducting air-core toroid magnets, instrumented with separate trigger and high-precision tracking chambers. Over the range $|\eta| < 1.4$, magnetic bending is provided by the large barrel toroid. For $1.6 < |\eta| < 2.7$, muon tracks are bent by two smaller end-cap magnets inserted into both ends of the barrel toroid. Over $1.4 < |\eta| < 1.6$, usually referred to as the

transition region, magnetic deflection is provided by a combination of barrel and end-cap fields. The configuration of magnets provides a field mostly orthogonal to the muon trajectories, hence minimising the degradation of resolution due to multiple scattering.

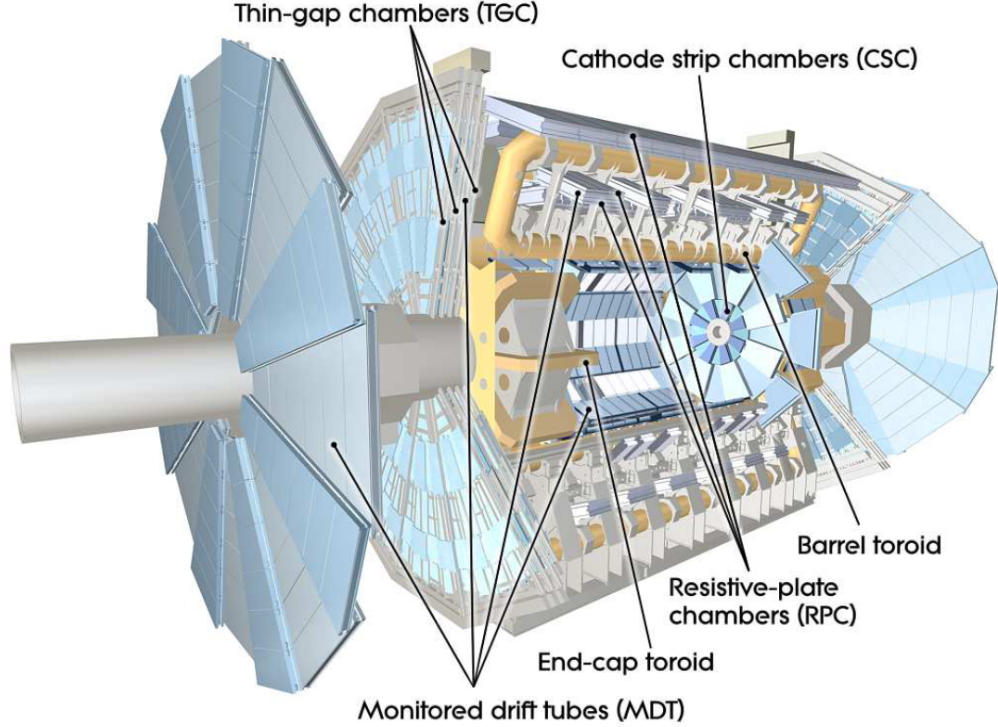


Figure 3.13: Cut-away view of the ATLAS muon spectrometer system. Image taken from [2].

The MS consists of four subsystems which rely on four different gas detector technologies. Two of them, the resistive plate chambers (RPC) in the barrel region and the thin gap chambers (TGC) in the end-cap region, provide trigger signals, while the other two, the monitored drift tubes (MDT) in the barrel and the cathode strip chambers (CSC) in the end-cap region provide the momentum measurement. The MDT chambers provide high precision measurements in the bending direction over most of the detector acceptance while the CSC are used in the forward region where the particle flux is too high for the MDT chambers. The muon chambers are arranged in the barrel ($|\eta| < 1.05$) in three cylindrical layers around the beam axis, while in the end-cap regions ($1.05 < |\eta| < 2.7$) they are placed in three wheels. The resolution of muons tracks momentum measurement varies from typically 2–3% over most of the kinematic range, to about 10% at $p_T = 1$ TeV.

3.2.6 Trigger system

As mentioned in section 3.1.3, the spacing of each bunch is 25 ns, which translates to a 40 MHz of bunch-crossing frequency, with up to 80 collisions per bunch crossing. This is far beyond the data collection bandwidth and storage capacity of ATLAS. Therefore, it's necessary to adopt a trigger system that make fast decisions whether an event is high quality, rare or “interesting” and to save the event or not. The ATLAS trigger system consists of two consecutive parts: the Level 1 trigger [25] which is hardware-based, followed by the software-based High Level Trigger (HLT) [26].

The L1 trigger searches for signatures from high- p_T muons, electrons/photons, jets, and τ -leptons decaying into hadrons. It also selects events with large MET and large total transverse energy. The L1 trigger uses reduced-granularity information from a subset of detectors: the RPC and TGC for high- p_T muons, and all the calorimeter sub-systems for electromagnetic clusters, jets, τ -leptons, E_{miss}^T , and large total transverse energy. As a result, the L1 trigger reduces the event rate from 40 MHz to a maximum of 100 kHz. The decision is made by Central Trigger Processor (CTP), which operates on signals from dedicated hardware in the calorimeter and muon detector systems. The decision time, at under 2.5 μs , is faster than the ID can process events so ID information is omitted. For each data-taking period, the L1 trigger is loaded with a trigger menu, a list of up to 256 criteria used to determine whether an event is accepted. The trigger menus are designed to accommodate a broad physics programme, with high acceptance for both BSM searches and SM precision measurements. The L1 trigger also uses detector information with reduced granularity to identify Regions of Interest (RoI) [27] in ϕ and η . The ROI information with full granularity and precision and all the available detector data (including the ID information) within the ROI's are provided to the HLT. This trigger level reduces the rate of events by two orders of magnitude, reaching an average of 1 kHz with a latency of 0.2 μs . These events are passed on to a data storage system for offline analysis.

Chapter 4

Data and Monte Carlo samples

Chapter 5

Object Reconstruction

Particles produced in the pp collisions inside ATLAS can interact with the detector subsystems with each type of particle leaving a unique signature. Reconstructing and identifying these particles precisely and efficiently using the information recorded in each sub-detectors is a building stone of physics analysis. Therefore, the following chapter outlines the reconstruction procedure of the particles important for the analysis present in this thesis, referred to as ‘physics objects reconstruction’.

5.1 Track and vertex reconstruction

Track and vertex reconstruction is a starting point of physics objects reconstruction, which makes it crucial to understand how they are implemented in ATLAS. Track reconstruction [28, 29] is done mainly with the “inside-outside” procedure, complemented by the “outside-in” and the reconstructing of TRT-standalone tracks. The inside-out stage starts from assembling the raw measurements into *clusters*: an algorithm called connected component analysis [30] groups pixels and strips in a given sensor, where the deposited energy yields a charge above threshold, with a common edge or corner into clusters.

From clusters, three-dimensional measurements referred to as *space points* are created (the yellow points in Figure 5.1). They represent the point where the charged particle traversed the active material of the ID. Each space point equates to one cluster in the pixel detector, while in the SCT, clusters from both sides of a strip layer must be combined to obtain a three-dimensional measurement. Three sets of space points are combined to track seeds (circled in blue in Figure 5.1). A combinatorial Kalman filter [31] is used to build track candidates from the chosen seeds by incorporating additional space points from the remaining layers of the pixel and SCT detectors which are compatible with the preliminary trajectory (circled in blue

dashed line in Figure 5.1). A track score computed by the quantities of the fitted

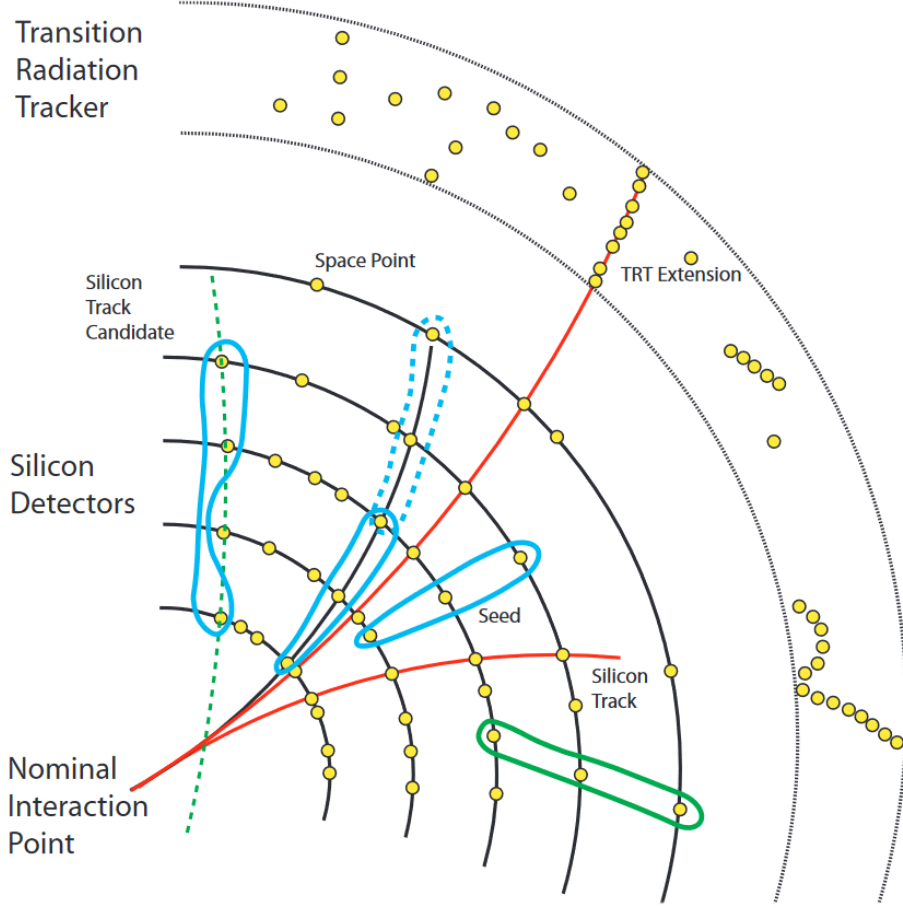


Figure 5.1: An example of track reconstruction. Image reproduced from [32].

track is assigned to each track. The tracks candidates are processed in descending order of track score, those fail a set of minimum requirement on p_T , number of holes, number of clusters etc are rejected; candidates that have too many bad quality clusters are stripped down and re-scored and returned to the list of remaining candidates. This process is referred to as “ambiguity solving” [29]. Finally, the tracks are extended into the TRT, and by using the full information of the three sub-detectors, the tracks are fitted again to estimate the final track impact parameter (IP, transverse distance from the interaction point) d_0 , distance from the interaction point along the z axis z_0 , azimuthal angle ϕ , polar angle θ and charge momentum ratio q/p_T .

The complementary “outside-in” algorithm starts with searching for tracks with segments reconstructed in the TRT, and extend the tracks inwards by adding silicon hits. The tracks are built with the combinatorial Kalman filter and passed to the ambiguity solving procedure. Finally, tracks with a TRT segment but no extension

into the silicon detectors are referred as TRT-standalone tracks.

After the tracks are reconstructed, primary vertices, which are the points where the hard scattering occurred, are reconstructed in two steps [33]: a) the primary vertex finding algorithm, dedicated to associate reconstructed tracks to the vertex candidates, and b) the vertex fitting algorithm, dedicated to reconstruct the vertex position. Vertex seeds are obtained from the z -position at the beamline of the reconstructed tracks. An iterative χ^2 fit is made using the seed and nearby tracks. Each track carries a weight which is a measure of its compatibility with the fitted vertex depending on the χ^2 of the fit. Vertices are required to contain at least two tracks, and tracks displaced by more than 7σ from the vertex are used to seed a new vertex and the procedure is repeated until no additional vertices can be found. This procedure is repeated until no unassociated tracks are left in the event or no additional vertex can be found. The primary vertex for each event is selected as the vertex with the highest $\sum_{tracks} (p_T^{track})^2$.

5.2 Electron

When an high energy electron (or positron) enters the detector, it interacts with the detector material primarily via bremsstrahlung. This results in radiation of photons, which subsequently convert into electron–positron pairs which continue to interact with the detector material, leading to a cascade of particles of decreasing energy. These cascade particles are usually referred to as electromagnetic *shower*. They are very collimated and frequently create neighbouring signals in the calorimeter component. These interactions can occur inside the inner-detector volume or even in the beam pipe, generating multiple tracks in the inner detector, or can instead occur downstream of the inner detector, only impacting the shower in the calorimeter.

5.2.1 Reconstruction

The reconstruction of electron is based on three fundamental components: a) localised clusters of energy deposits found within the EM calorimeter, b) charged tracks identified in the ID (as described in details in chapter 5.1), and c) close matching in $\eta \times \phi$ space of the tracks to the clusters [34]. Figure 5.2 provides a schematic illustration of the elements that enter into the reconstruction and identification of an electron. The reconstruction starts from EM cluster seeding from localised energy deposits using a sliding-window algorithm [35]. The $\eta \times \phi$ space of the EM is divided into *towers* of 200×256 elements of size $\Delta\eta \times \Delta\phi = 0.025 \times 0.025$, consistent with the granularity of the second layer of the EM calorimeter. Then algorithm

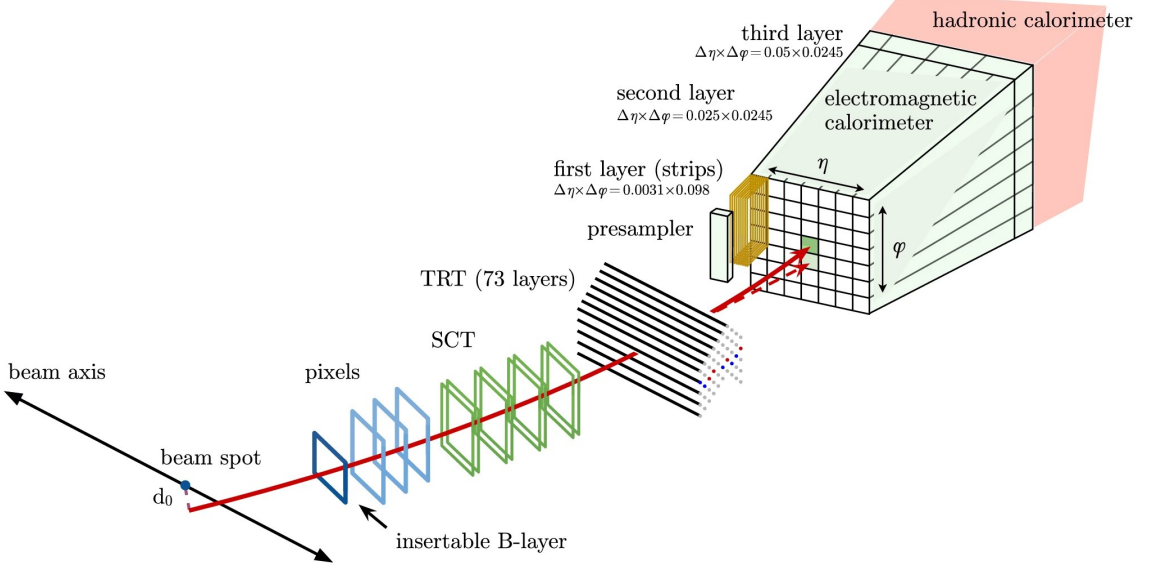


Figure 5.2: A schematic illustration of the path of an electron through the detector. The red trajectory shows the hypothetical path of an electron, which first traverses the tracking system (pixel detectors, then SCT and lastly the TRT) and then enters the electromagnetic calorimeter. The dashed red trajectory indicates the path of a photon produced by the interaction of the electron with the material in the tracking system. Image taken from [34].

then ‘‘slides’’ a rectangular window of size 3×5 towers whose summed transverse energy exceeds 2.5 GeV to form a seed-cluster. The centre of the seed moves in steps of 0.025 in either η or ϕ direction to search for localised energy deposits; this process is repeated until every element of the calorimeter has been covered. To better account for the energy loss of charged particles in material, a subsequent fitting procedure using optimised Gaussian-sum filter [36] is performed on tracks which are ‘‘loosely’’ matched to the EM clusters, which requires the tracks and clusters to satisfy: $|\eta_{cluster} - \eta_{track}| < 0.05$ and one of the two requirements: $-0.20 < \Delta\phi < 0.05$ or $-0.10 < \Delta\phi_{res} < 0.05$, where $\Delta\phi \equiv -q \times (\phi_{cluster} - \phi_{track})$ with q being the charge of the particle, and $\phi_{cluster}$, ϕ_{track} and $\eta_{cluster}$, η_{track} are the ϕ , η coordinates of the cluster barycentre and the position of the track extrapolated from the perigee to the second layer of the calorimeter, respectively; $\Delta\phi_{res}$ is similar to $\Delta\phi$ but with the momentum of the track rescaled to the energy of the cluster. The assymmetry in the condition is to account for the energy loss due to bremsstrahlung where tracks with negative (positive) electric charge bend due to the magnetic field in the positive (negative) ϕ direction.

The matching of the fitted tracks to the candidate calorimeter seed-cluster is the final step of electron reconstruction. The matching requires $-0.10 < \Delta\phi < 0.05$, with the other alternative requirement remaining the same. If several tracks fulfil the

matching criteria, the track considered to be the primary electron track is selected using an algorithm that takes into account the distance in η and ϕ between the extrapolated tracks and the cluster barycentres (again, measured in the second layer of the calorimeter), the number of hits in the silicon detectors and in the innermost silicon layer; a candidate with an associated track with at least four hits in the silicon layers and no association with a vertex from a photon conversion (photon converting into electron-positron pair) is considered as an electron candidate. However, if the primary candidate track can be matched to a secondary vertex and has no pixel hits, then this object is classified as a photon candidate (likely a conversion).

A further classification is performed using the candidate electron's E/p and p_T , the presence of a pixel hit, and the secondary-vertex information, to determine unambiguously whether the object is only to be considered as an electron candidate or if it should be ambiguously classified as potentially either a photon candidate or an electron candidate.

5.2.2 Identification

The reconstruction algorithm is very efficient in reconstructing electron, however, this is not necessarily what is needed for many ATLAS analysis, where they are interested in prompt electrons. Prompt electrons are electrons coming from the collision of the an event, while non-prompt electrons may come from the semileptonic decays of heavy quarks or from photon conversion. Other objects such as hadrons can be mis-reconstructed as electron as well. It necessitates the identification of prompt electrons, making use of the differences between prompt electrons and non-prompt electrons/mis-reconstructed electrons. A multivariate likelihood technique, taking advantages of the correlations among the variables describing the differences, is employed to select prompt electrons [34]. The input to the likelihood includes the differences of: a) shower shape, b) properties of the track, c) matching of the track and clusters. In addition, many analysis further require the electron to pass some *isolation* requirements. Isolation is built exploiting a characteristic signature of the prompt electrons that there is relatively little activity surrounding the prompt electrons, as compared to non-prompt electrons [37].

To quantify the performance of the identification, the identification efficiency is measured, which represents the probability of a prompt electron being reconstructed as an electron. Different cuts are applied on the final discriminant to define *working points* (WP), which can specify the identification efficiency, as a function of E_T or η of the electron. Three WPs, *Loose*, *Medium* and *Tight* are defined, each WP places a different requirement on final discriminant made with a different set of

variables. An example of the electron identification efficiency is shown in Figure 5.3. Similary for electron isolation, four WPs: *Gradient*, *HighPtCaloOnly*, *Loose* and

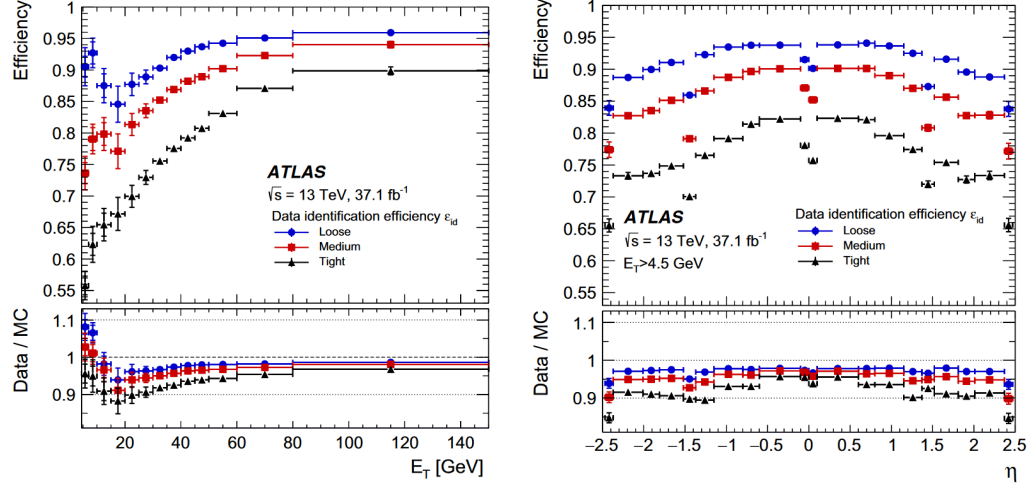


Figure 5.3: Measured electron identification efficiencies in $Z \rightarrow ee$ events for the ‘Loose’ (blue circle), ‘Medium’ (red square), and ‘Tight’ (black triangle) WPs as a function of E_T (left) and η (right). The vertical uncertainty bars (barely visible because they are small) represent the statistical (inner bars) and total (outer bars) uncertainties. For both plots, the bottom panel shows the data-to-simulation ratios. Reproduced from Reference [34].

Tight are defined, each targeting a fixed value of isolation efficiency or imposing fixed requirement on the isolation variables.

In the analysis presented in Chapter 7 the ‘Loose’ identification WP is used, with additional requirements on the electron $p_T > 7 \text{ GeV}$ and $|\eta| < 2.47$; the electron candidates are also required to pass the ‘Loose’ isolation WP which has an efficiency of 99%. The isolation requirement is also inverted to provide control regions for estimating backgrounds. In the calibration effort presented in Chapter 6 the ‘Medium’ identification WP is used, with additional requirements on the electron $p_T > 27 \text{ GeV}$ and $|\eta| < 2.47$; electrons are required to pass the ‘Gradient’ isolation WP, designed to give an efficiency of 90% at $p_T = 25 \text{ GeV}$ and 99% at $p_T = 60 \text{ GeV}$. The different requirements in the two chapters is the result of different signal targeted and hence different purity and phase space is needed.

5.3 Muon

5.3.1 Reconstruction

The characteristic behaviour of a muon in the detector is a particle ionising minimally. The muon reconstruction is done taking advantage of this feature, with information from the ID and MS tracking detectors, while information from the

calorimeters is also used for determination of track parameters and to account for cases of large energy loss in the calorimeters, and for MS-independent tagging of ID tracks as muon candidates [38]. The muon reconstruction consists of two steps. The first step is to reconstruct the stand-alone track in the MS, followed by reconstruction with complete detector information.

The first step of reconstruction starts with the identification of short straight-line local track segments reconstructed from hits in an individual MS *stations* (layers). These segments are then combined into preliminary track candidates, with information from precision measurements in the bending plane and measurements of the second coordinate from the MS triggers to create three-dimensional track candidates. A global χ^2 fit of the muon trajectory through the magnetic field is performed, outlier hits are removed and hits along the trajectory that were not assigned to the original track candidate are added. Finally, the tracks are fitted again with the updated hits information, and ambiguities are resolved by removing tracks that share a large fraction of hits with higher-quality tracks.

The second step of reconstruction is to combine the track candidates with the complete information of all sub-detectors. The reconstruction proceeds according to five main reconstruction strategies, leading to the corresponding muon types:

- *combined muons* are identified by matching MS tracks to ID tracks and performing a combined track fit based on the ID and MS hits, taking into account the energy loss in the calorimeters.
- *Inside out muons* are reconstructed using a complementary inside-out algorithm, which extrapolates ID tracks to the MS and searches for at least three loosely-aligned MS hits. The ID track, the energy loss in the calorimeters and the MS hits are then used in a combined track fit.
- *Muon-spectrometer extrapolated muons* are muons when an MS track cannot be matched to an ID track. Its parameters are extrapolated to the beamline and used to define an Muon-spectrometer extrapolated muon. Such muons are used to extend the acceptance outside that of the ID, thus fully exploiting the full MS coverage up to $|\eta| = 2.7$.
- *segment-tagged muons* are identified by requiring that an ID track extrapolated to the MS satisfies tight angular matching requirements to at least one reconstructed MS segment.
- *calorimeter-tagged muons* are identified by extrapolating ID tracks through the calorimeters to search for energy deposits consistent with a minimum-ionising

particle.

5.3.2 Identification

Muon identification is performed by applying quality requirements that suppress background, mainly from pion and kaon decays, while selecting prompt muons with high efficiency. Muon candidates originating from in-flight decays of charged hadrons in the ID are often characterized by the presence of a distinctive ‘kink’ topology in the reconstructed track. As a consequence, it is expected that the fit quality of the resulting combined track will be poor and that the momentum measured in the ID and MS may not be compatible [39]. Therefore, a set of requirements on the number of hits in the different ID subdetectors and different MS stations, on the track fit properties, and on variables that test the compatibility of the individual measurements in the two detector systems [38]. A set of WPs are defined for each of the muon types defined in the previous section. The main metrics considered for designing the WPs are the selection efficiency and purity in simulation, where the prompt muon efficiency of a selection WP represents the probability that a prompt muon traversing the detector is reconstructed as a muon and satisfies the WP; the purity of a selection WP is one minus the hadron misidentification rate (the fraction of light hadrons reconstructed as muons and satisfying the WP). Three standard selection WPs: *Loose*, *Medium*, and *Tight* are designed to cover the majority of physics analysis, with two additional WPs, *High- p_T* and *Low- p_T* are designed to accommodate the analysis targeting extreme phase space. In Chapter 7, muons are selected with $p_T > 7 \text{ GeV}$ and $|\eta| < 2.7$, and passing the ‘loose’ identification criteria as well as the ‘pflowLoose_VarRadIso’ isolation criteria [40]; while in Chapter 6 muons are selected with $p_T > 27 \text{ GeV}$ and $|\eta| < 2.5$, and passing the ‘medium’ identification criteria as well as a track-based isolation criteria. An example of the reconstruction and isolation efficiency of muon is shown in Figure 5.4.

5.4 Jet

5.4.1 Reconstruction

A jet can be defined as a collimated spray of stable particles arising from the fragmentation and hadronisation of a parton (quark or gluon) after a collision. Jets provide a link between the observed colourless stable particles and the underlying physics at the partonic level. A basic illustration of a collision of two protons, the subsequent particle shower and a reconstructed jet is shown in Figure 5.5.

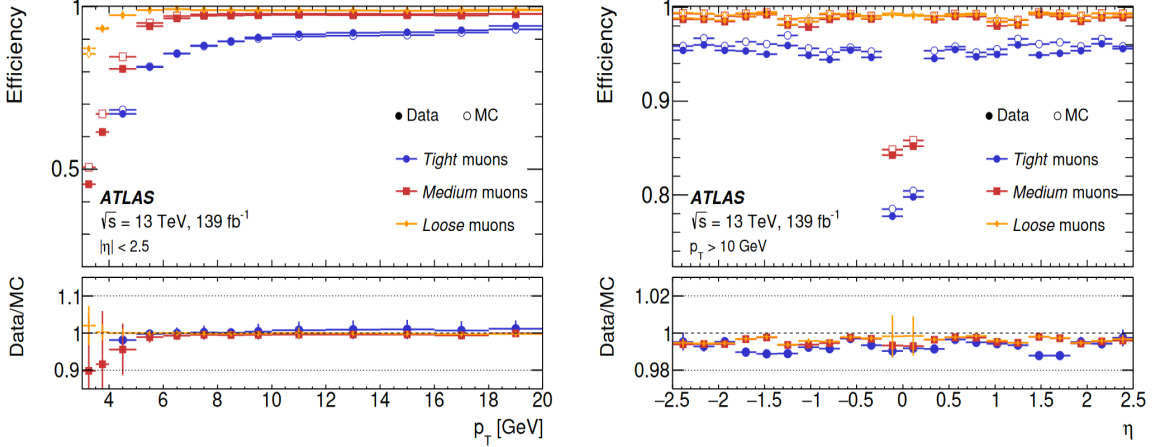


Figure 5.4: Muon reconstruction and identification efficiencies for the Loose, Medium, and Tight criteria. The left plot shows the efficiencies measured in $J/\psi \rightarrow \mu\mu$ events as function of p_T . The right plot displays the efficiencies measured in $Z \rightarrow \mu\mu$ events as a function of η , for muons with $p_T > 10$ GeV. The predicted efficiencies are depicted as open markers, while filled markers illustrate the result of the measurement in collision data. The statistical uncertainty in the efficiency measurement is smaller than the size of the markers, and thus not displayed. The panel at the bottom shows the ratio of the measured to predicted efficiencies, with statistical and systematic uncertainties. ratios. Reproduced from Reference [38].

The jet reconstruction starts by forming clusters of energy deposit in the calorimeters performing a three-dimensional topological clustering of individual calorimeter cell signals [42]. The algorithm clusters the energy deposits into so called “topo-clusters” and combines their four-momenta. In Run 1 of the LHC, the ATLAS experiment used either solely the calorimeter or solely the tracker to reconstruct hadronic jets and soft particle activity, and the vast majority of analysis utilised jets that were built from topo-clusters, referred to *EMTopo jets*. An alternative approach called “*Particle flow*” (PFlow) was done in ATLAS, as described in details in reference [43]. It is the default approach for the thesis. Measurements from both the tracker and the calorimeter are combined to form the signals. More specifically, the algorithm matches the reconstructed tracks to the candidate leptons and hadrons, in order to produce a new set of clusters called *PFlow clusters* from topo-clusters. Using the PFlow clusters as inputs, PFlow jets are then reconstructed using the anti- k_t algorithm [44]. The anti- k_t algorithm sequentially combines PFlow clusters into larger clusters based on the momentum-weighted distance between clusters. For two clusters i and j the algorithm defines:

$$d_{i,j} = \min(p_{T,i}^{2p}, p_{T,j}^{2p}) \frac{\Delta R_{i,j}^2}{R^2}$$

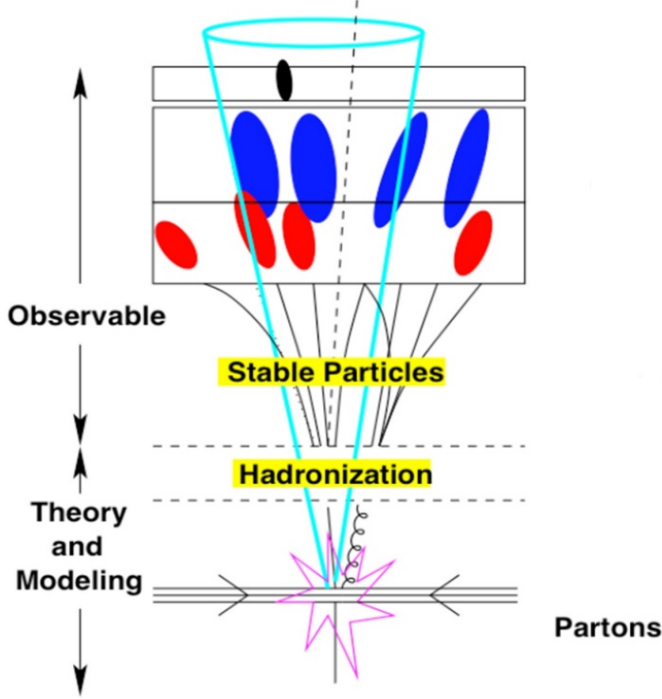


Figure 5.5: A simple example of an event showing the point of collision, the fragmentation and hadronization of the quarks and gluons and the resulting jet found through the detection of the stable particles. Image reproduced from [41].

and

$$d_{i,beam} = p_{T,i}^{2p}$$

where p is a exponent parameter and the value of -1 is used for the anti- k_t algorithm (as the name ‘anti’ suggests), $\Delta R^2 i,j = (\eta_i - \eta_j)^2 + (\phi_i - \phi_j)^2$, and $p_{T,i}$, η_i and ϕ_i are the transverse momentum, pseudorapidity and azimuthal coordinate of cluster i , respectively. The parameter R controls the size of the jet and for standard jets in ATLAS this is chosen to be $R = 0.4$. The algorithm combines objects i, j with minimum value of $d_{i,j}$ into one object iterartively, until no more $d_{i,j}$ can be found greater than $d_{i,beam}$, where the combined object is considered the final jet candidate.

A validation study is done by the author for comparison of the EMTopo jets to PFlow jets used in the analysis TODO: add reference after selection is defined.

5.4.2 Calibration

After the jets are reconstructed, the four-momenta of jets are calibrated with the jet energy scale (JES) calibration consists of several consecutive stages derived from a combination of MC-based methods and in situ techniques [45]. MC-based calibrations correct the reconstructed jet four momentum to that found from the simulated

stable particles within the jet. The calibrations account for features of the detector, the jet reconstruction algorithm, jet fragmentation, and the busy data-taking environment resulting from multiple pp interactions, and the difference in jet response between data and MC simulation. In order to calibrate jet energy resolution (JER), jet momentum must be measured precisely. As described in details in reference [46], a *dijet balance* approach is used for this purpose with well-defined dijet system, where the two jets are expected to have p_T that sum up to 0 precisely. Furthermore, jets arised from pileup are suppressed by using the *jet vertex tagger*, which is a multivariate combination of track-based variables developed to separate hard-scatter jets from pileup jets [47]. A jet cleaning selection is applied in order to veto any ‘fake’ jets, which arise from non-collision background events, such as cosmic rays, or from detector effects. Finally, all jets in the analysis are required to have $p_T < 20$ GeV and $|\eta| < 2.5$.

5.4.3 Identification of heavy quark flavoured jets

As frequently being called *flavour tagging*, the identification of jets containing b -hadrons (b jets) against the large background of jets containing c -hadrons (c jets) or jets coming from the hadronization of light (u,d,s) quarks or gluons (light jets) is of major importance in many areas of the physics programme of the ATLAS experiment at the LHC. It is crucial in a large number of SM precision measurements, studies of the Higgs boson properties, searches for new phenomena [48–50], and it also plays an important role in the $HH \rightarrow bb\tau\tau$ searches presenting in Chapter 7.

The ATLAS Collaboration uses various algorithms to identify b jets [51], referred to as b -tagging algorithms, when analysing data recorded during Run 2 of the LHC. These algorithms exploit the long lifetime, high mass and high decay multiplicity of b -hadrons, as well as the properties of the b quark fragmentation. Given a lifetime of the order of 1.5 ps, b -hadrons have a significant mean flight length ($\langle c\tau \rangle \approx 450 \mu m$), in the detector before decaying, generally leading to at least one vertex displaced from the hard-scatter collision point, as illustrated in Figure 5.6.

The strategy developed by the ATLAS Collaboration is based on a two-stage approach. Firstly, low-level algorithms reconstruct the characteristic features of the b jets via two complementary approaches, a) that uses the individual properties of charged-particle tracks associated with a hadronic jet, and b) that combines the tracks to explicitly reconstruct displaced vertices. These algorithms, first introduced during Run 1 [51], have been improved and retuned for Run 2 [52]. Secondly, in order to maximise the b -tagging performance, the results of the low-level b -tagging algorithms are combined into high-level algorithms via multivariate classifiers.

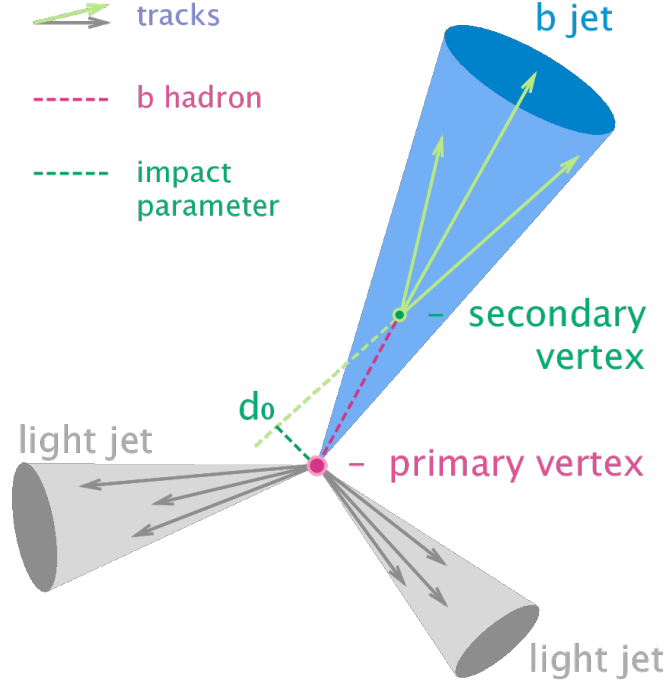


Figure 5.6: A diagram showing the b hadron decay initiated jets.

The most performant algorithms presently in use in physics analyses at ATLAS are based on multivariate combinations of the available information (MV2) or additionally using a deep feed-forward neural network (DL1) [53, 54], as shown in Figure 5.7, where the performance is characterised by the probability of tagging a b jet (b jet tagging efficiency, ϵ_b) and the probability of mistakenly identifying a c jet or a light-flavour jet as a b jet labelled $\epsilon_c(\epsilon_l)$. In addition, the distribution of the output discriminant of the MV2 and DL1 tagger for b jet, c jet, and light-flavour jets in the $t\bar{t}$ simulated events are shown in Figure 5.8. Depending on the low-level algorithm, the DL1 tagger can be further separated into two taggers: DL1 and DL1r, where the DL1 tagger uses traditional track-based impact parameter taggers IP2D and IP3D [55] and the DL1r tagger uses a Recurrent Neural Network Impact Parameter tagger (RNNIP) [54]. The calibration of DL1 and DL1r algorithms has been an original contribution of the author of this thesis and it is described in more detail in Chapter 6. The DL1r tagger is now the default b -tagging algorithm used for flavour tagging in ATLAS.

5.5 Hadronically decaying τ lepton

With a mass of 1.777 GeV and a proper decay length of $87 \mu\text{m}$ [56], tau leptons decay either leptonically ($\tau_{\text{lept}} \rightarrow \ell\nu\ell\nu\tau$, $\ell = e, \mu$) or hadronically ($\tau_{\text{had}} \rightarrow \text{hadrons}$

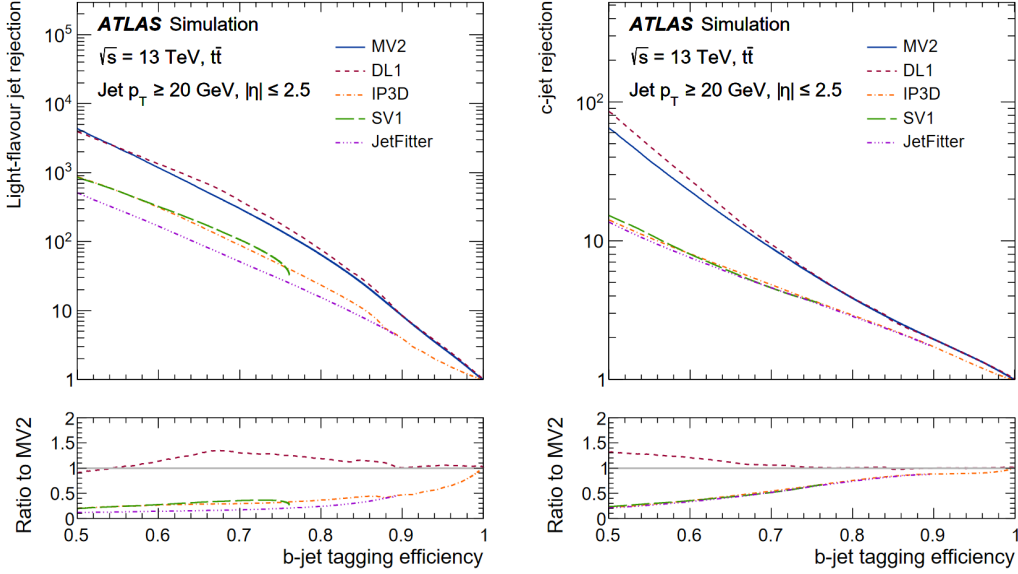


Figure 5.7: The light-flavour jet (left) and c jet (right) rejections versus the b jet tagging efficiency for the IP3D, SV1, JetFitter, MV2 and DL1 b -tagging algorithms evaluated on the $t\bar{t}$ events [52].

ν_τ) and do so typically before reaching active regions of the ATLAS detector. The leptonically decaying τ_{lep} is simply reconstructed as either an electron or muon, with the neutrinos contributing to the real component of the E_T^{miss} . On the other hand, the hadronically decaying τ_{tau} can be identified via their decay products. The hadronic tau lepton decays represent 65% of all possible decay modes [56]. In these decay modes, the hadronic decay products are one or three charged pions in 72% and 22% of all cases, respectively. Charged kaons are present in the majority of the remaining hadronic decays. In 78% of all hadronic decays, up to one associated neutral pion is also produced. The neutral and charged hadrons stemming from the tau lepton decay make up the visible decay products of the tau lepton, and are in the following referred to as $\tau_{had-vis}$.

5.5.1 Reconstruction

The $\tau_{had-vis}$ candidates are seeded by jets formed using the anti- k_t algorithm, with a jet-size parameter R of 0.4. For events with multiple interactions, the chosen primary may not be the vertex where the tau lepton is originated. There the *tau vertex association* algorithm is used with input as all tau candidates tracks within a region of $\Delta R < 0.2$ around the jet seed direction. The p_T of these tracks is summed and the primary vertex candidate to which the largest fraction of the p_T sum is matched to is chosen as the tau vertex [47].

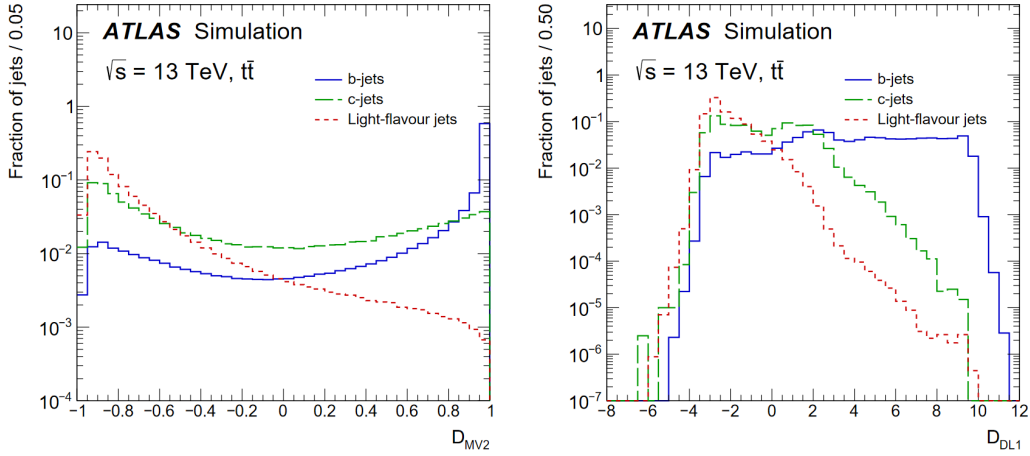


Figure 5.8: The fraction of light-flavour jets and c jets versus the b jets in the MV2 (left) and DL1 (right) b-tagging algorithms output distribution evaluated on the $t\bar{t}$ events [52].

Tracks are associated with the $\tau_{had-vis}$ if they are in the *core* region $\Delta R < 0.2$ around the $\tau_{had-vis}$ direction and satisfy the following criteria: $p_T > 1$ GeV, at least two associated hits in the pixel layers of the inner detector, and at least seven hits in total in the pixel and the SCT layers. Furthermore, requirements are imposed on the distance of closest approach of the track to the track vertex in the transverse plane, $|d_0| < 1.0$ mm, and longitudinally, $|z_0 \sin \theta| < 1.5$ mm. Tracks in the *isolation* region $0.2 < \Delta R < 0.4$ are used for the calculation of identification variables and are required to satisfy the same selection criteria. The number of core tracks defines the number of *prongs*.

5.5.2 Identification

The $\tau_{had-vis}$ reconstruction algorithm alone provides no discrimination against other particles that result in jet-like signatures in the detector. Therefore, dedicated algorithms are used to identify hadronic tau lepton decays. Here, a recurrent neural network (RNN) classifier is used as described in reference [57]. Compared to the ID that was used in the analysis of the 36.1 fb^{-1} data [58], which was based on a boosted decision tree, the RNN tau-ID shows better performance and allows to move to a looser WP gaining increased efficiency (about 24% and 11% in case of two τ_{had} and one τ_{had} in the final state, respectively) without losing jet rejection, as shown in Figure 5.9. Due to the distinct signatures of 1- and 3-prong τ_{had} decays, the τ_{had} -identification (τ_{had} -ID) is split into dedicated algorithms for 1- and 3-track $\tau_{had-vis}$. Selected $\tau_{had-vis}$ candidates in the analysis are required to have $p_T > 20$ GeV, $|\eta| < 2.5$, with candidates in the barrel-endcap transition region of the calorimeter ($1.37 < |\eta| < 1.52$) vetoed due to poor detector instrumentation in this region, one or

three tracks, unit charge, and to pass the ‘loose’ τ_{had} -ID working point. The loose WP corresponds to 85% efficiency for 1-prong and 75% efficiency for 3-prong (the efficiency is flat in p_T by definition).

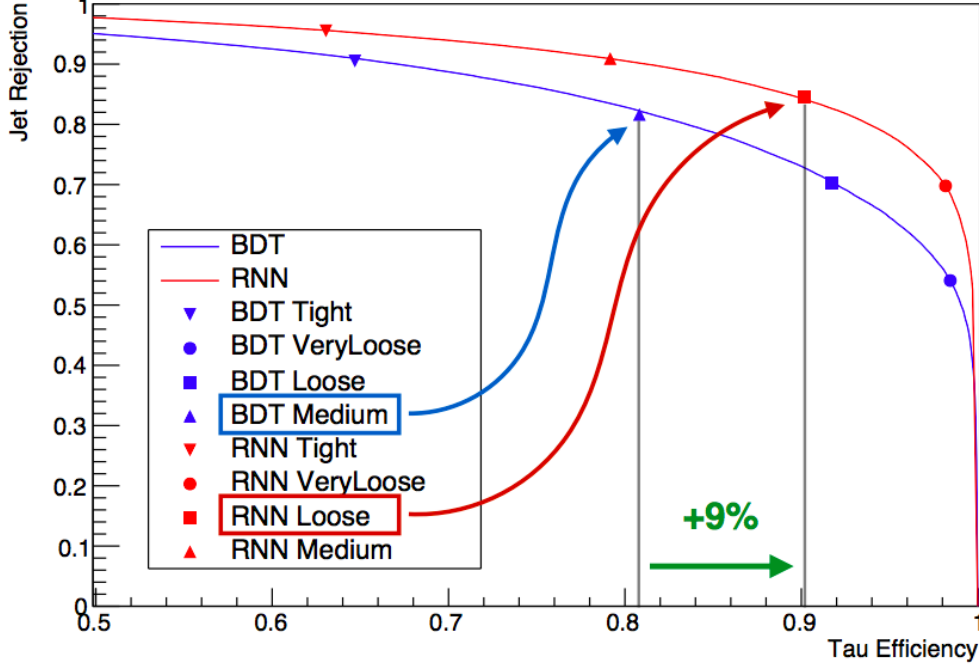


Figure 5.9: Jet rejection and tau efficiency of tau candidate, measured in $\gamma^* \rightarrow \tau\tau$ sample for RNN-ID [57] and $Z/\gamma^* \rightarrow \tau\tau$ sample for BDT-ID [59]. Jet rejection represents the probability of a jet not originating from a tau lepton being rejected by the identification algorithm. The green arrow indicates the increase in tau efficiency.

Additional rejection of $\tau_{had-vis}$ candidates originating from electrons is provided by a BDT employing track and shower shape information, the ‘loose’ working point is used, corresponding to a selection efficiency of about 95% efficiency for true $\tau_{had-vis}$ [60].

5.5.3 Anti- τ_{had} definition

In order to provide fake- τ_{had} -enriched regions used for background estimation, an “anti- τ_{had} ” selection is defined. Those $\tau_{had-vis}$ objects that fail the RNN loose τ_{had} -ID and have the RNN score greater than 0.01 are labelled as anti- τ_{had} candidates. For channels where τ_{had} -ID is applied at trigger level, anti- τ_{had} candidates are also required to be matched to the trigger τ_{had} in the same way as is required for signal taus. This definition selects objects that are predominantly jets faking hadronic τ decays. The minimum RNN score requirement ensures that the jets still have some τ_{had} -like properties and ensures that the composition of quark- and gluon-initiated

jets is closer to that of the signal region. More details of the choice of the minimum τ_{had} -ID RNN-score threshold are reported in TODO: link to the fake factor section

5.5.3.1 Anti- τ_{had} selection: TODO: should I put this section in here or in analysis chapter?

Anti- τ_{had} objects are selected only in events in which there are fewer τ_{had} that pass the offline τ_{had} -ID than required for a given channel (one for the $\tau_{lep}\tau_{had}$ and two for the $\tau_{had}\tau_{had}$ selection). In that case, additional anti- τ_{had} candidates are selected so that the total number of selected τ_{had} (loose, which always has priority, and anti- τ_{had}) corresponds to the required multiplicity in each channel. For channels where τ_{had} -ID is applied at trigger level (more details in Section ??), only the anti- τ_{had} objects that are matched to the trigger τ_{had} are considered, and thus there are no multiple selection possibilities. However, for channels where a τ_{had} trigger is not used, an anti- τ_{had} candidate is chosen randomly when there are more reconstructed τ_{had} satisfying the anti- τ_{had} definition. Any anti- τ_{had} objects that are not selected in this process are also not considered when performing the overlap removal of detector objects, which is discussed in Section 5.7.

5.6 Missing transverse energy

As defined in Equation 3.2.1, the \vec{E}_T^{miss} is defined as the negative vector sum of transverse momentum collected from the detector, from which one or more “invisible” particle(s) can be inferred. The reconstruction of \vec{E}_T^{miss} is comprised of two contributions [61]. The first one is from *hard-event* signals combining information of fully reconstructed and calibrated physics objects, i.e. electrons, muons, photons, jets, hadronically decaying τ -leptons and jets. The second one is from the *soft-event*, consisting of reconstructed charged-particle tracks associated with the hard-scatter vertex but with no physics objects.

5.7 Overlap removal

After the event is reconstructed, an overlap-removal procedure is applied to resolve ambiguities when a physical object is reconstructed as multiple particles in the ATLAS detector. The angular distance ΔR is used to measure the overlap of two reconstructed objects. Overlaps between most of the detector objects used in the analysis are resolved by using the standard overlap removal tools AssociationU-tils [62], with analysis specific procedure for the reconstructed $\tau_{had-vis}$, anti- $\tau_{had-vis}$

objects and jets. The step-by-step procedure that is used to resolve ambiguities in the reconstructed objects is summarised in the following:

- e_1-e_2 : For two electrons e_1 and e_2 in an event, reject e_1 if both electrons share the track and $p_{T1} < p_{T2}$
- $\tau_{had-vis}-e$: Reject $\tau_{had-vis}$ if $\Delta R < 0.2$
- $\tau_{had-vis}-\mu$: Reject $\tau_{had-vis}$ if $\Delta R < 0.2$:
 - Case 1 ($\tau_{had-vis} p_T > 50\text{GeV}$): $p_T, \mu > 2\text{GeV}$ and combined muon
 - Case 2 ($\tau_{had-vis} p_T \leq 50\text{GeV}$): $p_T, \mu > 2\text{GeV}$
- $\mu-e$: Reject μ if calo-muon and shared ID track
- $e-\mu$: Reject e if shared ID track
- jet- e : Reject jet if $\Delta R < 0.2$
- e -jet: Reject e if $\Delta R < 0.4$
- jet- μ : Reject jet if $N_{track} < 3$ ($p_T^{track} > 500\text{MeV}$), and $\Delta R < 0.2$
- μ -jet: Reject μ if $\Delta R < 0.4$

Additionally, an analysis-specific overlap-removal procedure for $\tau_{had-vis}$, anti- $\tau_{had-vis}$ and jets is implemented:

- jet- $\tau_{had-vis}$: Reject jet if $\Delta R < 0.2$
- anti- $\tau_{had-vis}$ -jet: Reject anti- τ_{had} if jet is b -tagged and $\Delta R < 0.2$
- jet-anti- $\tau_{had-vis}$: Reject jet if $\Delta R < 0.2$

This establishes the following priority: $\tau_{had-vis} > b$ -tagged jet $>$ anti- $\tau_{had-vis}$ $>$ untagged jet.

Chapter 6

Charm jet mis-tagging calibration

6.1 Calibration methods for b jet and light jet

MC simulations are not able to model exactly the performance of the b -tagging algorithms in data. For this reason calibration is required, i.e. correcting MC to recover the data in terms of b -tagging efficiency, charm jet mis-tagging and light jet mis-tagging rates [52]. The calibration is performed for all supported jet collections(TODO: refer back to the object definition chapter) and working points, which are cuts in the b -tagging algorithm output identifying the different tagging efficiencies and corresponding light jet and c jetrejection rate. In general, the efficiency is calculated with data and simulations, and scale factors are then calculated to match the efficiency extracted from simulations to the data. The production of $t\bar{t}$ pairs at the LHC provides an abundant source of b jets by virtue of the high cross-section and the $t \rightarrow Wb$ branching ratio being close to 100%. A very pure sample of $t\bar{t}$ events can be selected by requiring that both W bosons decay leptonically, referred to as di-leptonic $t\bar{t}$ decays in the following. For the b jet calibration, the performance of the b tagging algorithms is evaluated in the simulation and the efficiency with which these algorithms identify jets containing b -hadrons is measured in collision data. The measurement uses a likelihood-based method in the di-leptonic $t\bar{t}$ sample, where events with exactly 2 jets and 2 opposite-sign leptons are selected. The data b jet efficiency is then extracted from a combined likelihood fit, and subsequently compared with that predicted by the simulation. Scale factors are then calculated to emulate the performance of the algorithms to the data [52].

For the light jet mis-tagging calibration, two methods are used to measure the mis-tagging rate from the data [63]. The first is the negative tag method, which uses a high statistics data sample enriched in light jets with the application of a modified algorithm which reverses some of the criteria used in the nominal identifi-

cation algorithm. The second is the adjusted Monte Carlo (adjusted-MC) method, which adjusts the characteristic track observables in the simulation to im the data, and then compares the adjusted simulation to the “standard” simulation. The scale factors are then calculated using the these two methods. The scale factors of the two different methods are in good agreement within the systematic uncertainties.

6.2 Calibration method for c jet

It is worth mentioning that the author’s qualification task to become an ATLAS author is to calibrate the rate of a charm jet being mis-identified as a b jet which is a part of the calibration of the b -tagging algorithm. During the task the calibration range has been extended down to 20 GeV (previously 25 GeV) in jet p_T and a new selection category has been developed to increase the data statistics of the scale factors in the high- p_T ($p_T^{jet} > 70$ GeV) region. The calibration is performed on the PFlow jets (as defined in Section 5.4) and *VR-Track jets* reconstructed using the variable radius jet algorithm [64].

As determined by the CKM matrix [65, 66], the W boson decays dominantly to a pair of light quarks (u quark and d quark) or to a s quark and a c quark. The W boson decays very rarely to pairs containing a b quark. More specifically, the branching ratio of a W boson decays to a u quark and d quark pair or a s quark and c quark pair is 33.1%, and to pairs containing a b quark is only 0.057% [56]. Therefore, b -tagged jets from the W decay are most likely to be mis-tagged c jets or light jets.

Furthermore, given the ratio between the DL1 light jet rejection and the corresponding charm jet rejection ranges from 10 to 40 (Figure 5.7), the c jet is much more likely to be mis-tagged than the light jet. This allows for a source of mis-tagged c jets to be obtained in the $t\bar{t}$ events, requiring that one W boson decays leptonically and the other decay hadronically (referred to as semi-leptonic $t\bar{t}$ decay in the following), where the b -tagged jets from the W decay are candidates of mis-tagged c jets. Requiring a W boson decaying leptonically reduces the number of combinations of jets of different flavour, and allows triggering with the lepton.

The events kinematics are shown by the diagram in Figure 6.1, where the $t\bar{t}$ pair decays to a b and a \bar{b} quark, circled in red. One of the W bosons, circled in blue, decays hadronically to quarks, and the other W boson decays leptonically to either an electron or a muon and the corresponding neutrinos, circled in green and purple, respectively. The lepton in the final state is used for triggering. The following notation will be used: the jets that are the decay products of the W boson

are referred to as W jets and the remaining two jets are referred to as top-jets.

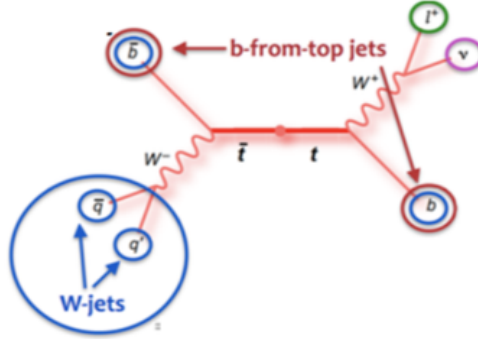


Figure 6.1: Feynman diagram of the semi-leptonic $t\bar{t}$ events.

A kinematic likelihood technique, referred to as KLFitter [67], is used to assign jets to the proper $t\bar{t}$ decay product (more details in Section 6.4). The following notation will be used: the jets that are assigned as the decay products of the W boson are referred to as W jets and the remaining two jets are referred to as top jets.

The charm jet efficiency is defined as the ratio of events with either of the W jet is tagged. The efficiency is evaluated in four p_T intervals, with boundaries of 20, 40, 65, 140 and 250 GeV for the PFlow jets and 15, 20, 40, 140 GeV for the VR-Track jets; and for four tagging intervals with the boundaries of 85%, 77%, 70% and 60%.

The choice of the bin boundaries ensures enough statistics for each bin and hence relatively flat statistical uncertainty, given the underlying charm-jet p_T spectrum as shown in Figure 6.7. The boundaries for the VR-Track jets are lower than for PFlow jets, since the track jets miss the neutral particles the reconstructed energy is significantly below the true jet energy.

The main method described in the chapter is for the “fixed-cut” calibration where the efficiency is defined as the fraction of b jets passing the tagger. Jets are said to be tagged (untagged) at particular working point if they have DL1r scores greater (less) than the DL1r score of that working point. The events with both W jet are discarded to simplfy the fit described in the following.

To extract the scale factors of the charm jet mis-tagging, a fit is performed by minimising the χ^2 defined as:

$$\chi^2 = \sum_{t=1}^4 \sum_{i=1}^4 \sum_{j=1}^4 (N_{\text{data}}^t(i,j) - p(i,j)[c^t(i)N_C^t(i,j) + N_J^t(i,j)])^2$$

$$\begin{aligned}
& + \sum_k c^4(k) N_X^t(i, j, k)])^2 / N_{\text{data}}^t(i, j) \\
& + \sum_{i=1}^4 \sum_{j=i}^4 [N_{\text{data}}^{\text{untag}}(i, j) - p(i, j) N_{\text{MC}}^{\text{untag}}(i, j)]^2 / N_{\text{data}}^{\text{untag}}(i, j). \tag{6.1}
\end{aligned}$$

The $c^t(i)$ is the main floating parameter in the fit, which is the charm jet mis-tagging scale factor at working point t of p_T bin labelled i . The other main floating parameter is $p(i, j)$ that is the normalisation factor scaling the MC to data. The $N_{\text{data}}^t(i, j)$ is the number of data events with a tagged W jet in the p_T bin labelled i and the other (un-tagged) W jet in the p_T bin labelled j . Similarly the $N_C^t(i, j)$ is the number of MC events with a tagged W jet while the tagged W jet is indeed a c jet which can be seen as “signal”. In contrast the $N_J^t(i, j)$ is the number of events with neither the tagged W jet nor the top jets are c jets and the $N_X^t(i, j, k)$ is the number of events with one of the top jets is a c jet. These two types of events can be seen as “background”. The later case is slightly more complicated, as the c jet lies in a different p_T bin to the tagged jet, denoted as k , and it only depends on the $c^4(k)$ (which is the scale factor of the 4th working point i.e. 60%) as the top jets are tagged at 60% working point. The calibration is then given as the scale factors of the four working points in bins of p_T defined in the above text.

6.3 Data and Monte Carlo samples

TODO: remove the overlap between this section and the Data MC chapter in the thesis Dedicated MC are used to model SM processes. The data analysed in this study correspond to 139 fb^{-1} [68–71], of pp collision data collected by the ATLAS detector between 2015 and 2018 with a centre-of-mass energy of 13 TeV. The data sample was collected using a set of single-muon [72] and single-electron triggers [73]. The single-muon triggers had p_T thresholds in the range 20–26 GeV for isolated muons and 50 GeV for muons without any isolation requirement. The single-electron triggers employed a range of p_T thresholds varying between 24–300 GeV and a combination of quality and isolation requirements depending on the data-taking period and the p_T threshold. All detector subsystems were required to be operational during data taking and to fulfil data quality requirements.

All samples were produced using the ATLAS simulation infrastructure [74] and GEANT4 [75]. A subset of samples use a faster simulation based on a parameterisation of the calorimeter response and GEANT4 for the other detector systems [74].

The simulated events are reconstructed with the same algorithms as used for data, and contain a realistic modelling of pile-up interactions. The pile-up profiles in the simulation match those of each dataset between 2015 and 2018, and are obtained by overlaying minimum-bias events, simulated using the soft QCD processes of PYTHIA 8 [76] using the NNPDF2.3LO set of PDFs [77] and a set of tuned parameters called the A3 tune [78].

The events that are used in this study originate mostly due to $t\bar{t}$ production. This process is modelled using the POWHEGBOX v2 [79–82] generator at NLO with the NNPDF3.0nlo parton distribution function (PDF) set and the h_{damp} parameter¹ set to $1.5 m_{\text{top}}$ [83]. The events were interfaced to PYTHIA 8.230 to model the parton shower, hadronisation, and underlying event, with parameters set according to the A14 tune and using the NNPDF2.3lo set of PDFs. The decays of bottom and charm hadrons were performed by EVTGEN v1.6.0 [84]. The simulated $t\bar{t}$ events are split according to the origin of W jets. The notation “ $t\bar{t}, \text{ll}$ ” denotes that both W jets are light flavour jets. Similarly, “ $t\bar{t}, \text{cl}$ ” (“ $t\bar{t}, \text{bl}$ ”) indicates that one of the W jets is a c jet (b jet) whereas the other is a light flavour jet. W jets with origin other than what is discussed above fall into the category denoted by “ $t\bar{t}, \text{other}$ ”. This category includes events in which at least one of the W jets comes from a hadronically decaying τ -lepton.

In addition to $t\bar{t}$ production, there are some minor backgrounds that contribute to the final event sample that is used for the calibration. These backgrounds consist mostly of single-top and diboson production, the production of $t\bar{t}$ in association with a vector boson and the production of a vector boson in association with jets. The details of the modeling of these samples are given in the following.

Single-top s -channel production is modelled using the POWHEGBOX v2 generator at NLO in QCD in the five-flavour scheme with the NNPDF3.0nlo [85] parton distribution function (PDF) set. The associated production of top quarks with W bosons (tW) is modelled using the POWHEGBOX v2 [80–82, 86] generator at NLO in QCD using the five-flavour scheme and the NNPDF3.0nlo set of PDFs [85]. The diagram removal scheme [87] is used to remove interference and overlap with $t\bar{t}$ production. The events for both single-top s -channel and tW production are interfaced to PYTHIA8.230 using the A14 tune and the NNPDF2.3lo set of PDFs.

The production of $Z + \text{jets}$ and $W + \text{jets}$ is simulated with the SHERPA v2.2.1 [88] generator using next-to-leading order (NLO) matrix elements (ME) for up to two partons, and leading order (LO) matrix elements for up to four partons calculated

¹The h_{damp} parameter is a resummation damping factor and one of the parameters that controls the matching of POWHEG matrix elements to the parton shower and thus effectively regulates the high- p_T radiation against which the $t\bar{t}$ system recoils.

with the Comix [89] and OPENLOOPS [90–92] libraries. They are matched with the SHERPA parton shower [93] using the MEPS@NLO prescription [94–97] using the set of tuned parameters developed by the SHERPA authors. The `NNPDF3.0nnlo` set of PDFs [85] is used and the samples are normalised to a next-to-next-to-leading order (NNLO) prediction [98].

Samples of diboson final states (VV) are simulated with the SHERPA v2.2.1 or v2.2.2 [88] generator depending on the process, including off-shell effects and Higgs-boson contributions, where appropriate. Fully leptonic final states and semileptonic final states, where one boson decays leptonically and the other hadronically, are generated using matrix elements at NLO accuracy in QCD for up to one additional parton and at LO accuracy for up to three additional parton emissions. Samples for the loop-induced processes $gg \rightarrow VV$ are generated using LO-accurate matrix elements for up to one additional parton emission for both cases of fully leptonic and semileptonic final states. The matrix element calculations are matched and merged with the SHERPA parton shower based on Catani-Seymour dipole factorisation [89, 93] using the MEPS@NLO prescription [94–97]. The virtual QCD correction are provided by the OPENLOOPS library [90–92]. The `NNPDF3.0nnlo` set of PDFs is used, along with the dedicated set of tuned parton-shower parameters developed by the SHERPA authors.

The production of $t\bar{t}$ in association with a vector boson is modelled using the `MADGRAPH5_aMC@NLO` v2.3.3 [99] generator at NLO with the `NNPDF3.0nlo` [85] parton distribution function (PDF). The events are interfaced to PYTHIA8.210 [76] using the A14 tune [100] and the `NNPDF2.3l0` [85] PDF set. The decays of bottom and charm hadrons are simulated using the `EVTGEN` v1.2.0 program [101].

6.4 Kinematic Likelihood Fitter

The four-vectors of the four highest p_T jets, the lepton and the event E_T^{miss} are used as inputs to a likelihood-based $t\bar{t}$ event reconstruction algorithm, which is described in more detail in Ref. [67]. This algorithm uses a likelihood function to assign the four jets to the $t\bar{t}$ decay topology. In particular, the algorithm assigns one jet to be the b jet from the leptonically decaying top quark ($t \rightarrow Wb \rightarrow \ell\nu b$), another to the b jet from the hadronically decaying top quark ($t \rightarrow Wb \rightarrow qq'b$, where qq' are the quarks in which the W boson decays) and the remaining two jets to the jets that come from the hadronic W boson decay. The jet assignment does not use any b -tagging information to avoid bias.

6.5 Maximising likelihood

Taking only four jets in the event limits the total number of possible jet orderings (permutations) in the event. In the semi-leptonic channel, four jets can be permuted a total number of times equal to $4! = 24$. However, the two W jets are kinematically indistinguishable. This reduces the possible number of permutations to 12. For every combination of jet ordering, the likelihood is maximised over its free parameters, the energy of the four jets, the lepton energy and the three components of the momentum of the neutrino, and provides a value based on how closely the kinematic information from the reconstructed objects for a specific jet ordering resembles the expected kinematic behaviour of the decay of a Standard Model semi-leptonic $t\bar{t}$ event. The likelihood therefore distinguishes the possible permutations on an event-by-event basis. The best permutation, given by the largest log-likelihood value, is adopted as the jet ordering for the event. An additional requirement of $\log\text{-likelihood} > -48$ is

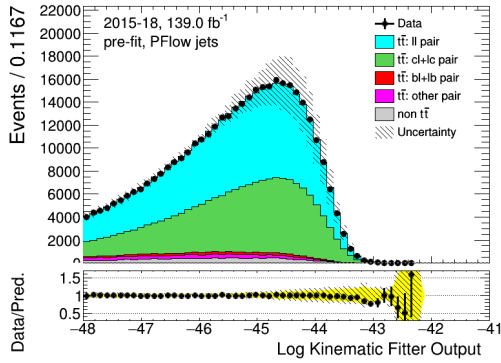


Figure 6.2: Distribution of the negative logarithm of the likelihood that is used to reconstruct the $t\bar{t}$ decay.

placed on the output of the likelihood value for the chosen event permutation. An example of the distribution of log-likelihood of the best permutations is shown in Figure 6.2. In this figure, the data events are compared against the simulation. The majority of the events come from $t\bar{t}$ production. There is only a very small fraction of events, which is denoted as “non $t\bar{t}$ ” on the figure, that come from other processes like W or Z production in association with jets or single-top production.

6.6 Event selection

6.6.1 Standard selection

Events are required to contain exactly one trigger-matched lepton with $p_T > 27$ GeV and exactly four jets with $p_T > 25$ GeV. Leptons are required to have p_T above

27 GeV in order to avoid the turn-on curve for the single lepton triggers. Events which contain an additional lepton with $p_T > 27$ GeV are rejected. The events are also required to have $E_T^{\text{miss}} > 20$ GeV, which is assumed to be the result of the neutrino from the leptonically decaying W boson. The transverse mass m_T between the lepton and the E_T^{miss} , is constrained as follows:

$$m_T = \sqrt{2p_T^\ell E_T^{\text{miss}}(1 - \cos \Delta\phi)} > 40 \text{ GeV},$$

where $\Delta\phi = \phi(E_T^{\text{miss}}) - \phi(\ell)$ is the azimuthal difference between the lepton and E_T^{miss} .

The yields of the data and the MC are given in Table 6.1. An example of the p_T

	PFlow jets	Track jets
Data	227118	218351
$t\bar{t}$	235670 ± 200	223770 ± 180
Non $t\bar{t}$	7610 ± 120	7280 ± 100
Data/MC	0.934 ± 0.002	0.945 ± 0.002

Table 6.1: Standard selection: prefit comparison of the number of events in data and in simulation considering the PFlow jets and the VR-Track jets for events with exactly 4 jets.

distributions before any tagging or fitting and after the standard selection is shown in Figure 6.3. More plots can be found in Appendix A.1.1. The yellow band in the lower pad shows the overall systematic uncertainties, combining the experimental uncertainties and the $t\bar{t}$ modelling uncertainties, as described in Section 6.7. The data/MC ratio shows good agreement within the systematic uncertainties.

6.6.2 Low- p_T selection

The author has developed an orthogonal selection to extend the calibration in the low- p_T region so that the calibration can be applied to PFlow jets with $20 < p_T < 25$ GeV. The p_T threshold of the VR-Track jets is 10 GeV therefore the low- p_T selection is not needed. Instead of requiring events to have exactly 4 jets $p_T > 25$ GeV, events are required to have exactly 3 jets with $p_T > 25$ GeV and exactly 1 jet with $25 \text{ GeV} > p_T > 20 \text{ GeV}$. Other than that, all requirements for the selection are the same. This additional cut provides candidates for the PFlow W jet that is used for calibration in the $20 - 25$ GeV region. The inclusive yields of the low- p_T selection of the data and the MC are given in Table 6.2, and the p_T distributions of the W jets are shown in Figure 6.4. More plots of the kinematic distributions are shown in Appendix A.1.2. Good agreement between MC and data is shown in these distributions, and the p_T range of the sub-leading has gone down to 20 GeV.

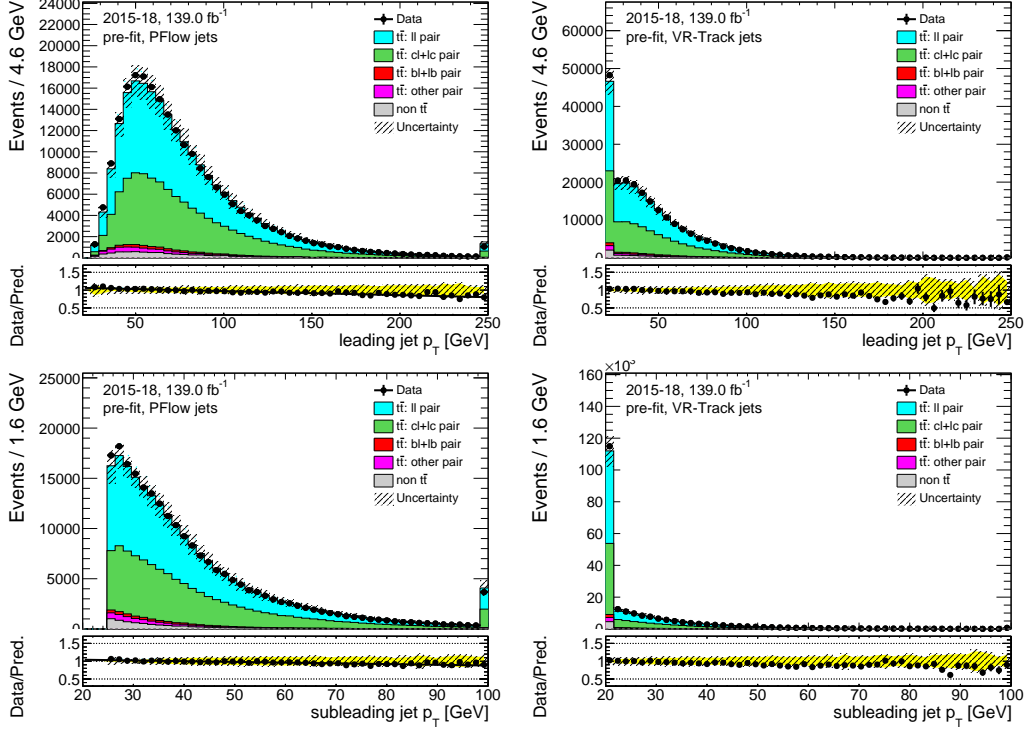


Figure 6.3: Standard selection: data versus simulation of the leading and sub-leading W jet p_T for the PFlow jets in the left column and for VR-Track jets in the right column. The leading jet and sub-leading jet refer to the highest p_T W jet and the second highest p_T jet, respectively. The 'non $t\bar{t}$ ' background indicates background comes from non- $t\bar{t}$ processes like W or Z production in association with jets or single-top production. The error in the table (and the following yields tables for different selection) is stats-only.

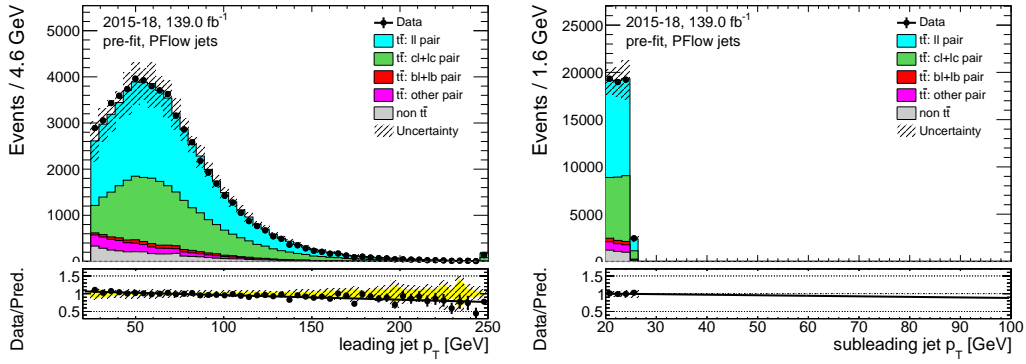


Figure 6.4: Low- p_T selection: data versus simulation of the PFlow W jets p_T .

6.6.3 High- p_T selection

It has been observed that in the previous calibrations that the statistics are relatively low for the high- p_T region (e.g. jet $p_T > 100$ GeV). Therefore, the author has worked

	PFlow jets
Data	59987
$t\bar{t}$	56530 ± 90
Non $t\bar{t}$	3340 ± 60
Data/MC	1.002 ± 0.004

Table 6.2: Low- p_T selection: prefit comparison of the number of events in data and MC for the PFlow W jets. Events are required to have exactly 3 jets with $p_T > 25$ GeV and one jet with $20 < p_T < 25$ GeV.

on an orthogonal selection to improve this situation. Instead of requiring events to have exactly 4 jets, events are required to have at least 5 jets with $p_T > 25$ GeV, in which at least 1 jet with $p_T > 70$ GeV. Other than that, all requirements for the selection remain the same.

The choice of cut value at 70 GeV is based on the study shown in the following. The effect on the c jet purity and the potential statistical gain is investigated, where the c jet purity is defined as:

$$c \text{ jet purity} = \frac{N_{\text{true } c \text{ jet}}}{N_{\text{all}}}, \quad (6.2)$$

where $N_{\text{true } c \text{ jet}}$ stands for the number of events with a true c jet from the W decay, and N_{all} stands for the number of all events. The ideal situation is the high- p_T selection will maximally increase the statistics while minimally decreasing the c jet purity, therefore a figure of merit P^{Cut} is defined as:

$$P^{\text{Cut}} = \frac{\sum_i \text{Gain in stats}_i^2}{\sum_i c \text{ jet purity}_i^2},$$

where i stands for the number of bins. The “Gain in stats” stands for increase in statistics and it’s summed over all bins in Figure 6.5. The c jet purity and the statistical gain are calculated for 4 different cut values as shown in Figure 6.5, comparing with the cut value of 0. The value of 70 GeV is chosen as it gives the highest value of P^{Cut} .

	PFlow jets	Track jets
Data	98273	83957
$t\bar{t}$	99430 ± 120	87476 ± 110
Non $t\bar{t}$	1842 ± 21	1570 ± 20
Data/MC	0.97 ± 0.003	0.94 ± 0.003

Table 6.3: High- p_T selection: prefit comparison of the number of events in data and in simulation considering the PFlow W jets and the VR-Track jets.

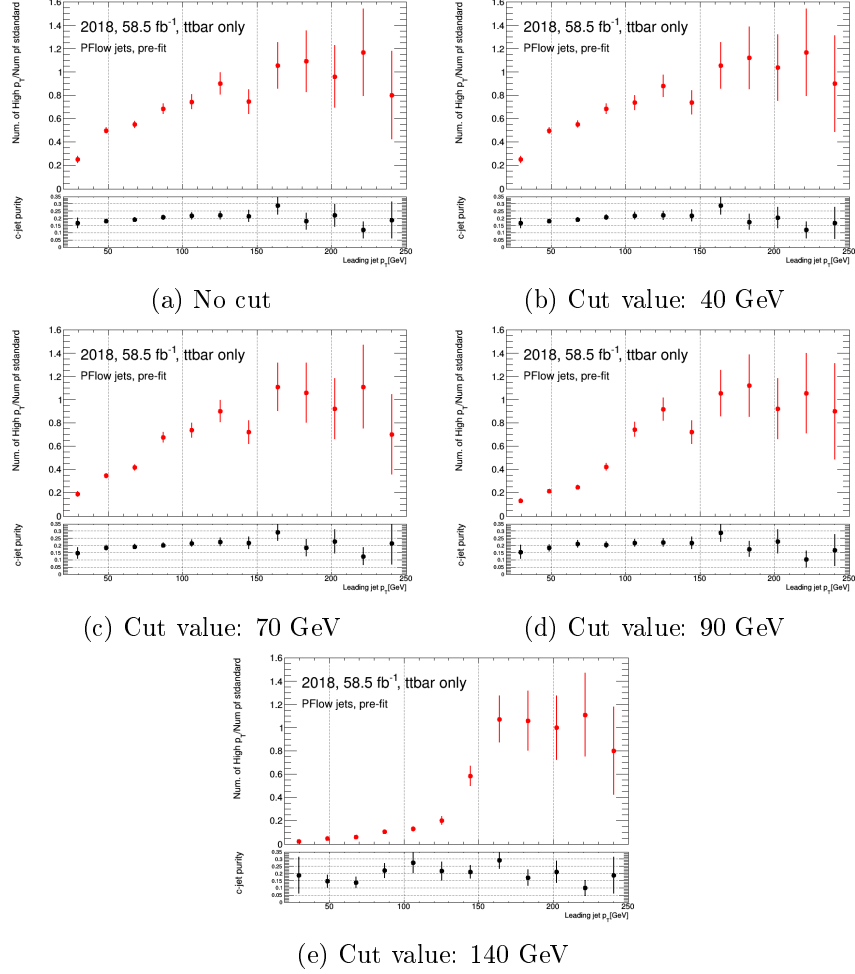


Figure 6.5: Comparison of different cut values in terms of gain in stats and c jet purity.

The yields of the data and the MC are given in Table 6.3. An example of the p_T distributions before any tagging or fitting, applying the high- p_T selection is shown in Figure 6.6. In general the event statistics improve about 80% in region with $p_T > 70$ GeV as desired. More plots can be found in Appendix A.2.

6.6.4 Combined selection

As the standard selections, low- p_T selection and high- p_T selection are orthogonal to each other, all the selections are combined to provide the maximum range and statistics for the calibration. The yields of the data and the MC are given in Table 6.4, an example of the p_T distributions before any tagging or fitting and after the combined selection is shown in Figure 6.7. More plots can be found in Appendix A.3.

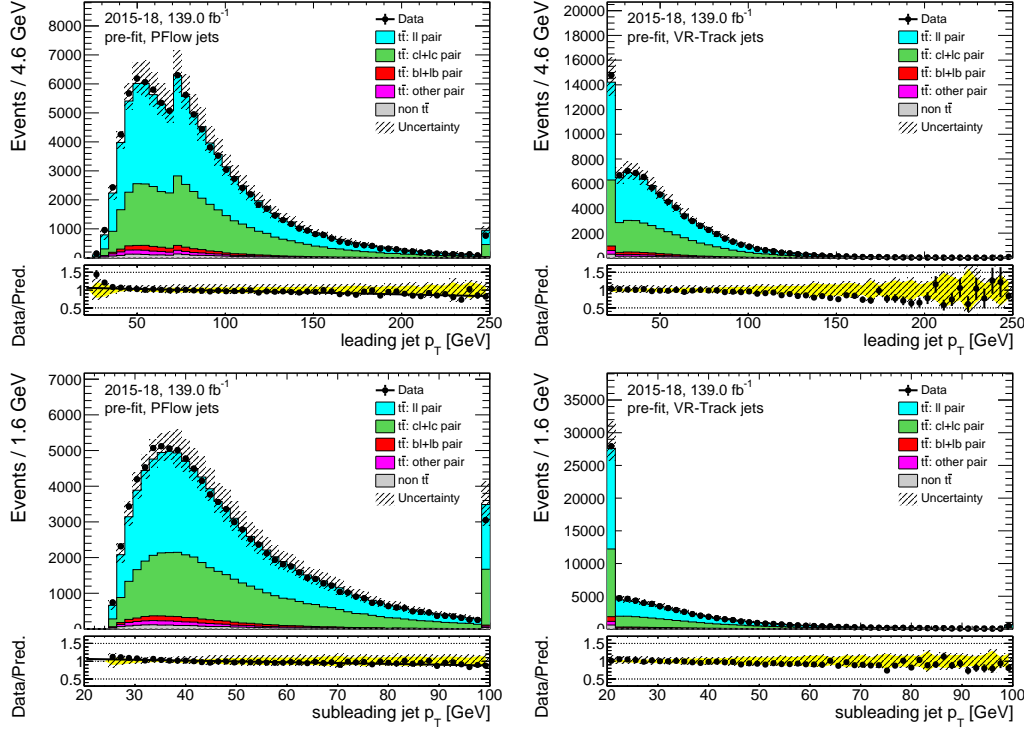


Figure 6.6: High- p_T selection: data versus simulation of W jets p_T for PFlow jets in the left column and for VR-Track jets in the right column.

	PFlow jets	Track jets
Data	385378	302308
$t\bar{t}$	383520 ± 230	302690 ± 200
Non $t\bar{t}$	12420 ± 120	8570 ± 100
Data/MC	0.973 ± 0.002	0.971 ± 0.002

Table 6.4: Combined selection: prefit comparison of the number of events in data and in simulation considering the PFlow jets and the VR-Track jets for an inclusive selection.

6.7 Systematic uncertainties

The systematic uncertainties considered and propagated in this calibration can be broadly categorised into experimental and modelling systematic uncertainties.

6.7.1 Experimental uncertainties

TODO: refer to the analysis Part Experimental uncertainties are related to the detector and estimated using data-driven methods or MC simulations. The lepton energy scale and resolution are corrected to provide better agreement between MC predictions and data, uncertainties due the corrections are considered. Uncertainties are taken into account on the electron and muon trigger, identification and reconstruc-

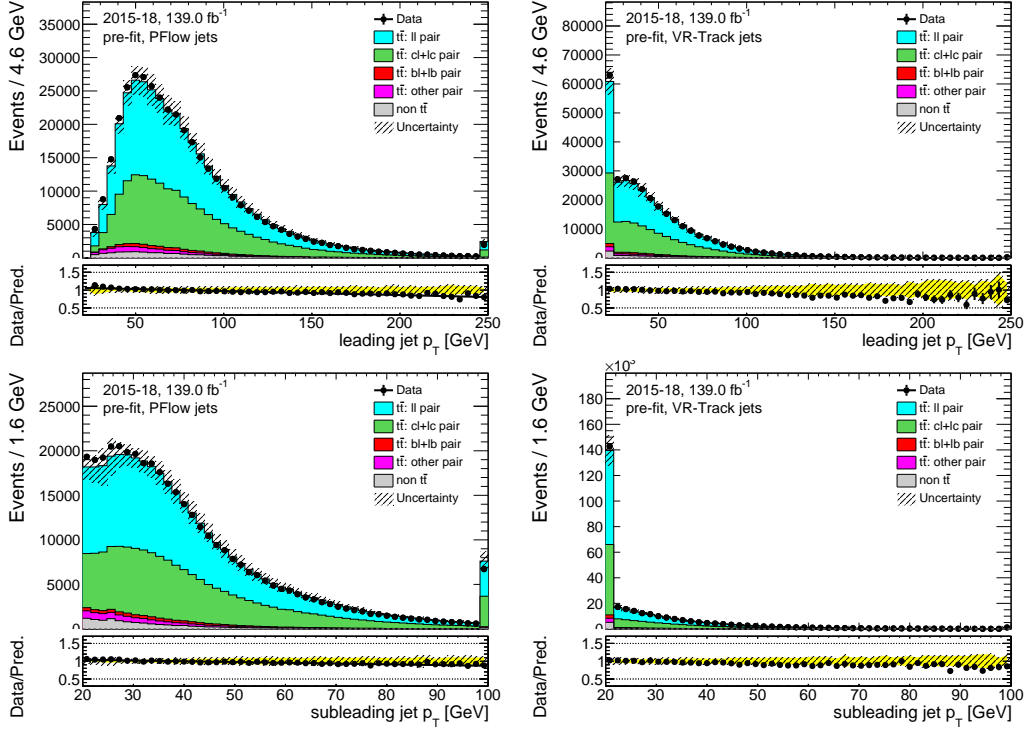


Figure 6.7: Combined selection: data versus simulation of W jets p_T for PFflow jets in the left column and for VR-Track jets in the right column.

tion efficiencies, and for uncertainties associated with the isolation requirements.

The jet energy scale (JES) uncertainty depends on p_T and η and takes into account uncertainties due to pile-up effects. Uncertainties on the jet energy resolution (JER) are taken into account. Uncertainties on the energy scale and resolution of the electrons, muons, jets and taus are propagated to the calculation of the E_T^{miss} , which also has additional dedicated uncertainties on the scale, resolution, and reconstruction efficiency of tracks not associated to any of the reconstructed objects, along with the modelling of the underlying event. Uncertainties on the b -tagging (mis-tagging) probabilities for b (light) jets are considered both for the tagging jets assigned to the b quark from the top decay and for the jets associated to the hadronically decaying W boson. Supporting material for this section can be found in the appendix, Tab.A.1.

6.7.2 Modelling uncertainties

The uncertainty due to different choices of the parton shower models is estimated by comparing the MC samples generated with nominal parton shower model and with the alternative parton shower model. More specifically, it is derived by comparing the prediction from POWHEG interfaced either to PYTHIA8 or Herwig++. The uncer-

tainty due to additional radiation in the initial state and the final state is estimated by comparing the nominal MC samples with the MC samples with alternative scale of renormalisation and factorisation. The uncertainty on modelling of initial state radiation (ISR) is assessed with two alternative POWHEG+PYTHIA8 samples. The samples include one with an increase in radiation which has the renormalisation and factorisation scales decreased by a factor of two and the $hdamp$ parameter doubled (which controls the p_T of the first additional emission), while the sample with a decrease in radiation has the scales increased by a factor of two. In all cases, MC-to-MC SFs are taken into account. In addition, the uncertainty due to the variations samples being produced by fast simulation while the nominal samples being produced full simulation is also considered. The comparisons of the nominal $t\bar{t}$ sample and the samples with each systematic uncertainty are shown in Table 6.5.

	PFlow jets		Track jets	
	Yields	Ratio of difference to nominal sample	Yields	Ratio of difference to nominal sample
$t\bar{t}$ Nominal Data/MC	385378 ± 230 0.973 ± 0.002		302690 ± 200 0.971 ± 0.002	
$t\bar{t}$ AF2 DATA/MC(AF2)	386260 ± 250 0.967 ± 0.002	0.716%	304860 ± 230 0.965 ± 0.002	0.716%
$t\bar{t}$ ISR DATA/MC(ISR)	377130 ± 220 0.989 ± 0.002	-1.665%	297960 ± 200 0.986 ± 0.002	-1.562%
$t\bar{t}$ Herwig DATA/MC(Herwig)	331960 ± 220 1.119 ± 0.002	-13.443%	259940 ± 190 1.126 ± 0.002	-14.123%

Table 6.5: Comparison of the number of events in data and in simulation considering the PFlow jets and the VR-Track jets for an inclusive selection. The uncertainty due to the variations samples being produced by fast simulation is included in the table as $t\bar{t}$ AF2.

6.8 Under-estimation of $t\bar{t}$ + Heavy flavour background

Despite the fact that the true nature of most of the reconstructed W jets are either c jets or light jets, there is still a very small amount of them are true b jets.

There are two main sources of these true b jets. The first is a W boson decays to a b and a c quark. The second is when the $t\bar{t}$ plus a gluon process (referred to as $t\bar{t}$ + heavy flavour process) is selected, and the gluon splits into a pair a b quarks and one of them is assigned as a W jet. The first source can be excluded by requiring no c jets in the W jets, meaning the true b jet in the W jets can only come from the $t\bar{t}$ + heavy flavour process. This process is underestimated by the MC by about 30% for both the PFlow and VR-Track jets collections, as shown in Table 6.6 and Figure 6.8, where an extra cut requiring at least one W jet with $DL1r > 8$ is added

to the combined selection to reject most of the true c jets and true light jet. A more thorough study is done in Ref. [102], where the mis-modelling factor is measured to be 1.25 ± 0.25 , which is also consistent with the 30% mismodelling observed in the previous study. Therefore, events in the simulation in which the top jets and at least one of the W jets are b jets (referred to as 3 true b jets events), are scaled by 1.25 ± 0.25 . All results shown in this chapter have this scale factor implemented, and the full difference between the simulation before applying this scale factor and after is taken as a systematic uncertainty. This uncertainty has been added in quadrature to the systematic uncertainties described in Section 6.7 in all the plots in this chapter.

	PFlow jets	VR-Track jets
Data	1589	1336
$t\bar{t}$	1100 ± 13	940 ± 12
Non $t\bar{t}$	83 ± 6	69 ± 5
Data/MC	1.34 ± 0.04	1.32 ± 0.04

Table 6.6: Yields of the 2018 data and MC of the combined selection, requiring at least 1 PFlow or track W jet with $\text{DL1r} > 8$ to reject most of the light- and c jets.

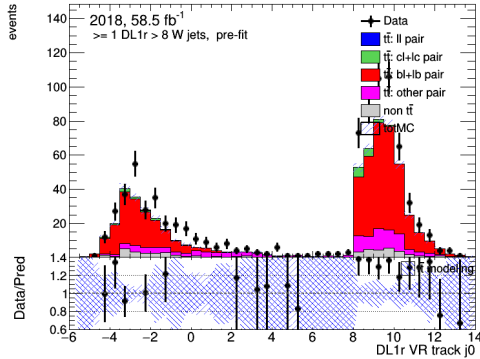


Figure 6.8: The DL1r score distribution of the leading VR-Track jet, requiring at least 1 VR-Track jets have $\text{DL1r} > 8$ to reject most of the light and the c jets, with $t\bar{t}$ modelling and statistical uncertainties.

6.9 Results

6.9.1 Overview

Four rounds of calibrations have been carried out, containing different jet collections, Monte Carlo samples, analysis framework and b jet identification algorithm. In the latest round, the calibration includes the PFlow jet and the VR-Track jet collection, and MV2c10, DL1 and DL1r taggers. The low- p_T selection and the standard

selection are carried out for all four calibrations, while the high- p_T selection is only implemented in the latest calibration.

6.9.2 b -tagging algorithms output distribution

The distributions of the b -tagging algorithm’ output of the MC and the data of the latest calibration (December 2020) are shown in Figure 6.9 for the PFlow jets and Figure 6.10 for the VR-Track jets, combining the standard selection, low p_T and the high- p_T selection. In these figure, the data events are compared against the simulation. The majority of the events come from $t\bar{t}$ production. There is only a very small fraction of non $t\bar{t}$ events. The W jets pairs are mostly light jets pairs and c jet light jet pairs, and a very small fraction of the pairs are b jet light jet pairs or pairs containing one or more τ hadron(s). The yellow band in the lower pad indicates the overall systematic uncertainties and the black band represents the $t\bar{t}$ modelling systematic uncertainty, which dominates at low b -tagging discriminant (DL1 or DL1r < 4). The experimental systematic uncertainty is in general very small. At high b -tagging discriminant (DL1 or DL1r > 4), the uncertainty due to the 1.25 ± 0.25 scale factor becomes more important.

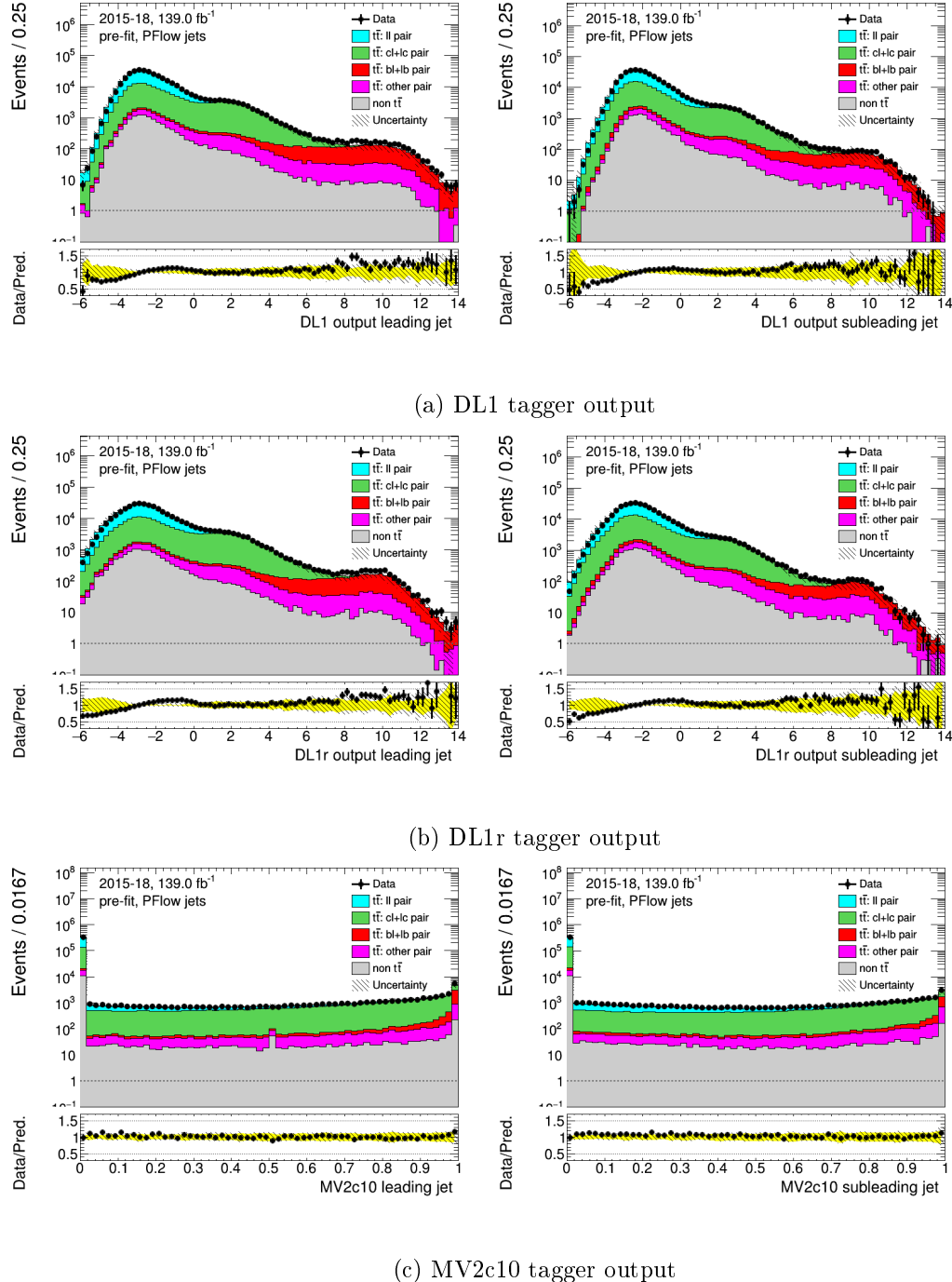


Figure 6.9: PFlow jets: distributions of the DL1, DL1r and MV2c10 tagger outputs of the combined selection, leading jet in the left column and sub-leading jet in the right column, before fitting or tagging with full uncertainties.

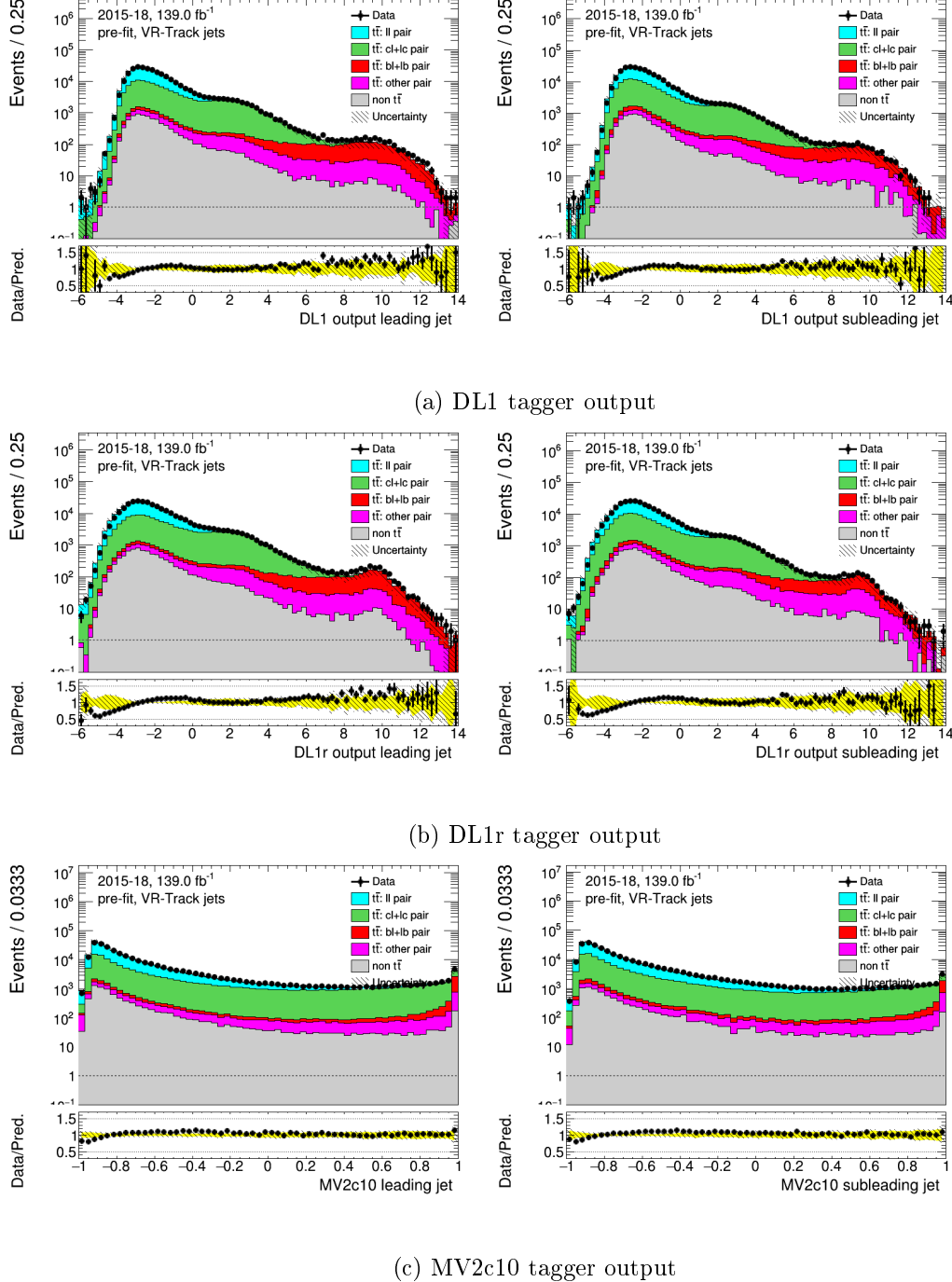


Figure 6.10: VR-Track jets: distributions of the DL1, DL1r and MV2c10 tagger outputs of the combined selection, leading jet in the left column and sub-leading jet in the right column, before fitting or tagging with full uncertainties.

6.9.3 Efficiencies and Scale Factors

The DL1 and DL1r c jet efficiencies and scale factors with systematics uncertainties are calculated with four fixed cut working points for the PFlow and VR VR-Track jets collection in the latest derivation in December 2020.

The c jet mis-tagging efficiencies are shown in Figure 6.11-6.14 for the PFlow jet collections and the VR-Track jets with the DL1 and the DL1r tagger. For PFlow jets, these results combine the standard selection, low- p_T selection and the high- p_T selection and for the VR-Track jets they combine the standard selection and the high- p_T selection.

The 1.25 ± 0.25 scale factor is applied on events with 3 true b jets. The overall uncertainties are shown in the red band. The scale factors are shown in Figure 6.15-6.18 for the PFlow jets and the VR-Track jets with the DL1 and DL1r tagger. The tighter working points (60%, 70%) show larger uncertainties and bigger deviation from 1, while the looser working points (77%, 85%) have much smaller uncertainty and the simulation is able to recover the data well due to more abundant events statistics. For the PFlow jets, in most of the working points the systematic uncertainties dominate in the low- p_T bins ($p_T < 150$) and the statistical error, represented by the error bars on the markers, become more important in the last bin. For the VR-Track jets the statistical uncertainty is relatively constant for all bins while the systematic uncertainty increases as the p_T increases. To demonstrate the effect on statistics with the high- p_T selection, the fractional statistical uncertainties of 60% working point scale factor are shown in Table 6.7 for the standard and the combined selection. In some bins the statistical uncertainty can decrease up to 30%, suggesting that the high- p_T selection is successful at increasing events statistics.

	PFlow jets			VR-Track jets		
	Standard selection	High- p_T selection	Fractional decrease	Standard selection	High- p_T selection	Fractional decrease
Bin No.1	3.3%	3.3%	0.0%	5.6%	5.3%	5.7%
Bin No.2	3.1%	2.8%	10.7%	4.2%	3.7%	13.5%
Bin No.3	3.4%	2.6%	30.8%	5.8%	4.9%	18.4%
Bin No.4	12.1%	9.3%	30.1%	7.2%	5.6%	28.6%

Table 6.7: Comparison of the fractional statistical uncertainty in the DL1r 60% working point scale factor. The p_T range of each bin can be found in section 6.2.

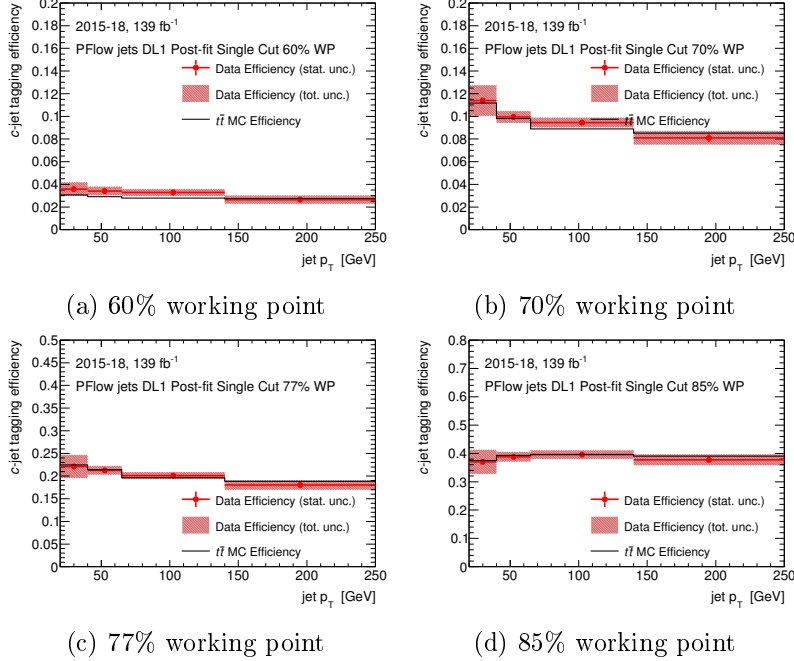


Figure 6.11: Charm-jet efficiencies for the PFlow jets collection with the DL1 tagger.

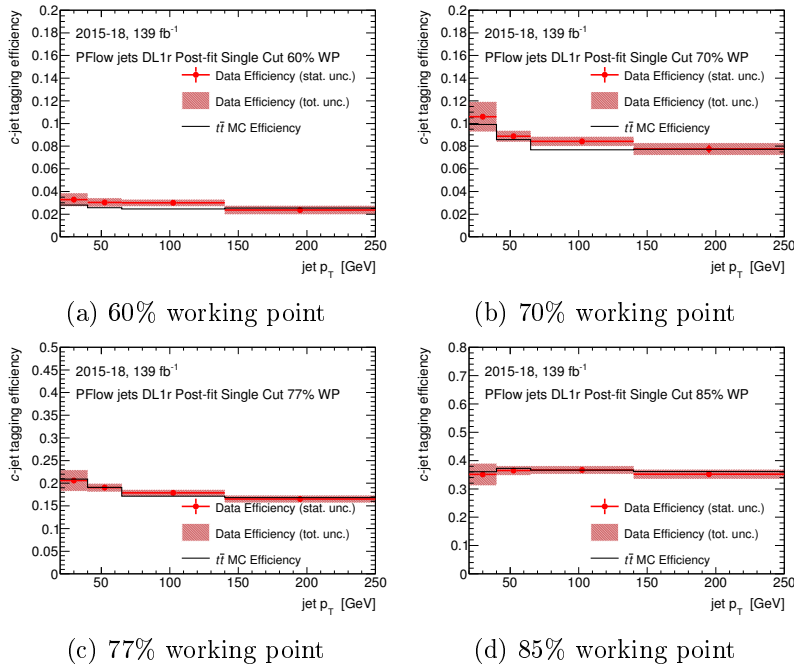


Figure 6.12: Charm-jet efficiencies for the PFlow jets collection with the DL1r tagger.

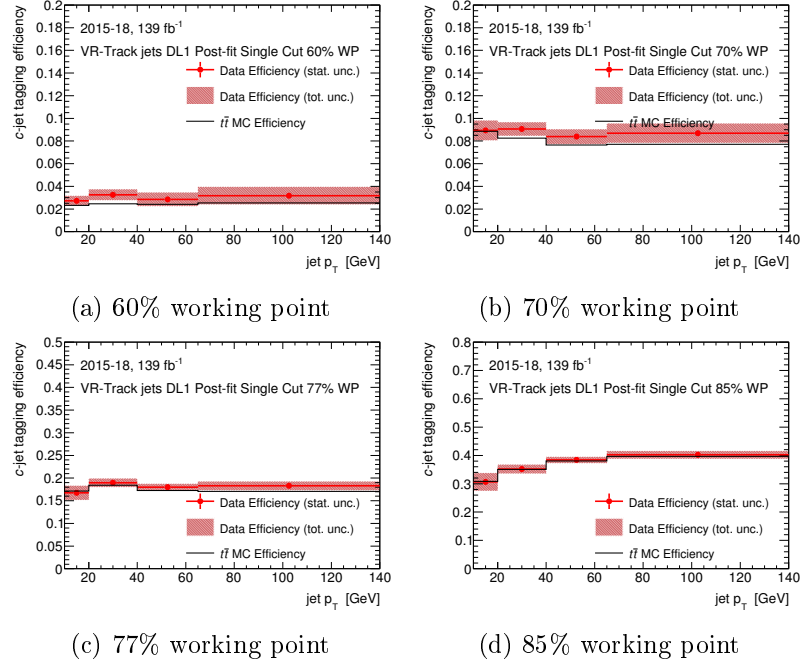


Figure 6.13: Charm-jet efficiencies for the VR-Track jets collection with the DL1 tagger.

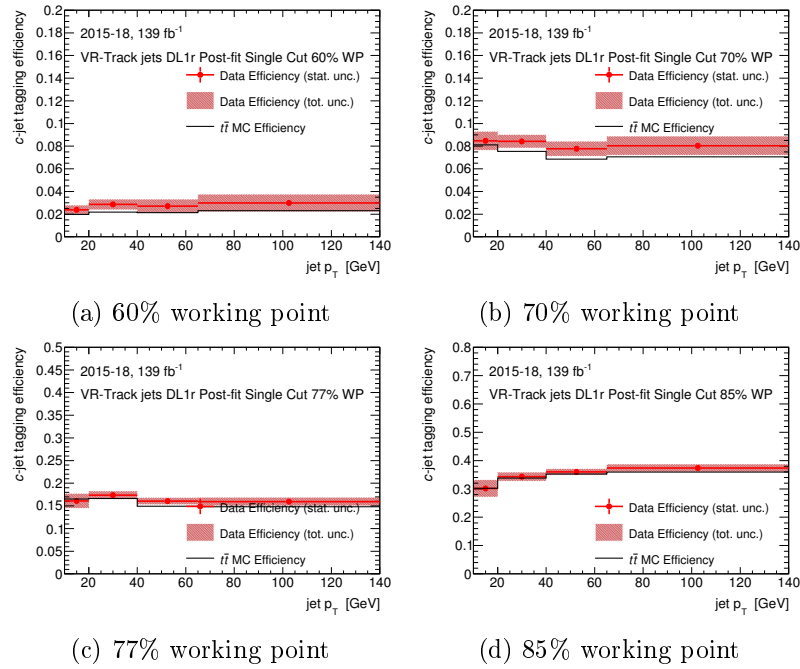


Figure 6.14: Charm-jet efficiencies for the VR-Track jets collection with the DL1r tagger.

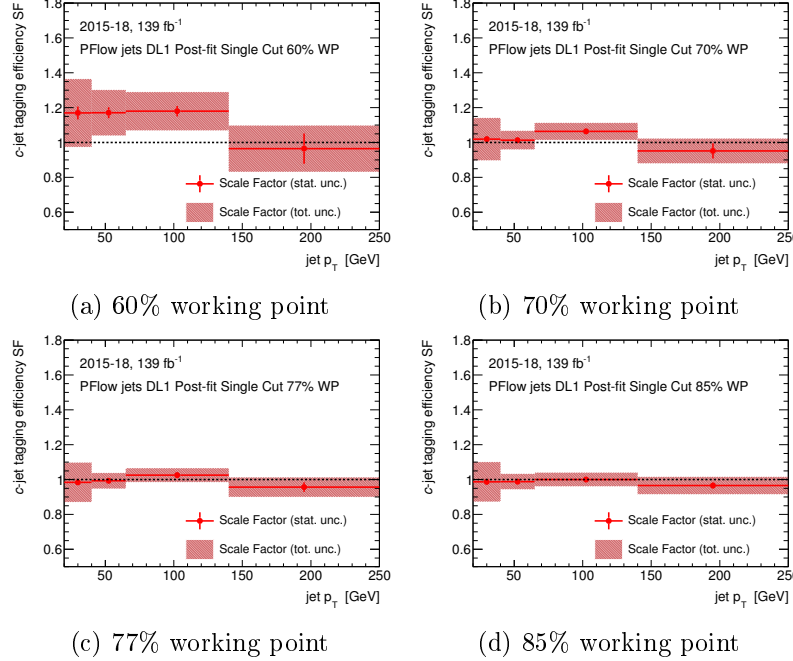


Figure 6.15: Charm-jet scale factors for the PFlow jets collection with the DL1 tagger.

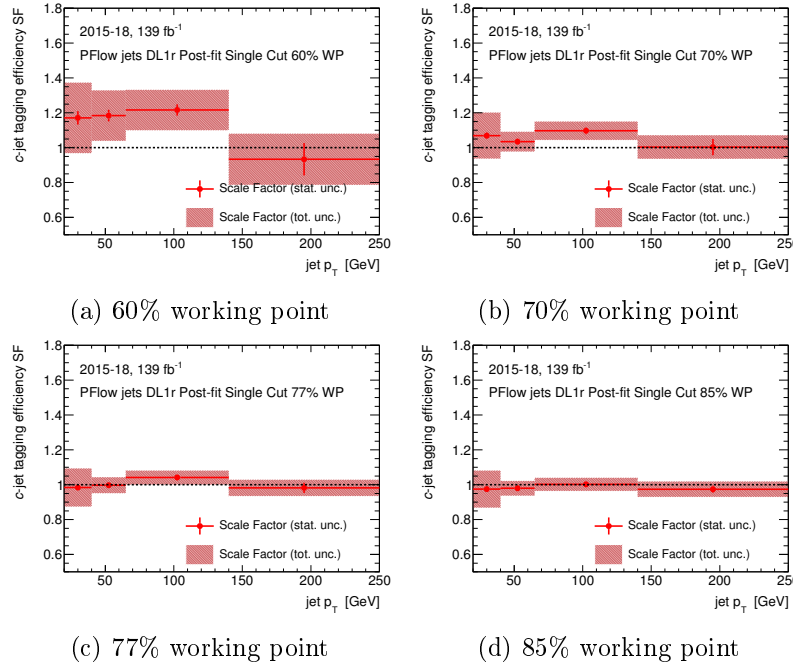


Figure 6.16: Charm-jet scale factors for the PFlow jets collection with the DL1r tagger.

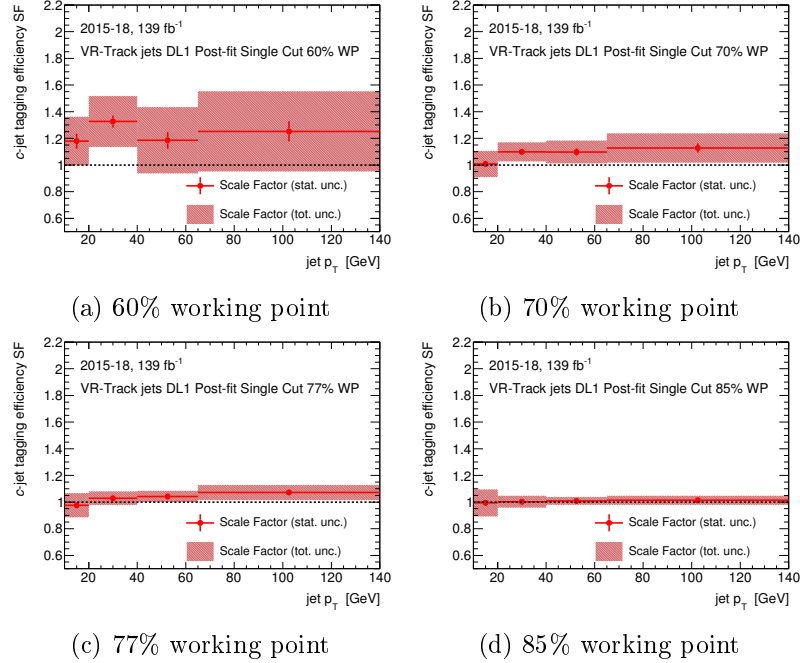


Figure 6.17: Charm-jet scale factors for the VR-Track jets collection with the DL1 tagger.

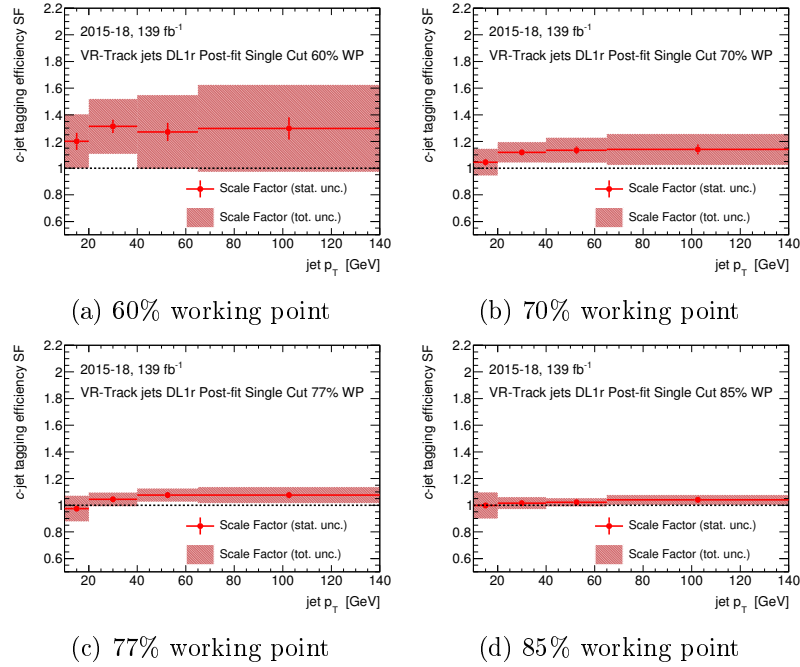


Figure 6.18: Charm-jet scale factors for the VR-Track jets collection with the DL1r tagger.

Chapter 7

Search for Higgs boson pair production in the $b\bar{b}\tau_{lep}^+\tau_{had}^-$ channel

due: 15/12 This chapter describes the search for Higgs boson pair production in the $b\bar{b}\tau_{lep}^+\tau_{had}^-$ channel, where one Higgs boson decays to a b quark pair and the other to a τ -lepton pair, where one τ -lepton decays leptonically and the other τ -lepton decay hadronically. This analysis is the main focus of this thesis work and it is part of the ATLAS Run 2 di-Higgs to $b\bar{b}\tau^+\tau^-$ search, published in Reference TODO: add in the publishing dihiggs paper. The ATLAS $b\bar{b}\tau^+\tau^-$ analysis is performed in two channels depending on the τ -leptons decay modes, the $b\bar{b}\tau_{lep}^+\tau_{had}^-$ channel which is described in this thesis, and the $b\bar{b}\tau_{had}^+\tau_{had}^-$ channel where both τ -leptons decay hadronically. The combination of the two sub-channels is also performed in this thesis work and is presented in this chapter. The results of this search are interpreted in terms of an upper limit on the SM di-Higgs production cross section and limits on the triple Higgs self-coupling $k_\lambda = \lambda_{HHH}/\lambda_{SM}$ for the non-resonant search. The non-resonant search is also interpreted in terms of the coupling modifiers using an effective field theory approach. Moreover, the data are also analysed to search for resonances decaying to a pair of Higgs bosons and interpreted in terms of upper limits on the resonance production cross section as a function of the resonance mass, constraining a model with an extended Higgs sector based on two doublets (2HDM) model. The non-resonant and resonant search in the $b\bar{b}\tau_{lep}^+\tau_{had}^-$ channel is part of the ATLAS $b\bar{b}\tau^+\tau^-$ analysis, as combined with the $b\bar{b}\tau_{had}^+\tau_{had}^-$ where both τ -leptons decay hadronically. The combine results are published in References TODO: cite the paper. The k_λ result is combined with other final states of the di-Higgs production including $b\bar{b}b\bar{b}$ and $b\bar{b}\gamma\gamma$ where the di-Higgs decay to two pairs of b quarks and a pair of b quarks with a pair of photons. The result is published in Reference TODO: cite the combination paper.

In the following sections all the aspects of the analysis are discussed. The simulated signal and background samples are listed in Section 6.1. The object and event selections are discussed in Section 6.2 and 6.3 respectively. The background estimation is explained in Section 6.4. The multivariate analysis is described in Section 6.5. The list of systematic uncertainties is given in Section 6.6. The statistical interpretation is described in Section 6.7 and the results are presented and discussed in Section 6.8.

7.1 Data and Monte Carlo Simulation

7.1.1 Data samples

The data used in this search were collected at a centre-of-mass energy of 13 TeV between 2015 and 2018, using triggers to select events with at least one electron or one muon and at least one $\tau_{\text{had-vis}}$. Details about these triggers are discussed in Section 7.2.1. Events are selected for analysis only if they are of good quality and if all the relevant detector components are known to be in good operating conditions [103]. The total integrated luminosity of the data, after meeting the good quality criteria, is $139.0 \pm 2.4 \text{ fb}^{-1}$ [70, 104]. The recorded events contain an average of 34 simultaneous inelastic pp collisions per bunch-crossing.

7.1.2 Simulated event samples

Monte Carlo (MC) simulated events are used to model the SM background production, the SM-like non-resonant HH signal production, and the BSM resonant HH signal production. They are passed through the full ATLAS detector simulation [74] based on GEANT 4 [75], except for the BSM resonant HH signal samples that are passed through a fast simulation, for which the response of the calorimeters is parameterised rather than fully simulated. The effects of pileup are modelled by overlaying minimum bias events, simulated using the soft quantum chromodynamics (QCD) processes of PYTHIA 8.186 [105] with the A3 [78] set of tuned parameters and NNPDF2.3LO [77] parton distribution functions (PDFs). The EVTGEN v1.6.0 program [101] is used to describe the decays of bottom and charm hadrons for all samples of simulated events, except for those generated using SHERPA [88] and the VBF non-resonant HH sample. The resulting events were then processed through the same reconstruction programs as the data. For all samples containing a SM Higgs boson, its mass was fixed to 125 GeV. The same mass value is used for the calculation of the Higgs boson decay branching ratios and for the calculation of the single Higgs boson and SM non-resonant HH production cross-sections. Unless spec-

Process	ME generator	ME QCD	ME PDF hadronisation	PS and tune	UE model order	Cross-section
Signal						
non-resonant $gg \rightarrow HH$ (ggF)	POWHEG-BOX v2	NLO	PDF4LHC15 NLO	PYTHIA 8.244	A14	NNLO FTApprox
non-resonant $qq \rightarrow qqHH$ (VBF)	MADGRAPH5_aMC@NLO v2.7.3	LO	NNPDF3.0NLO	PYTHIA 8.244	A14	N3LO(QCD)
resonant $gg \rightarrow X \rightarrow HH$	MADGRAPH5_aMC@NLO v2.6.1	LO	NNPDF2.3LO	HERWIG v7.1.3	H7.1-Default	-
Top-quark						
$t\bar{t}$	POWHEG-BOX v2	NLO	NNPDF3.0NLO	PYTHIA 8.230	A14	NNLO+NNLL
t -channel	POWHEG-BOX v2	NLO	NNPDF3.0NLO	PYTHIA 8.230	A14	NLO
s -channel	POWHEG-BOX v2	NLO	NNPDF3.0NLO	PYTHIA 8.230	A14	NLO
Wt	POWHEG-BOX v2	NLO	NNPDF3.0NLO	PYTHIA 8.230	A14	NLO
$t\bar{t}Z$	SHERPA 2.2.1	NLO	NNPDF3.0NLO	SHERPA 2.2.1	Default	NLO ^(†)
$t\bar{t}W$	SHERPA 2.2.8	NLO	NNPDF3.0NNLO	SHERPA 2.2.8	Default	NLO ^(†)
Vector boson + jets						
$W/Z+jets$	SHERPA 2.2.1	NLO (≤ 2 jets) LO (3,4 jets)	NNPDF3.0NNLO	SHERPA 2.2.1	Default	NNLO
Diboson						
WW, WZ, ZZ	SHERPA 2.2.1	NLO (≤ 1 jet) LO (2,3 jets)	NNPDF3.0NNLO	SHERPA 2.2.1	Default	NLO ^(†)
Single Higgs boson						
ggF	POWHEG-BOX v2	NNLO	NNPDF3.0NLO	PYTHIA 8.212	AZNLO	N3LO(QCD)+NLO(EW)
VBF	POWHEG-BOX v2	NLO	NNPDF3.0NLO	PYTHIA 8.212	AZNLO	NNLO(QCD)+NLO(EW)
$qq \rightarrow WH$	POWHEG-BOX v2	NLO	NNPDF3.0NLO	PYTHIA 8.212	AZNLO	NNLO(QCD)+NLO(EW)
$qq \rightarrow ZH$	POWHEG-BOX v2	NLO	NNPDF3.0NLO	PYTHIA 8.212	AZNLO	NNLO(QCD)+NLO(EW) ^(†)
$gg \rightarrow ZH$	POWHEG-BOX v2	NLO	NNPDF3.0NLO	PYTHIA 8.212	AZNLO	NLO+NLL
$t\bar{t}H$	POWHEG-BOX v2	NLO	NNPDF3.0NLO	PYTHIA 8.230	A14	NLO

Table 7.1: The generators used for the simulation of the signal and background processes. If not specified, the order of the cross-section calculation refers to the expansion in the strong coupling constant (α_S). The acronyms ME, PS and UE are used for matrix element, parton shower and underlying event, respectively.

ified, the order of the cross-section calculation refers to the expansion in the strong coupling constant (α_s). A summary of the event samples used for the simulation of the signal and background processes is shown in Table 7.1.

7.1.2.1 Simulated signal samples

Simulated SM non-resonant HH signal production includes the contributions from the ggF and VBF processes. The simulated ggF events were generated with the POWHEG-Box v2 generator [82] at next-to-leading order (NLO) with finite top-quark mass, and using the PDF4LHC15 NLO PDF set [106]. Parton showers and hadronisation were simulated using PYTHIA 8.244 [105] with the A14 set of tuned parameters [100, 107] and the NNPDF2.3LO PDF set. The cross-section of the ggF non-resonant HH production calculated at next-to-next-to-leading order (NNLO) FTApprox [108] (taking account of the finite top-quark mass) is $31.1^{+2.2\%}_{-5.0\%}(\text{scale}) \pm 2.1\%(\alpha_S) \pm 2.1\%(\text{PDF}) \pm 2.6\%(m_{top})$ fb at $\sqrt{s} = 13$ TeV and $m_H = 125$ GeV.

The VBF non-resonant HH signal production was generated at LO using the MADGRAPH5_aMC@NLO v2.7.3 [99] generator with the NNPDF3.0NLO [85] PDF set. Parton showering and hadronisation were performed using PYTHIA 8.244 with the A14 set of tuned parameters and the NNPDF2.3LO PDF set. The EVTGEN v1.7.0 program was used for describing the bottom- and charm-hadron decays. The

cross-section of the VBF non-resonant HH production calculated at next-to-next-to-next-to-leading order (N3LO) in QCD in the limit in which there is no partonic exchange between the two protons [109] is $1.73^{+0.03\%}_{-0.04\%}(\text{scale}) \pm 2.1\%(\text{PDF} + \alpha_S)$ fb. Other non-resonant HH production modes are not considered as their contributions to the analysis sensitivity are expected to be negligible.

The BSM resonant HH signal from the ggF production of a heavy spin-0 resonance and its decay into a pair of SM Higgs bosons, $X \rightarrow HH$, was simulated with the MADGRAPH5_aMC@NLO v2.6.1 generator using the NNPDF2.3LO PDF set at LO accuracy in QCD. The simulated events were interfaced to HERWIG 7.1.3 [110, 111] to model the parton shower, hadronisation and underlying event, using the H7.1-Default tune [112] and the NNPDF2.3LO PDF set. The resonant HH signal was simulated for 19 values of the resonance mass, m_X , between 251 GeV and 1.6 TeV. A dummy cross section of 1 pb is chosen for these samples to make combination with other decay channels easier, and to ease scaling of the signal for the calculation of the cross section limits (more details in Section ??).

7.1.2.1.1 Non-resonant signal reweighting and combination

The non-resonant signal is sensitive to the parameter κ_λ as described in section ?? (TODO: ref back to theory section about klambda dependence). For the ggF non-resonant HH production, MC samples are generated at $\kappa_\lambda = 1$ and 10, while for VBF production, MC samples are generated at $\kappa_\lambda = 0, 1, 2$ and 10. A sample combination technique is used to model the signal hypothesis at different κ_λ values. For the ggF di-Higgs production, a reweighting method described in [113] is used to obtain predictions at different κ_λ values in the range $\kappa_\lambda \in [-30, 30]$ in increments of 0.2 based on a linear combination of samples at $\kappa_\lambda = 0, 1$ and 20. The remaining $\kappa_\lambda = 10$ sample is used to validate the method. For each κ_λ value, a set of weights $w(m_{HH}, \kappa_\lambda)$ is evaluated by dividing the binned m_{HH} distribution of the κ_λ target sample over the SM distribution. Therefore, weights for any κ_λ sample can be obtained and they can be used to reweight the SM sample to any κ_λ value. Then a reweighted distribution at analysis level results from applying the weights to the SM sample after reconstruction and the selection steps. Given the assumption that the kinematic of the ggF events and their acceptance depend only on m_{HH} variable, using the weights $w(m_{HH}, \kappa_\lambda)$ the reweighted sample describes correctly any kinematic distribution of a given target κ_λ value. Good closure is found between the distributions obtained from κ_λ generated and reweighted, as shown in section ??.

For the VBF di-Higgs production, the above reweighting procedure is not valid, because the kinematic of the events can not be defined just using a single variable

such as m_{HH} . Therefore three MC samples with $\kappa_\lambda = 1, 2, 10$ are used, the events distributions and the multivariate algorithm output (more details in section 7.2.3) for any κ_λ value are obtained from the linear combination of the events distribution and the multivariate output of the three samples at analysis level. The linear coefficients for combining the three samples defined are defined by the formula (which is also valid to evaluate the VBF cross-section as a function of κ_λ where all the other couplings are set to SM value):

$$\begin{aligned} \sigma(\kappa_\lambda) = & \left(\frac{\kappa_\lambda^2}{9} - \frac{4\kappa_\lambda}{3} + \frac{20}{9} \right) \times \sigma(1) + \left(-\frac{\kappa_\lambda^2}{8} + \frac{11\kappa_\lambda}{8} - \frac{5}{4} \right) \times \sigma(2) \\ & + \left(\frac{\kappa_\lambda^2}{72} - \frac{\kappa_\lambda}{24} + \frac{1}{36} \right) \times \sigma(10) \end{aligned} \quad (7.1)$$

7.1.2.2 Simulated background samples

The $t\bar{t}$ production and the single top-quark events in the Wt -, s - and t -channels were generated using the POWHEG-BOX v2 generator together with the NNPDF3.0NLO PDF set. The simulated events were interfaced to PYTHIA 8.230 for parton shower and hadronisation using the A14 set of tuned parameters together with the NNPDF2.3LO PDF set. For all these simulated top-quark processes, the top-quark spin correlations are preserved. The top-quark mass was set to 172.5 GeV. The $t\bar{t}$ production cross-section is calculated at next-to-next-to-leading order and next-to-next-to-leading-logarithm (NNLO+NNLL) [114]. The cross-sections of the single top-quark processes are calculated at NLO [115–117]. The $t\bar{t}$ - Wt interference is handled using the diagram removal scheme.

Events containing W or Z bosons produced in association with jets, diboson (WW , WZ and ZZ) production processes, and $t\bar{t}Z$ ($t\bar{t}W$) processes were simulated with the SHERPA 2.2.1 (2.2.8) generator [88] using the NNPDF3.0NNLO [85] PDF set with dedicated parton shower tuning developed by the SHERPA authors. For simulating the $W/Z+jets$ events the matrix elements were calculated for up to two partons at NLO and four partons at LO using the OPENLOOP [91] and COMIX [89] matrix-element generators. The number of expected $W/Z+jets$ events is normalised to the NNLO cross-sections [118]. The diboson production was simulated up to one additional parton at NLO and up to three additional partons at LO using the OPENLOOP and COMIX programs. The cross-sections from SHERPA at NLO are used to normalise the diboson and the $t\bar{t}W/Z$ events.

The SM single Higgs boson production is considered as part of the background in this search, and its production modes were simulated using the POWHEG-Box v2 generator and the NNPDF3.0NLO PDF set. The single Higgs boson production via ggF was simulated at NNLO accuracy in QCD using the Powheg NNLOPS program [119, 120], whereas the VBF single Higgs boson production was simulated at NLO accuracy in QCD [121]. Both productions were interfaced to PYTHIA 8.212 for parton shower and hadronisation using the AZNLO tune [122] together with the CTEQ6L1 PDF set [123]. The cross-section of ggF production of single Higgs boson is based on a computation with N3LO accuracy in QCD, and NLO in the electroweak (EW) expansion [124–128], whereas the VBF single Higgs boson production cross-section is set to the NNLO(QCD)+NLO(EW) calculation [124, 129–131]. The $qq \rightarrow WH$, $qq \rightarrow ZH$ and $gg \rightarrow ZH$ simulated events were interfaced to PYTHIA 8.212 for parton shower and hadronisation using the AZNLO tune together with the CTEQ6L1 PDF set. The cross-sections are set to the NNLO(QCD)+NLO(EW) calculations for $qq \rightarrow WH$ and $qq \rightarrow ZH$ [132–138], and to the next-to-leading order and next-to-leading-logarithm (NLO+NLL) in QCD for $gg \rightarrow ZH$ [139–143]. For the Higgs boson production in association with a pair of top-quarks ($t\bar{t}H$), the simulated events were interfaced to PYTHIA 8.230 for parton shower and hadronisation using the A14 set of tuned parameters, and NNPDF2.3LO PDF set. The cross-section of $t\bar{t}H$ production is set to NLO calculations [124]. The SM single Higgs boson production plays a more important role as a background to the non-resonant HH search than the resonant HH search due to more similar kinematics between the SM single Higgs boson production and the non-resonant HH production.

7.2 Event Selection

7.2.1 Trigger selection

Events in the $\tau_{\text{lep}}\tau_{\text{had}}$ categories are recorded using a combination of single-lepton triggers (SLTs) and lepton-plus- $\tau_{\text{had-vis}}$ triggers (LTs). The SLTs require an electron or muon to be reconstructed at the HLT with a minimum E_T threshold that ranges from 24 GeV to 26 GeV for electrons and a minimum p_T threshold that ranges from 20 GeV to 26 GeV for muons, depending on the data-taking period. The LTs require that an electron with $E_T > 17$ GeV or a muon with $p_T > 14$ GeV in addition to a $\tau_{\text{had-vis}}$ with $p_T > 25$ GeV are reconstructed at the HLT. From the 2017 data-taking period onward, for the LTs that rely on an electron at the HLT or a $\tau_{\text{had-vis}}$ with a p_T threshold below 35 GeV, either an additional jet with $E_T > 25$ GeV or two

additional jets with $E_T > 12$ GeV are required at the Level-1 trigger to reduce the trigger rates. To ensure that the trigger reaches its efficiency plateau, the offline electrons, muons and $\tau_{\text{had-vis}}$ objects are required to be within $\Delta R < 0.07$, $\Delta R < 0.1$ and $\Delta R < 0.2$ of the corresponding objects at the HLT, respectively. Minimum p_T thresholds are applied to the offline objects, which are 1 GeV above the thresholds for electrons and muons at the HLT, 5 GeV above the thresholds for $\tau_{\text{had-vis}}$ at the HLT, and 80 GeV (45 GeV) for jets with Level-1 trigger E_T -thresholds of 25 GeV (12 GeV). Events which pass the offline SLT lepton p_T requirements are not considered for the LTT to ensure no overlap with the SLT category. These two categories are analysed separately.

7.2.2 Event preselection

Before passing the events to the MVA algorithm, they are required to pass a loose preselection criteria, given in the following. Events are required to contain exactly exactly one electron or muon, an oppositely charged $\tau_{\text{had-vis}}$, and exactly two b -tagged jets. The selected electron (muon) must pass a tight (medium) identification requirement with an efficiency of around 80% (97%).

The invariant mass of the τ -lepton pair ($m_{\tau\tau}^{\text{MMC}}$) is estimated from the four-momenta of the electron or muon, the $\tau_{\text{had-vis}}$ and the $\mathbf{p}_T^{\text{miss}}$ using the Missing Mass Calculator (MMC) [144], which assumes that the $\mathbf{p}_T^{\text{miss}}$ is exclusively from the neutrinos produced in the τ -lepton decays. To reject background events from low-mass Drell-Yan events, $m_{\tau\tau}^{\text{MMC}}$ is required to be above 60 GeV. The b -tagged jet pair invariant mass (m_{bb}) is required to be less than 150 GeV to reject $t\bar{t}$ background events, and to allow for the definition of a $t\bar{t}$ -enriched region which is used in the estimation of $t\bar{t}$ backgrounds, as described in Section ???. A $\tau_{\text{had-vis}}$ with $p_T > 20$ GeV and $|\eta| < 2.3$ is required in the SLT category, and a $\tau_{\text{had-vis}}$ with $p_T > 30$ GeV, or higher if required by the trigger, and $|\eta| < 2.3$ is required in the LTT category. In both categories, the (sub-)leading b -tagged jet must have $p_T > 45$ (20) GeV, in addition to any trigger-dependent requirements. The full event selection is summarised in Table 7.2.

The rate of events accepted by the detector and selected by the analysis selection are quantified by the acceptance and the selection efficiency, respectively. The acceptance times efficiency for the non-resonant ggF+VBF $HH \rightarrow b\bar{b}\tau^+\tau^-$ signal is evaluated with respect to the targeted τ -lepton decay modes to be 4.0% (1.0%) in the $\tau_{\text{lep}}\tau_{\text{had}}$ SLT (LTT) categories. For the resonant HH signal, the acceptance times efficiency is shown in Figure 7.1 as a function of the resonance mass. The decrease in acceptance times efficiency for m_X greater than about 1000 GeV is due to the

Lorentz boost of the Higgs bosons causing their decay products to become highly collimated more often.

$\tau_{\text{lep}}\tau_{\text{had}}$ categories	
SLT	LTT
e/μ selection	
Exactly one tight e or medium μ	
$p_T^e > 25, 27 \text{ GeV}$	$18 \text{ GeV} < p_T^e < \text{SLT cut}$
$p_T^\mu > 21, 27 \text{ GeV}$	$15 \text{ GeV} < p_T^\mu < \text{SLT cut}$
$ \eta^e < 2.47, \text{ not } 1.37 < \eta^e < 1.52$	
$ \eta^\mu < 2.7$	
$\tau_{\text{had-vis}}$ selection	
One loose $\tau_{\text{had-vis}}$	
$ \eta < 2.3$	
$p_T > 20 \text{ GeV}$	$p_T > 30 \text{ GeV}$
Jet selection	
≥ 2 jets with $ \eta < 2.5$	
$p_T > 45$ (20) GeV	Trigger dependent
Event-level selection	
Trigger requirements passed	
Collision vertex reconstructed	
$m_{\tau\tau}^{\text{MMC}} > 60 \text{ GeV}$	
Opposite-sign electric charges of $e/\mu/\tau_{\text{had-vis}}$ and $\tau_{\text{had-vis}}$	
Exactly two b -tagged jets	
$m_{bb} < 150 \text{ GeV}$	

Table 7.2: Summary of the event selections, shown separately for the SLT and LTT. In cases where pairs of reconstructed objects of the same type are required, thresholds on the (sub-)leading p_T object are given outside (within) parentheses. When the selection depends on the year of data-taking, the possible values of the requirements are separated by commas, except for the jet selection in the LTT channel which use multiple selection criteria as described in Section 7.2.1. The trigger p_T thresholds shown correspond to the offline requirements.

7.2.3 Multivariate signal extraction

The di-Higgs non-resonant SM signal is well-defined in its kinematic properties, and so a neural network trained on this signal is used in the $\tau_{\text{lep}}\tau_{\text{had}}$ channel. The di-Higgs resonant signal, however, is not a single signal hypothesis, but rather a set of continuous signal hypotheses parameterised by the mass of the heavy resonance which decays to Higgs boson pairs. For these cases, a standard binary classification algorithm is not optimal. A set of single discriminants trained on each of the simulated signal hypotheses would provide good discrimination for the simulated hypotheses, but can not interpolate well between these points. For this reason, and to reduce the number of algorithms that require training, Parametric Neural Networks (PNNs) [145] are used for the extraction of the resonant signal. PNNs are

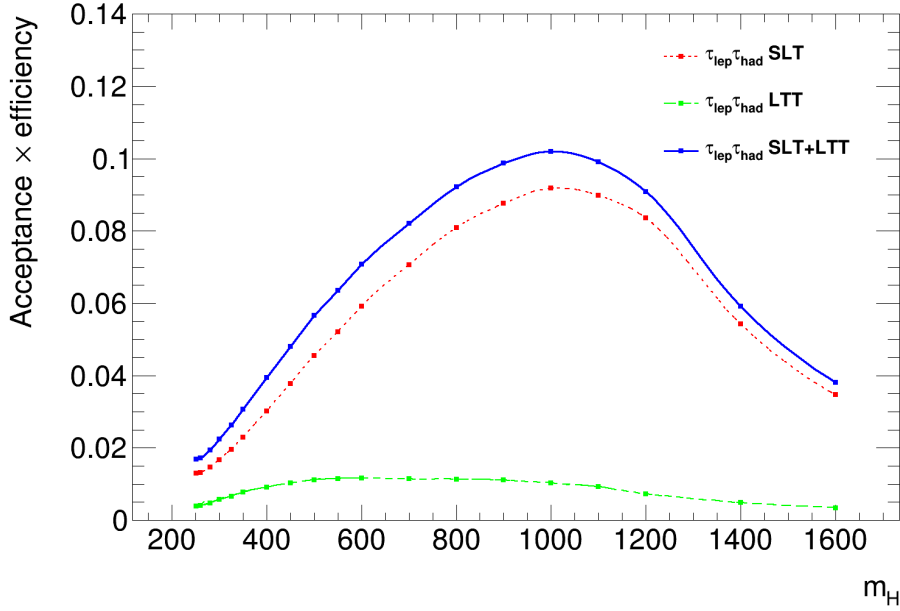


Figure 7.1: Acceptance times efficiency for the $\tau_{\text{lep}}\tau_{\text{had}}$ selection as a function of the resonance mass m_X in SLT, LTT and SLT LTT combined. The acceptance times efficiency is evaluated for $X \rightarrow HH \rightarrow b\bar{b}\tau^+\tau^-$ decays, with respect to the targeted $\tau_{\text{lep}}\tau_{\text{had}}$ decay mode.

neural networks which enable optimal signal-to-background classification for signal spectra connected by one or more physics parameters. As this problem is a smoothly-varying learning task, the PNN is not just able to learn how to classify signals at the simulated signal mass training points, but also how to interpolate between them. Figure 7.2 shows the PNN response in terms of Asimov significance as a function of the PNN mass parameter obtained for signal samples with different masses. This is showing the mass resolution of the PNN.

The (P)NNs are trained using Keras [146] with the Tensorflow [147] backend. The PNNs used in the analyses described in this note take as an input parameter to specify which signal should be targeted, along side the feature variables, the heavy resonance mass for the di-Higgs analysis. During training, the PNNs are trained on all the signals simultaneously, and are provided with the generator-level masses of the signals and a random mass from the distribution of simulated signal masses for the background. The background events are provided with such distribution of simulated signal masses because the background events do not have a well-defined value for the “truth scalar resonance mass” and the ‘parameter’ assigned to background events must be uninformative regarding the signal / background discrimination. This is achieved by randomly assigning a “truth scalar resonance mass” that follows the distribution seen in the signal training events. During implementation, the mass of

the targeted signal is given, which results in optimal discrimination for that signal hypothesis. As the ideal neural network output (when trained on the binary cross entropy) is a monotonic function of the signal-to-background density ratio, this means that the PNN will optimally classify the targeted signal events, as specified by the physics input parameter.

The same choice of MVA input variables is used for the resonant and non-resonant production modes, though different input variables are used in the different analysis categories. These variables are listed in Table 7.3, and are defined as follows:

- m_{HH} is the invariant mass of the HH system as reconstructed from the τ -lepton pair (calculated using the MMC) and the b -tagged jet pair;
- $\Delta R(\tau, \tau)$ is evaluated between the two $\tau_{\text{had-vis}}$ (the electron or muon and the $\tau_{\text{had-vis}}$) in the $\tau_{\text{had}}\tau_{\text{had}}$ category ($\tau_{\text{lep}}\tau_{\text{had}}$ categories);
- $\Delta R(b, b)$ is evaluated between the b -tagged jets;
- $\Delta p_T(\ell, \tau)$ is the difference between the transverse momenta of the lepton and the $\tau_{\text{had-vis}}$;
- $m_T^W = \sqrt{2p_T^\ell E_T^{\text{miss}}(1 - \cos \Delta\phi_{\ell, \mathbf{p}_T^{\text{miss}}})}$ is the transverse mass of the lepton and the $\mathbf{p}_T^{\text{miss}}$;
- the $\mathbf{p}_T^{\text{miss}} \phi$ centrality specifies the angular position of the $\mathbf{p}_T^{\text{miss}}$ relative to the $\tau_{\text{had-vis}}$ in the transverse plane [148] and is defined as $(A+B)/\sqrt{A^2 + B^2}$, where $A = \sin(\phi_{\mathbf{p}_T^{\text{miss}}} - \phi_{\tau_2})/\sin(\phi_{\tau_1} - \phi_{\tau_2})$, $B = \sin(\phi_{\tau_1} - \phi_{\mathbf{p}_T^{\text{miss}}})/\sin(\phi_{\tau_1} - \phi_{\tau_2})$, and τ_1 and τ_2 represent the two $\tau_{\text{had-vis}}$ (electron or muon and $\tau_{\text{had-vis}}$) in the case of the $\tau_{\text{had}}\tau_{\text{had}}$ category ($\tau_{\text{lep}}\tau_{\text{had}}$ categories);
- $\Delta\phi(\ell\tau, bb)$ is the azimuthal angle between the $\ell+\tau_{\text{had-vis}}$ system and the b -tagged jet pair;
- $\Delta\phi(\ell, \mathbf{p}_T^{\text{miss}})$ is the azimuthal angle between the lepton and the $\mathbf{p}_T^{\text{miss}}$;
- $\Delta\phi(\ell\tau, \mathbf{p}_T^{\text{miss}})$ is the azimuthal angle between the electron or muon and $\tau_{\text{had-vis}}$ system and the $\mathbf{p}_T^{\text{miss}}$;
- S_T is the total transverse energy in the event, summed over all jets, $\tau_{\text{had-vis}}$ and leptons in the event and E_T^{miss} .

The m_{HH} , $m_{\tau\tau}^{\text{MMC}}$ and m_{bb} distributions are shown in Figure ???. For all categories of the non-resonant search, $m_{\tau\tau}^{\text{MMC}}$ and m_{bb} are among the three most important MVA input variables. For the resonant search, five values of m_X were tested in all

categories, and m_{HH} was found to be the most important MVA input variable in all cases except for at lower values of m_X in the $\tau_{\text{had}}\tau_{\text{had}}$ category.

Table 7.3: Variables used as inputs to the MVAs in the three analysis categories. The same choice of input variables is used for the resonant and non-resonant production modes. The variables are defined in the main text.

Variable	$\tau_{\text{had}}\tau_{\text{had}}$	$\tau_{\text{lep}}\tau_{\text{had}}$	SLT	$\tau_{\text{lep}}\tau_{\text{had}}$	LTT
m_{HH}	✓		✓		✓
$m_{\tau\tau}^{\text{MMC}}$	✓		✓		✓
m_{bb}	✓		✓		✓
$\Delta R(\tau, \tau)$	✓		✓		✓
$\Delta R(b, b)$	✓		✓		
$\Delta p_T(\ell, \tau)$			✓		✓
Sub-leading b -tagged jet p_T			✓		
m_T^W			✓		
E_T^{miss}			✓		
$\mathbf{p}_T^{\text{miss}}$ ϕ centrality			✓		
$\Delta\phi(\ell\tau, bb)$			✓		
$\Delta\phi(\ell, \mathbf{p}_T^{\text{miss}})$				✓	
$\Delta\phi(\ell\tau, \mathbf{p}_T^{\text{miss}})$				✓	
S_T				✓	

The (P)NNs use rectified linear unit and sigmoidal activation functions for the hidden and output layers, respectively, binary cross entropy as the loss function, and stochastic (mini-batch) gradient descent as the optimiser [149]. For the (P)NN used in the $\tau_{\text{lep}}\tau_{\text{had}}$ SLT category, 2 layers of 512 hidden nodes are used, and for the (P)NN used in the $\tau_{\text{lep}}\tau_{\text{had}}$ LTT category 3 layers of 512 (256) nodes are used. The (P)NN input variables are standardised by subtracting the median value and dividing by the interquartile range. Nesterov momentum and learning rate decay were used in the training of all (P)NNs, and in the $\tau_{\text{lep}}\tau_{\text{had}}$ categories they used an L2 regularisation term in the loss function [149].

7.2.4 $Z + \text{HF}$ control region

The normalisation of the $Z + \text{HF}$ background is determined from data by fitting the $m_{\ell\ell}$ distribution in the a dedicated control region ($Z + \text{HF CR}$) in the likelihood fit. This is to account for a known discrepancy in the $Z + \text{HF}$ production cross-section at NLO with respect to data, as provided for these processes in SHERPA. The $Z + \text{HF CR}$ targets events containing Z boson decays to electron or muon pairs using triggers that require single leptons, or pairs of same-flavour leptons. Exactly two oppositely-charged same-flavour leptons and exactly two b -tagged jets are required to be reconstructed offline. The leptons are required to have $p_T > 9 \text{ GeV}$, pass offline

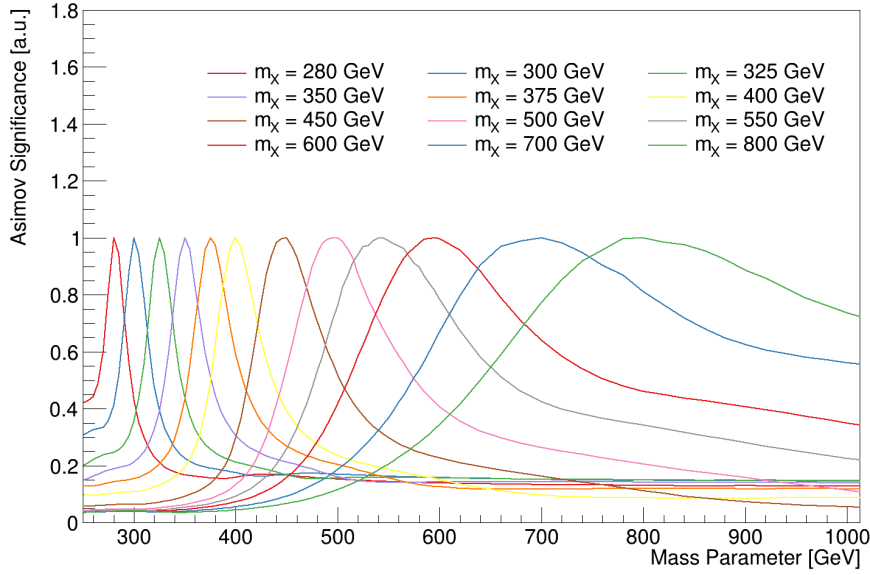


Figure 7.2: PNN response in terms of Asimov significance as a function of the PNN mass parameter obtained for signal samples with different masses for the di-Higgs $\tau_{\text{lep}}\tau_{\text{had}}$ channel. Due to a large difference in acceptance times efficiency of the $\tau_{\text{lep}}\tau_{\text{had}}$ channel signal region selection depending on the mass of the resonance, all significances are scaled so that the maximum significance is 1 for better visibility.

p_T thresholds based on the trigger thresholds, be compatible with originating from the primary vertex, and pass medium identification and loose isolation requirements. Lastly, the invariant mass of the lepton pair is required to be between 75 GeV and 110 GeV to select events originating from a Z boson decay, and m_{bb} is required to be less than 40 GeV or greater than 210 GeV to ensure orthogonality to other analyses containing Higgs boson decays. This region also provides constraints on the normalisation of the $t\bar{t}$ background.

due: 05/11

7.3 Background estimation

This section describes the background estimation methods used in the HH analysis.

The simulated event samples summarised in Section ?? are used to model all background processes, except for processes with fake- τ_{had} which are estimated using data-driven techniques, as discussed below. In the $\tau_{\text{lep}}\tau_{\text{had}}$ channel, all fake- τ_{had} backgrounds from $t\bar{t}$ and multi-jet processes are estimated using an inclusive fake-factor method, described in Section 7.3.1. In the $\tau_{\text{had}}\tau_{\text{had}}$ channel, the multijet background is estimated using a data-driven fake-factor method as described in Section ?? and

the $t\bar{t}$ background with fake- τ_{had} is estimated using a scale-factor method with scale-factors derived from data to correct the MC prediction as described in Section ??.

Events with electrons or muons that are misidentified as τ_{had} objects, dominantly coming from the $t\bar{t}$ production, represent a minor background in the analysis and they are estimated from simulation. This background is treated together with the $t\bar{t}$ events containing true- τ_{had} objects.

7.3.1 Fake- τ backgrounds in the $\tau_{\text{lep}}\tau_{\text{had}}$ channel

Background processes where a jet is misidentified as a τ_{had} , referred to as fake- τ_{had} processes, are estimated using a data-driven method due to imperfect MC modelling of these processes. Feynman diagrams in Figure 7.3 show examples of the two dominant processes contributing to the fake- τ_{had} background, which are $t\bar{t}$ and multi-jet (QCD) processes. In $t\bar{t}$ events, the fake- τ_{had} typically originates from quark initiated jets from top-quark decay; in multi-jet events jets initiated from both quark and gluon can be misidentified as τ_{had} .

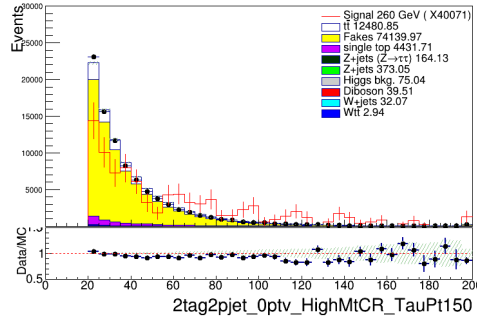


Figure 7.3: Plots of the $\tau_{\text{had}} p_T$ distributions for the (left) anti- τ_{had} and (right) τ_{had} selection for the (top) single lepton trigger and (bottom) lepton-plus-tau trigger selections in the $t\bar{t}$ control region with 1-prong τ_{had} .

The strategy for estimating such background is based on the ‘fake factor’ (FF) method. The FF is a measure of the ratio of the number of signal region events with a fake- τ_{had} , (fake- τ_{had} events) to the number of control region events with a fake- τ_{had} . In the case of the $b\bar{b}\tau^+\tau^-$ channel, a fake- τ_{had} enriched region is provided by the anti- τ_{had} selection (anti- τ_{had} region), as defined in Section ?? TODO: add reference to antitau selection. In the case where the event contains more than one anti- τ_{had} , one is chosen randomly. Derived variables used in the analysis, such as the $E_{\text{T}}^{\text{miss}}$, $m_{\text{T}}^{\text{MMC}}$ and $E_{\text{T}}^{\text{miss}}\phi$ centrality are calculated in the same way as for signal events, but with the anti- τ_{had} taking the place of the loose τ_{had} candidate. Given

that, the fake factor is calculated as:

$$FF = \frac{N(\text{loose } \tau_{\text{had}})}{N(\text{anti-}\tau_{\text{had}})} \quad (7.2)$$

where $N(\text{loose } \tau_{\text{had}})$ ($N(\text{anti-}\tau_{\text{had}})$) is the number of data events with a nominal τ_{had} ($\text{anti-}\tau_{\text{had}}$) with contributions from true τ_{had} subtracted from each term. Due to the different origins of the fake- τ_{had} , the FF are calculated separately for $t\bar{t}$ and multi-jet, and for 1 and 3-prong τ_{had} candidates. For each process the FF are calculated in a dedicated background enriched region. The control regions for each process are defined as follows:

- $t\bar{t}$ CR: $m_{bb} > 150$ GeV, 2 b -tag
- Multi-jet (QCD) CR: inverted lepton isolation ('tight' electrons and 'medium' muons are required to fail their respective 'loose' isolation working points), 2 b -tag.

Individual fake-factors for each process are then used to provide a combined fake-factor. The combined FF is then applied to the anti- τ_{had} events in order to extrapolate to the SR which gives an estimation of the fake- τ_{had} events in the SR. The combined fake-factor is defined as:

$$FF(\text{comb}) = FF(\text{QCD}) \times r_{\text{QCD}} + FF(t\bar{t}) \times (1 - r_{\text{QCD}}) \quad (7.3)$$

where r_{QCD} is measured as a function of the $\tau_{\text{had}} p_{\text{T}}$ and defined as the fraction of multi-jet events in the anti-tau signal region:

$$r_{\text{QCD}} = \frac{N(\text{multi-jet, data})}{N(\text{data}) - N(\text{true } \tau_{\text{had}}, \text{MC})} \quad (7.4)$$

where the $N(\text{multi-jet, data})$ is calculated by subtracting all background contributions apart from multi-jet, regardless of whether they contain fake or true- τ_{had} candidates, from the data in the anti- τ_{had} selection:

$$N(\text{multi-jet, data}) = N(\text{data}) - N(\text{true } \tau_{\text{had}}, \text{MC} + \text{fake } \tau_{\text{had}}, \text{MC}) \quad (7.5)$$

The subtracted backgrounds are taken from the MC predictions. In graphical form, the various control regions where the fake factors are measured and applied can be seen in Figure 7.4. The fake factor is parameterized in p_{T} of the τ_{had} , where it shows an obvious trend. The depending on η of the τ_{had} is also checked but no clear trend is found, as shown in Figure 7.5, 7.6 for the SLT and LTT channels respectively.

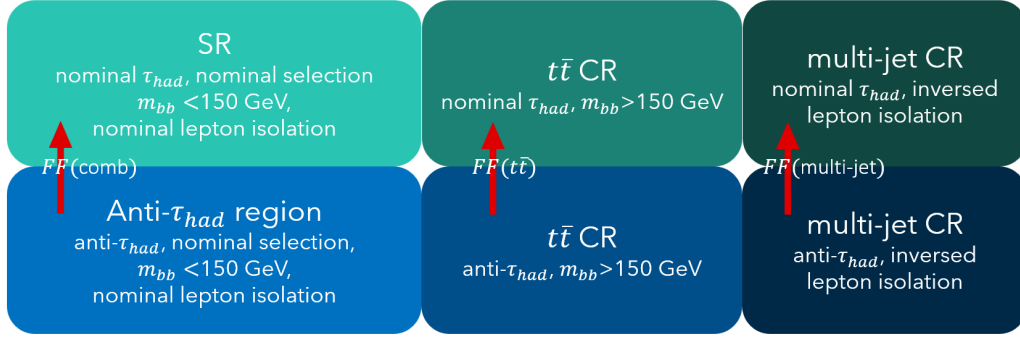


Figure 7.4: Graphical representation of the Combined Fake Factor Method. The fake factors are calculated independently for the $t\bar{t}$ CR and the multi-jet CR, and combined to the combined fake factor. The direction of the arrow indicates the direction of extrapolation when applying the fake factor.

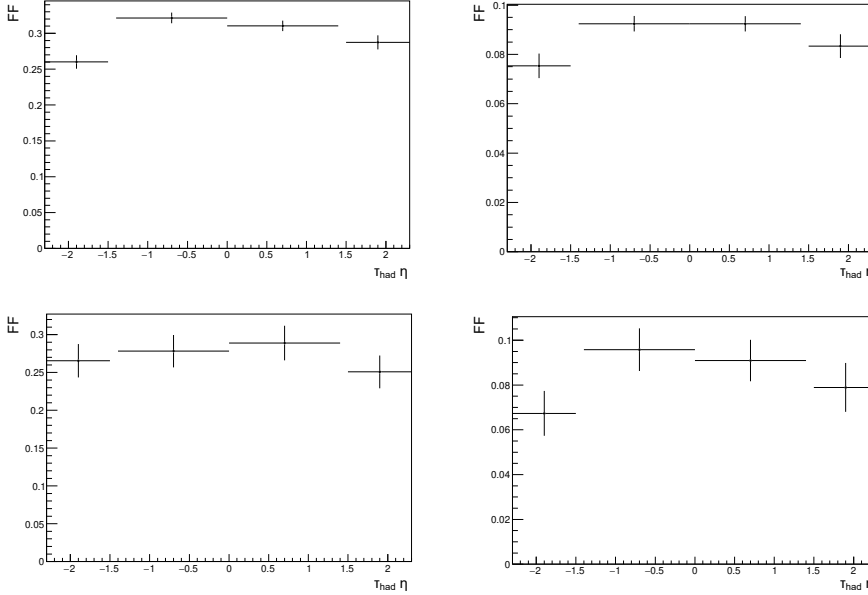


Figure 7.5: Fake-factors as a function of η for 1-prong (left) and 3-prong (right) τ_{had} candidates for $t\bar{t}$ CR (top) and multi-jet (bottom) for the $\tau_{lep}\tau_{had}$ SLT category. No significant trend is observed.

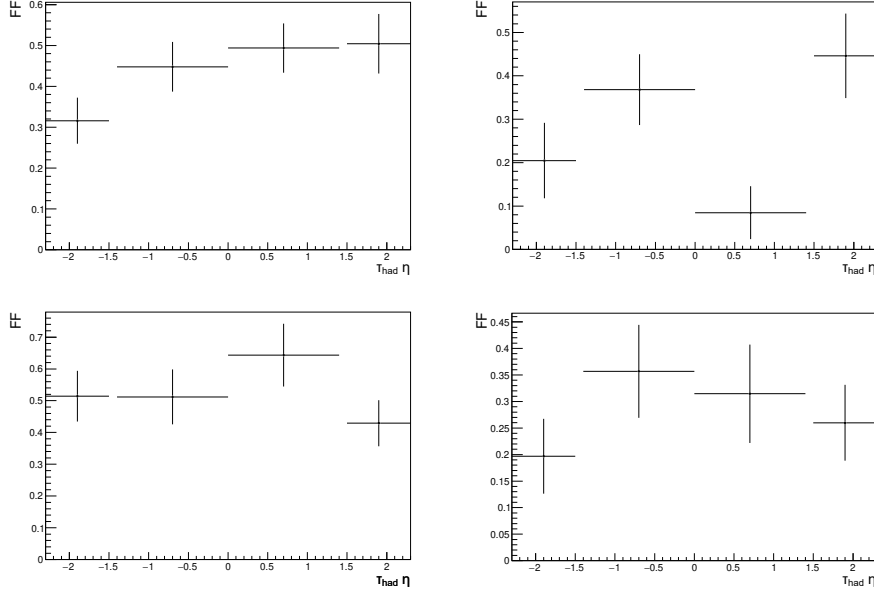


Figure 7.6: Fake-factors as a function of η for 1-prong (left) and 3-prong (right) τ_{had} candidates for $t\bar{t}$ CR (top) and multi-jet (bottom) for the $\tau_{\text{lep}}\tau_{\text{had}}$ LTT category. No significant trend is observed.

The determination of the combined fake factor is sensitive to the modelling of simulated $t\bar{t}$ events with true- τ_{had} given that this is the dominant background that is subtracted from data in the derivation of the FFs and r_{QCD} , and when obtaining the SR Template. Additionally, the derivation of r_{QCD} is sensitive to the modelling of simulated $t\bar{t}$ events with fake- τ_{had} . It was observed that mismodeling in the $t\bar{t}$ background especially in the high jet multiplicity and high top-quark p_T region can cause issues in the calculation of the fake factors, giving non-physical negative values at high $\tau_{\text{had}} p_T$ region. To mitigate this issue, simulated events from $t\bar{t}$ production are differentially reweighted depending on the jet multiplicity and the scalar sum of the transverse momentum of all visible final state objects in the event. These reweighting factors are determined from another $t\bar{t}$ control region ($t\bar{t}$ CR2), which is defined using a selection identical to the SR selection, but with the $t\bar{t}$ CR m_{bb} requirements ($m_{bb} > 150$ GeV) and an additional $m_T^W > 40$ GeV requirement. Furthermore, events in this control region are required to have a reconstructed τ_{had} candidate, but this candidate is not required to pass the RNN τ_{had} identification criteria defined in Section 5.5. The m_T^W requirement is introduced to remove any potential contamination from multi-jet events. The reweighting method is validated in two additional validation region, as described in more details in Appendix ?? TODO: add reference to appendix. The reweighting only applies to the control regions and the anti- τ_{had} region, while it's not necessary applying to the signal region where it would complicate the $t\bar{t}$ systematics

uncertainties and statistical analysis. The $t\bar{t}$ CR and multi-jet CR events with an anti- τ_{had} candidate after the $t\bar{t}$ reweighting are shown in Figure 7.7, 7.8, 7.9 and 7.10. These plots can also be used to check the purity of the fake- τ_{had} events in the $t\bar{t}$ and multi-jet CRs, where the fakes contributions from $t\bar{t}$ are given from MC simulation. In the multi-jet control region, the events show large discrepancy between the data and the MC distributions, as a result of the fakes originating from the multi-jet processes which are not simulated by the MC. A much larger fraction of $t\bar{t}$ fakes are presented in the $t\bar{t}$ CR. The MC does not agree with data very well due to the imperfect $t\bar{t}$ fakes MC simulation, which is the main motivation for using the data-driven FF method.

The calculated fake factors are shown on Figure 7.11 and Figure 7.12, for the SLT and LTT channels respectively. The Fake factors obtained with reweighted and un-weighted $t\bar{t}$ contributions are shown on the same graph. The binning is optimised for the $\text{FF}_{t\bar{t}}$ and the same binning is used for the FF_{QCD} . As a result a smooth trend is observed in the $\text{FF}_{t\bar{t}}$ but some artifacts shapes at mid and high p_T range are shown in the FF_{QCD} . This issue has no visible impact on the fakes estimation, because the $t\bar{t}$ FF dominates over the multi-jet FF in the combined FF which can be seen in the r_{QCD} distribution in the following. The r_{QCD} is computed both for $e\tau_{\text{had}}$ and $\mu\tau_{\text{had}}$ channels, since the QCD contents are different for them. The parameterized r_{QCD} as a function of $p_T(\tau_{\text{had}})$ for 1-prong and 3-prong τ_{had} candidates in $e\tau_{\text{had}}$ and $\mu\tau_{\text{had}}$ channels are shown in Figure 7.13 for the SLT category and in Figure 7.14 for the LTT category.

Statistical uncertainties in $\text{FF}_{t\bar{t}}$, FF_{QCD} and r_{QCD} are evaluated and propagated to the final result, and a conservative 30% modelling uncertainty is assigned to simulated non- $t\bar{t}$ backgrounds which are subtracted from data. The uncertainties due to $t\bar{t}$ modelling issue and its subtraction are discussed in more details in section ??.TODO: add reference to the systematics section. The combined FF method is validated in the 0- b -tagged and 1- b -tagged regions, where the same event selection is applied but with different numbers of b -tagged jets required. The 0- b -tagged region has rich statistics while the 1- b -tagged region is closer to the signal region. The signal contamination in the 0- b -tagged and 1- b -tagged regions is negligible. The estimated background distributions agree well with the observed distributions in all validation regions. The data and MC comparison with fakes estimated with the FF method are shown in Figure ?? for the SLT channel and Figure ?? for the LTT channel.

Figure 7.15 shows the comparison of the contribution of fakes as estimated using MC and using either the fake estimation or data with true τ backgrounds subtracted in the signal region and control region, respectively. As expected, the difference

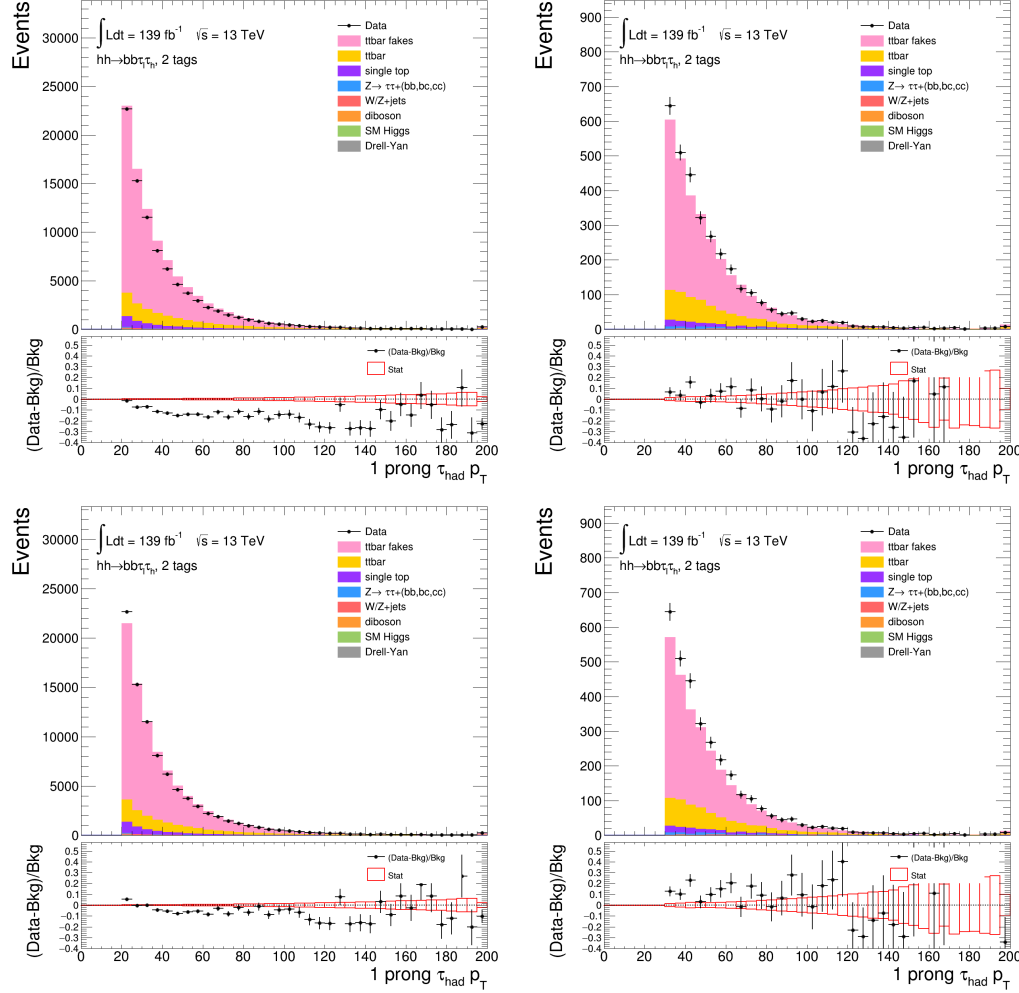


Figure 7.7: Plots of the $\tau_{\text{had}} p_T$ distributions for the SLT (left) and LTT channel (right) with $t\bar{t}$ un-weighted (top) and with $t\bar{t}$ re-weighted (bottom) in the $t\bar{t}$ control region with 1-prong anti- τ_{had} . The $t\bar{t}$ initiated fakes background is labelled as ‘ttbar fakes’ in pink. With true τ_{had} contributions subtracted from data (and with true τ_{had} $t\bar{t}$ reweighted), this region is used as the denominator of the $t\bar{t}$ control region fake factor calculation.

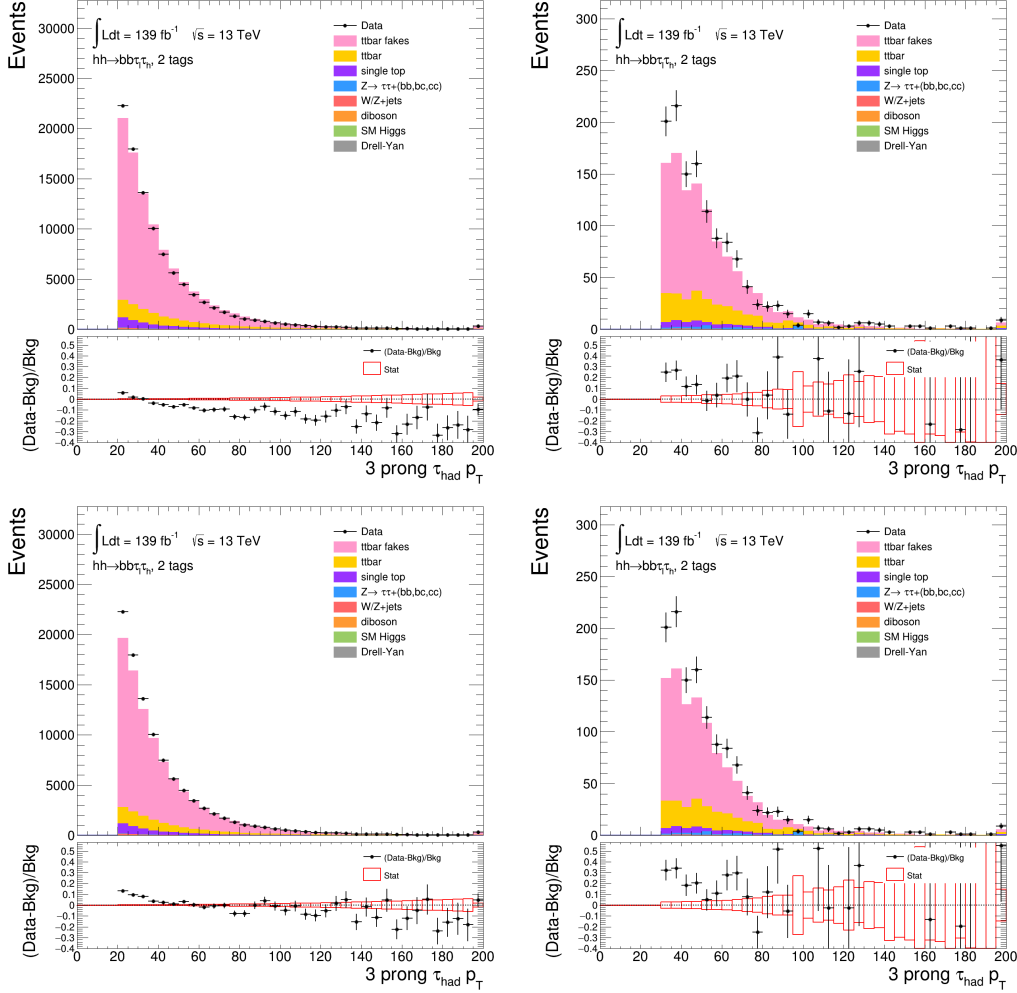


Figure 7.8: Plots of the $\tau_{\text{had}} p_T$ distributions for the SLT (left) and LTT channel (right) with $t\bar{t}$ un-weighted (top) and with $t\bar{t}$ reweighted (bottom) in the $t\bar{t}$ control region with 3-prong anti- τ_{had} . The $t\bar{t}$ initiated fakes background is labelled as ‘ttbar fakes’ in pink. With true τ_{had} contributions subtracted from data (and with true τ_{had} $t\bar{t}$ reweighted), this region is used as the denominator of the $t\bar{t}$ control region fake factor calculation.

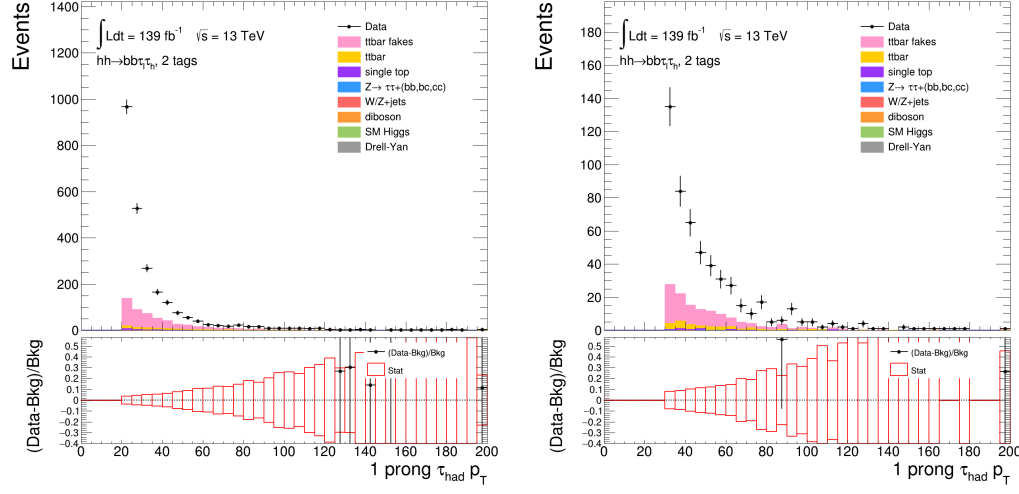


Figure 7.9: Plots of the $\tau_{\text{had}} p_T$ distributions for the SLT (left) and LTT channel (right) with $t\bar{t}$ reweighted in the multi-jet control region with 1-prong anti- τ_{had} . The $t\bar{t}$ initiated fakes background is labelled as ‘ttbar fakes’ in pink. With true τ_{had} contributions subtracted from data, this region is used as the denominator of the $t\bar{t}$ control region fake factor calculation.

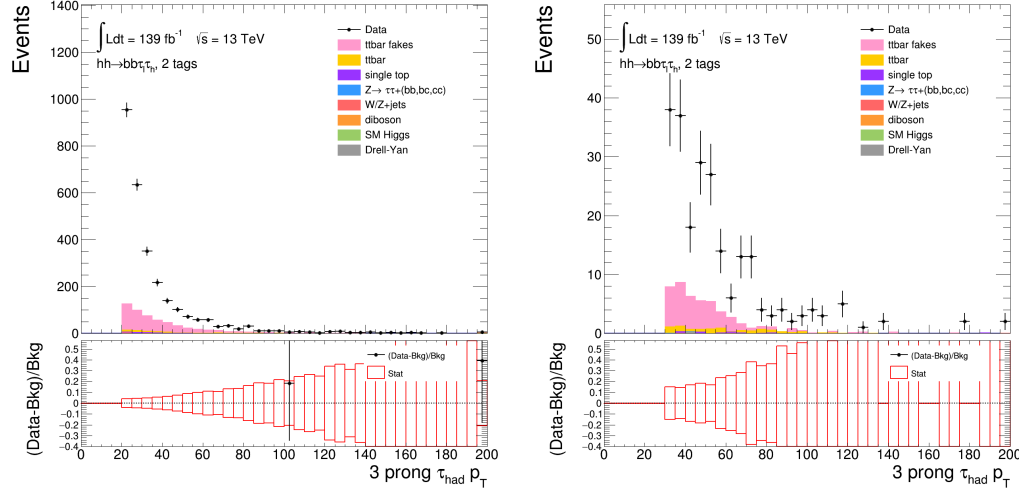


Figure 7.10: Plots of the $\tau_{\text{had}} p_T$ distributions for the SLT (left) and LTT channel (right) with $t\bar{t}$ reweighted. The $t\bar{t}$ initiated fakes background is labelled as ‘ttbar fakes’ in pink. With true τ_{had} contributions subtracted from data, this region is used as the denominator of the multi-jet control region fake factor calculation.

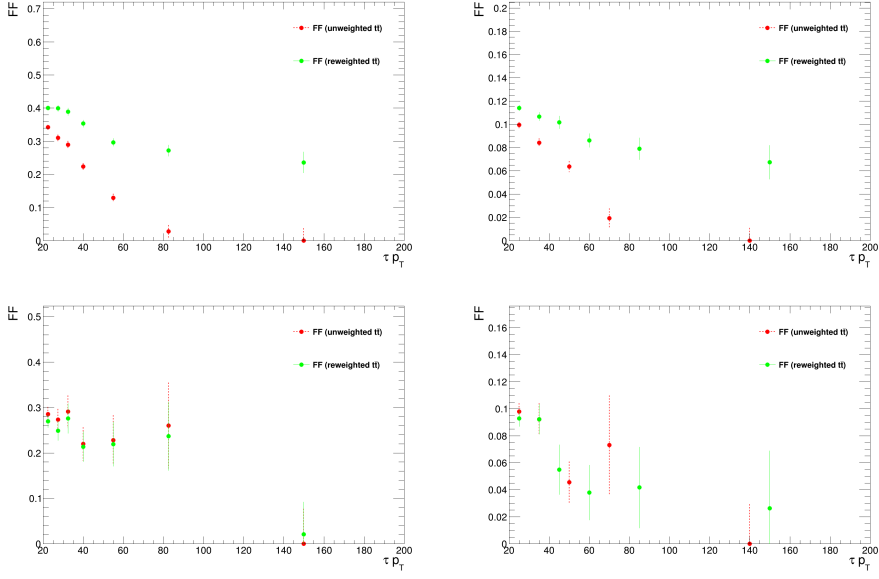


Figure 7.11: Fake-factors for 1-prong (left) and 3-prong (right) τ_{had} candidates for $t\bar{t}$ processes (top) and multi-jet (bottom) for the $\tau_{\text{lep}}\tau_{\text{had}}$ SLT category.

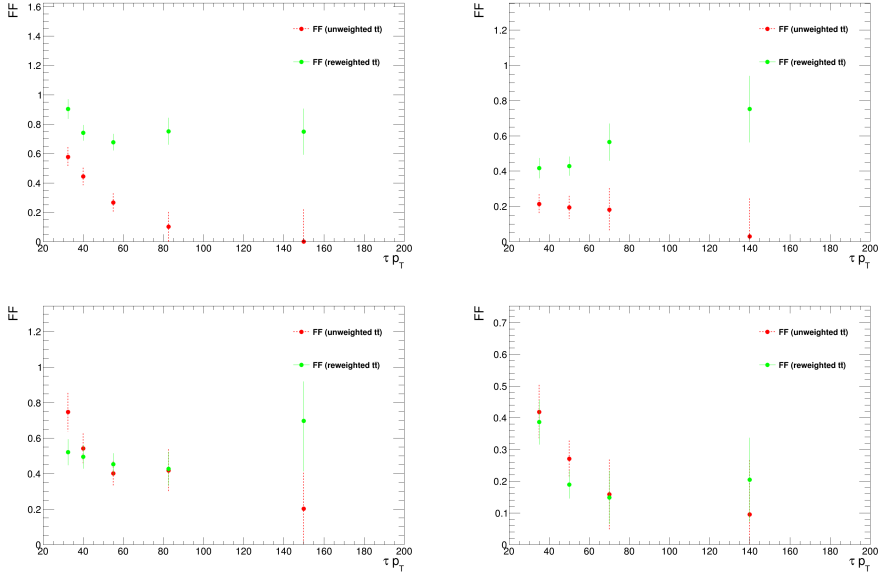


Figure 7.12: Fake-factors for 1-prong (left) and 3-prong (right) τ_{had} candidates for $t\bar{t}$ processes (top) and multi-jet (bottom) for the $\tau_{\text{lep}}\tau_{\text{had}}$ LTT category.

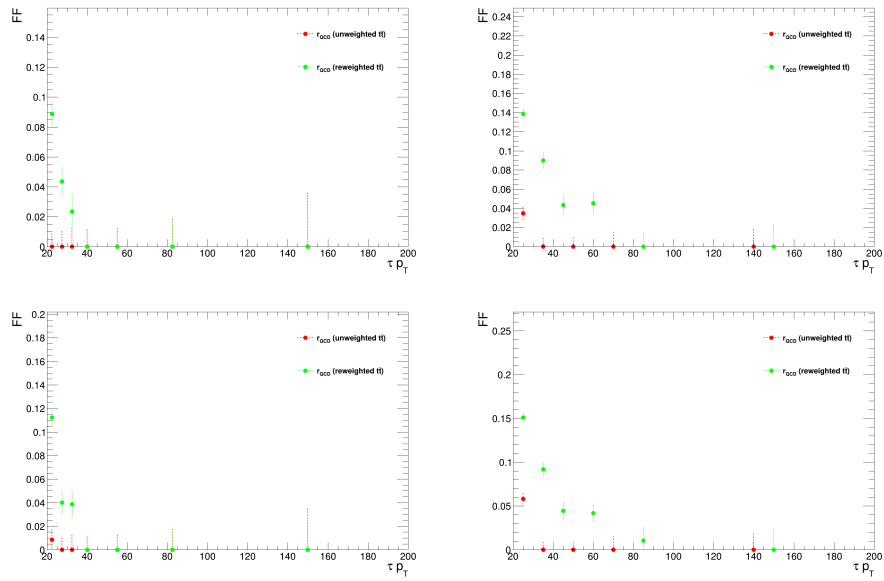


Figure 7.13: r_{QCD} for 1-prong (left) and 3-prong (right) τ_{had} candidates for $e\tau_{\text{had}}$ channel (top) and $\mu\tau_{\text{had}}$ (bottom) for the SLT channel.

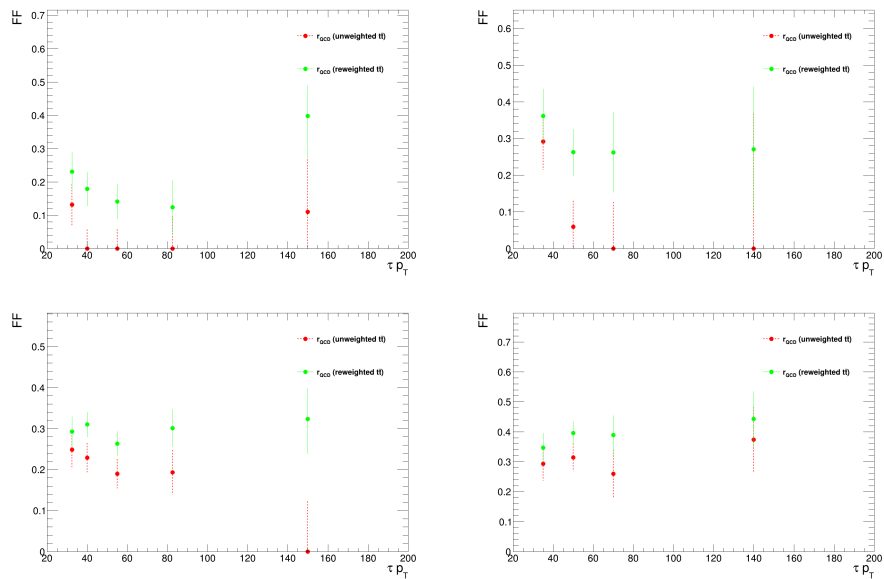


Figure 7.14: r_{QCD} for 1-prong (left) and 3-prong (right) τ_{had} candidates for $e\tau_{\text{had}}$ channel (top) and $\mu\tau_{\text{had}}$ (bottom) LTT channel.

between MC and the data estimate is larger in the LTT channel, where the lower momentum events include more multi-jet events (for which MC is not available). This is shown with the analysis binning algorithm applied to the final discriminant for the non-resonant and several resonant mass points.

To validate the ability of the combined fake factor method to describe the PNN or NN shape, plots have been made using the fake factor method to estimate the combined multi-jet and $t\bar{t}/W$ contribution in validation regions. First, we have applied the combined fake factor method directly to the $t\bar{t}$ CR, as a closure test of the method, which can be seen in Fig. 7.16. The next region is the high statistic and relatively background-enriched 0-tag region, which is the same as the lephad signal region except for the requirement that there are no b -tagged jets. This is shown in Fig. 7.17 and Fig. 7.18 for several mass hypotheses and for the single lepton and lepton-plus-tau trigger categories, respectively. In Fig. 7.19 and Fig. 7.20, a few distributions are also shown for a validation region closer to the signal region, the 1-tag validation region, which requires the same selection as the signal region with the exception of requiring exactly one b -tagged jet. The background estimation appears to agree well with the observed distributions in these validation regions.

It was also requested to see what the SM NN plots looked like in the 0-tag and 1-tag regions with the exact binning used in the signal region, rather than the a binning defined by the algorithm that is used in the signal region. This binning is not derived from the distributions in the 0-tag and 1-tag region at all, but is instead an example of what a binning derived in a different region would look like in the validation regions. This is shown in Fig. 7.21 and Fig. 7.22.

due 15/11

7.4 Multivariate analysis

7.5 Systematic uncertainties

due 30/11

7.6 Results

due 15/12

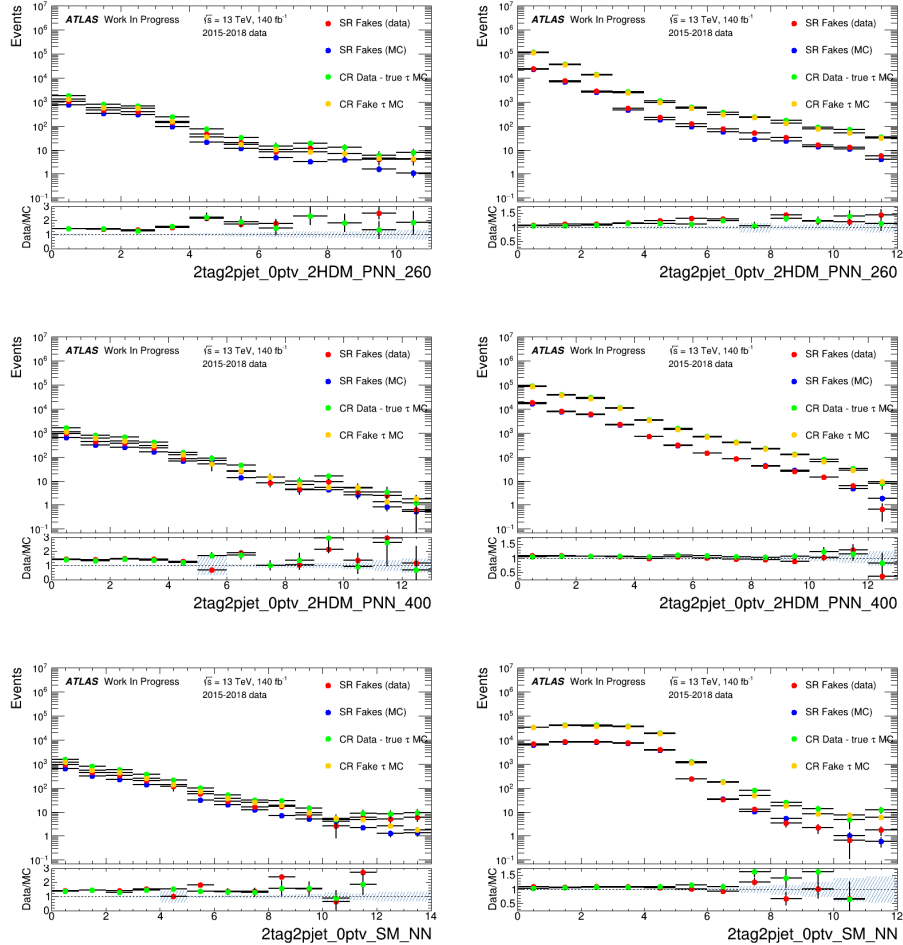


Figure 7.15: A comparison of the contribution of fakes as estimated using MC and using either the fake estimation or data with true τ backgrounds subtracted in the signal region and control region, respectively. Uncertainties are statistical only, and note that multi-jet contributions are included in the data estimates but not the MC. The distributions are the final discriminant for the 260 GeV (top) and 400 GeV (middle) resonant mass points, and the non-resonant discriminant (bottom) for the lepton-plus-tau trigger channel (left) and the single lepton trigger channel (right).

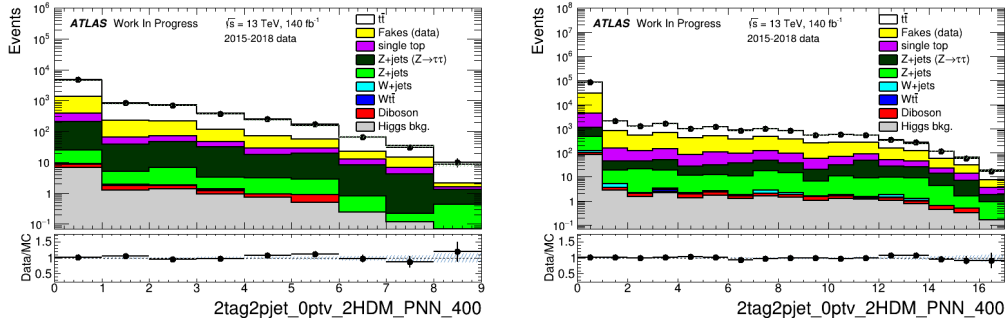


Figure 7.16: The PNN distribution for the $m_X = 400$ GeV mass hypothesis in the signal-depleted $t\bar{t}$ CR where the $t\bar{t}$ FF are measured. This is a simple closure test.

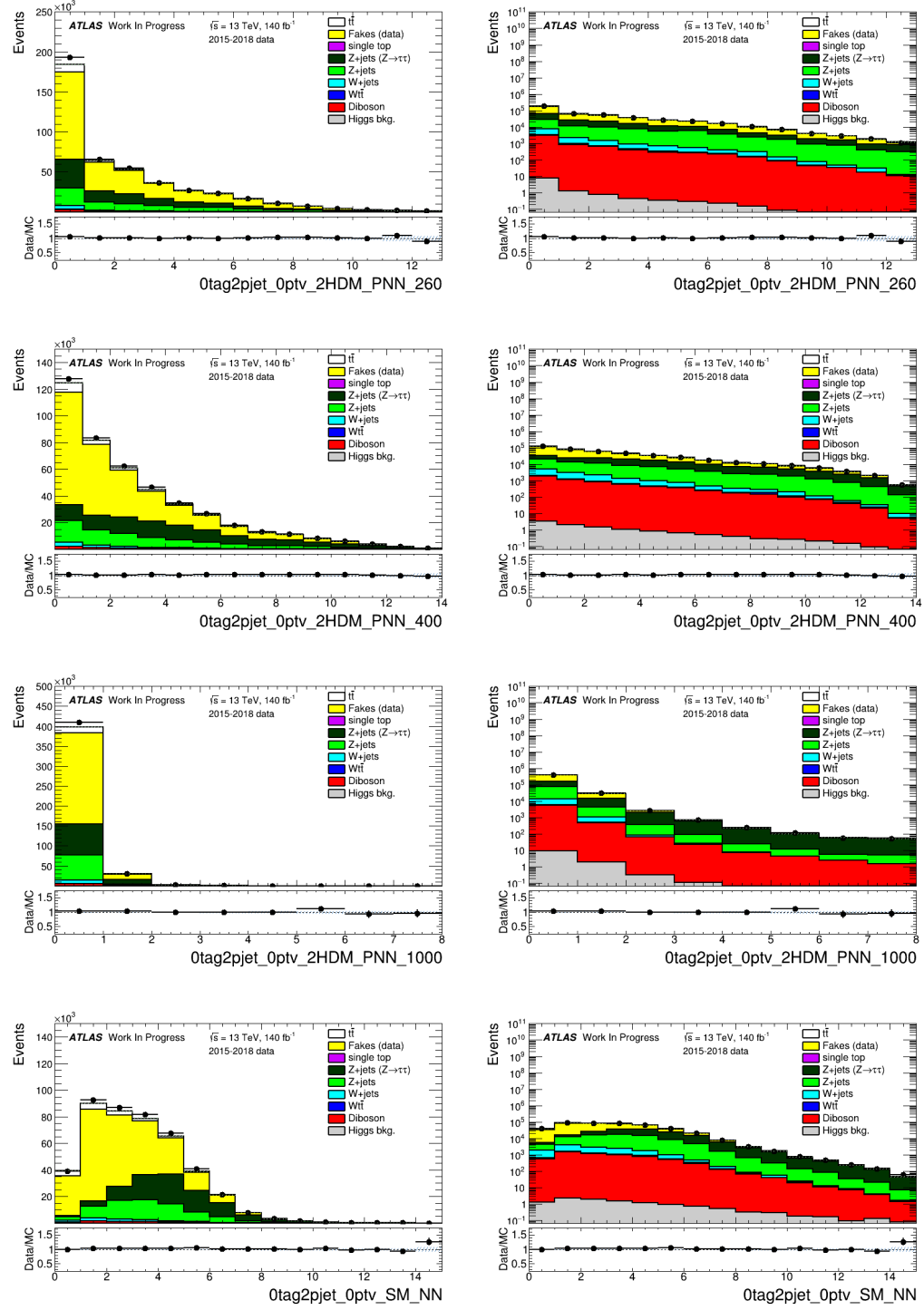


Figure 7.17: The PNN distribution for the $m_X = 260, 400$, and 1000 GeV mass hypotheses and the non-resonant NN distribution in the 0-tag validation region of the single lepton trigger category in (left) linear and (right) log scale. The binning is defined using the same algorithm as is used for the signal region in the final fit, and normalization factors are used for $Z + HF$ (1.33) and $t\bar{t}$ (0.95).

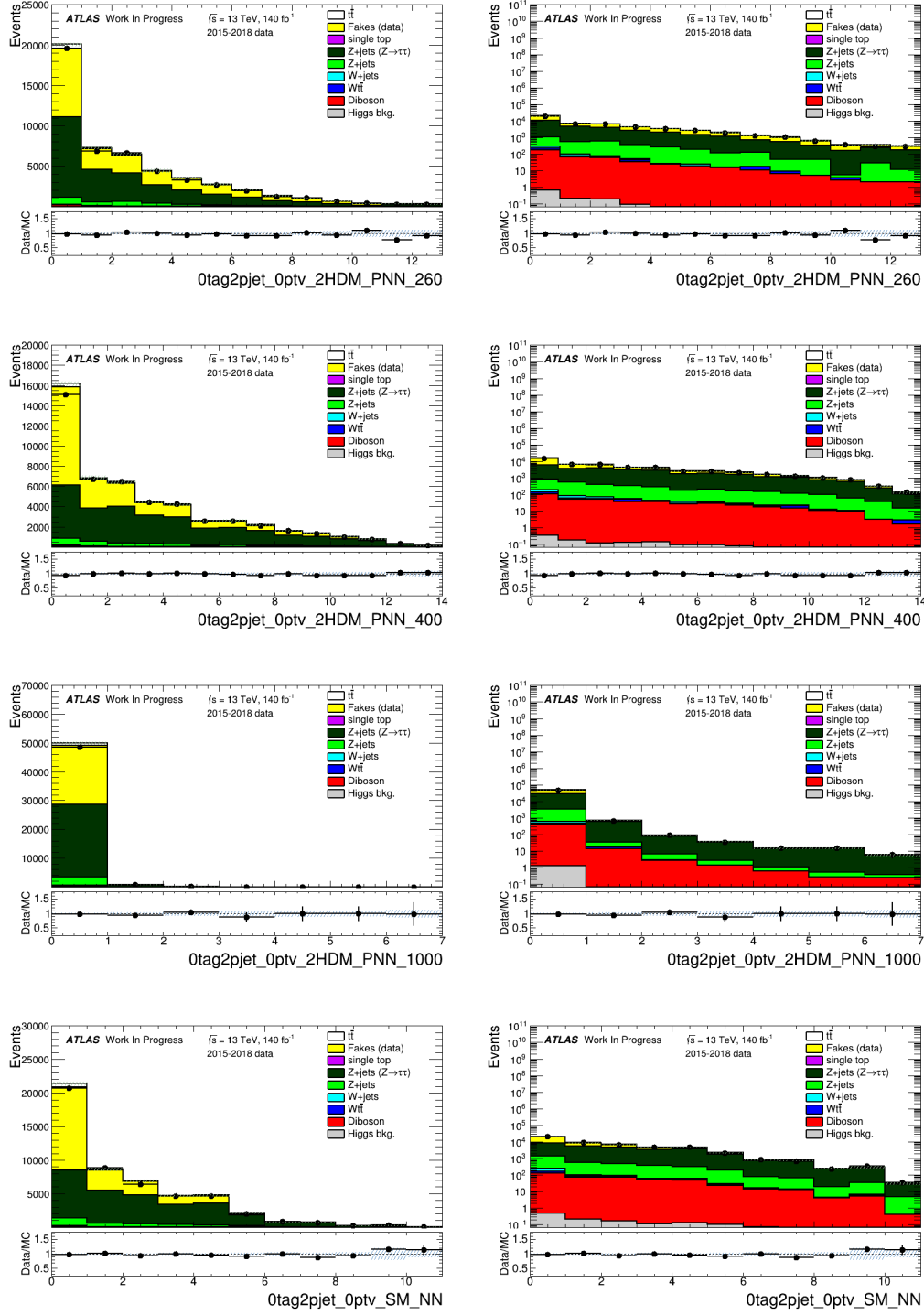


Figure 7.18: The PNN distribution for the $m_X = 260, 400$, and 1000 GeV mass hypotheses and the non-resonant NN distribution in the 0-tag validation region of the lepton-plus-tau trigger category in (left) linear and (right) log scale. The binning is defined using the same algorithm as is used for the signal region in the final fit, and normalization factors are used for $Z + HF$ (1.33) and $t\bar{t}$ (0.95).

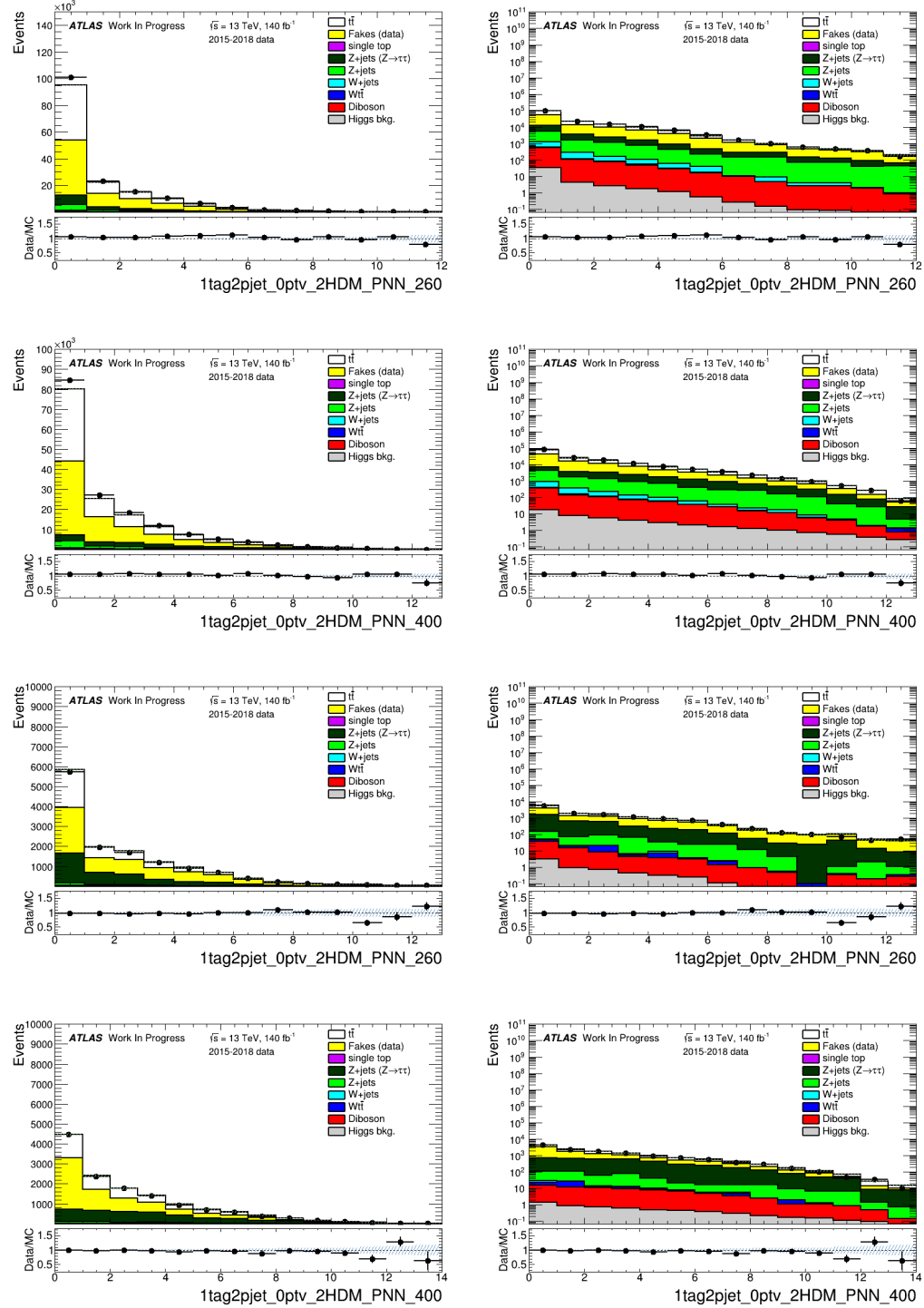


Figure 7.19: The PNN distribution for the $m_X = 260$ and 400 GeV mass hypotheses in the 1-tag validation region of the (top) single lepton trigger category and (bottom) lepton-plus-tau trigger category in (left) linear and (right) log scale. The binning is defined using the same algorithm as is used for the signal region in the final fit, and normalization factors are used for $Z + HF$ (1.33) and $t\bar{t}$ (0.95).

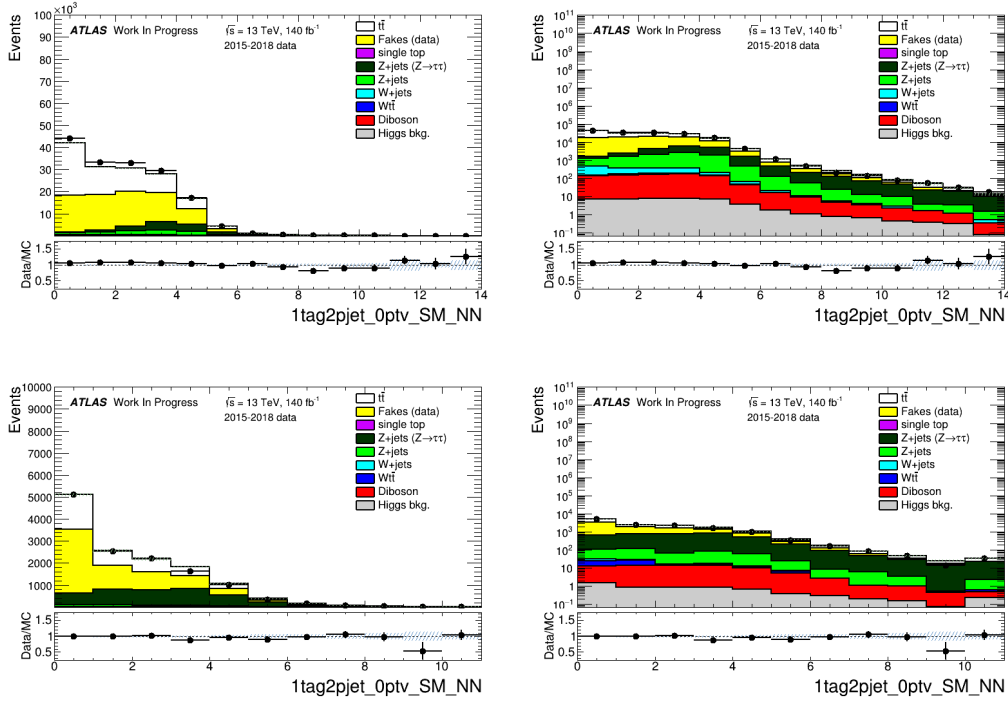


Figure 7.20: The PNN distribution for the non-resonant signal hypothesis in the 1-tag validation region of the (top) single lepton trigger category and (bottom) lepton-plus-tau trigger category in (left) linear and (right) log scale. The binning is defined using the same algorithm as is used for the signal region in the final fit, and normalization factors are used for $Z + HF$ (1.33) and $t\bar{t}$ (0.95).

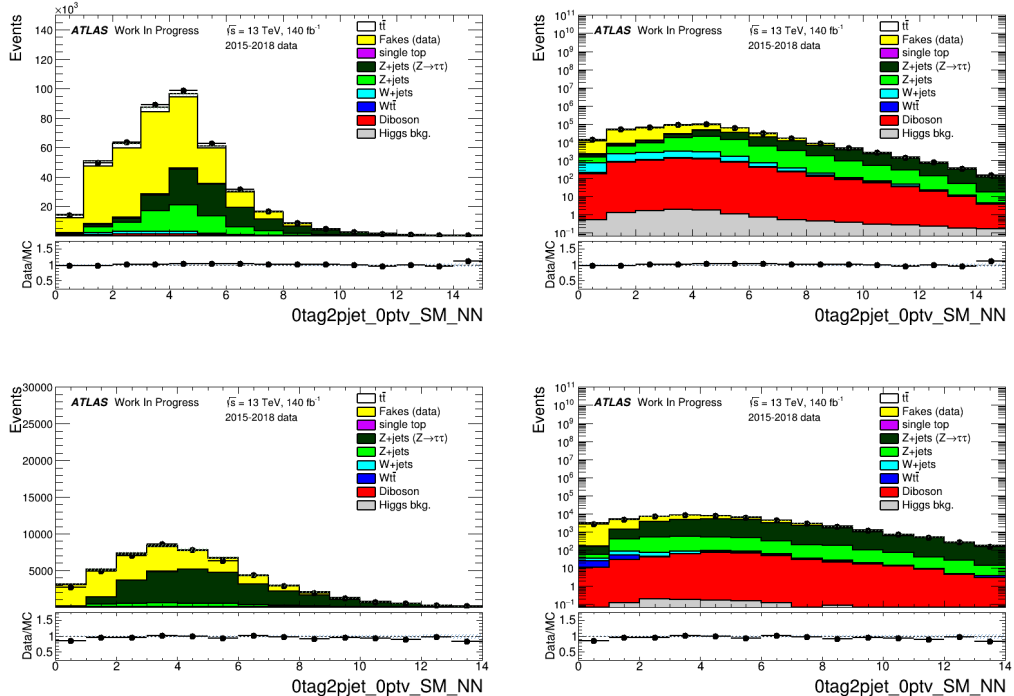


Figure 7.21: The NN distribution for the non-resonant signal hypothesis in the 0-tag validation region of the (top) single lepton trigger category and (bottom) lepton-plus-tau trigger category in (left) linear and (right) log scale. The binning is exactly the same as is used for the signal region in the final fit, and normalization factors are used for $Z + HF$ (1.33) and $t\bar{t}$ (0.95).

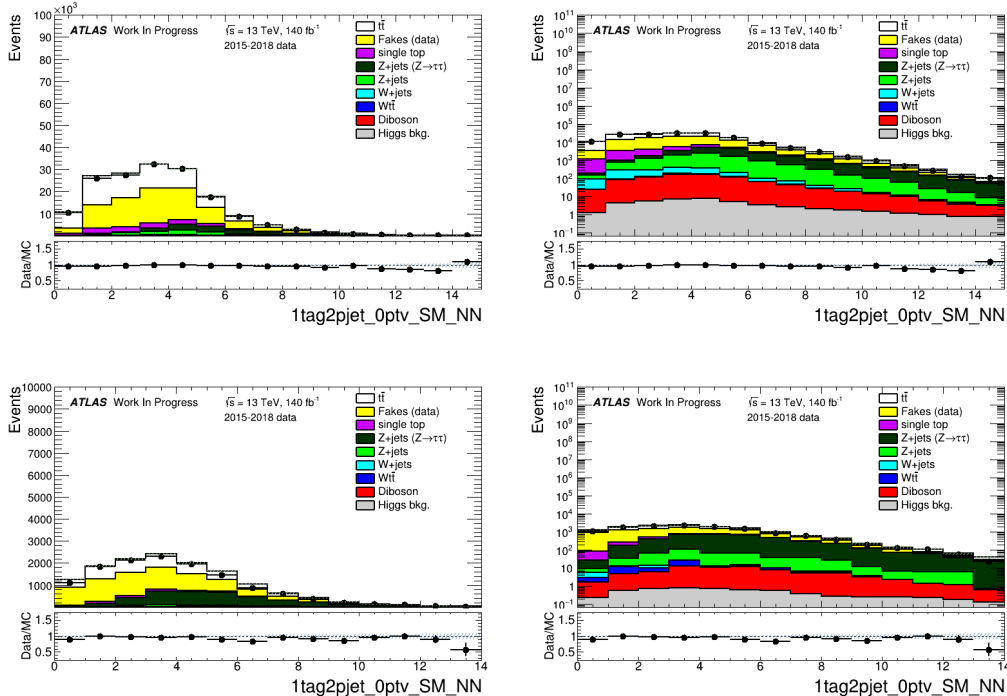


Figure 7.22: The NN distribution for the non-resonant signal hypothesis in the 1-tag validation region of the (top) single lepton trigger category and (bottom) lepton-plus-tau trigger category in (left) linear and (right) log scale. The binning is exactly the same as is used for the signal region in the final fit, and normalization factors are used for $Z + HF$ (1.33) and $t\bar{t}$ (0.95).

Chapter 8

Summary

Bibliography

- [1] Lyndon Evans and Philip Bryant. “LHC Machine”. In: *JINST* 3 (2008), S08001. DOI: [10.1088/1748-0221/3/08/S08001](https://doi.org/10.1088/1748-0221/3/08/S08001).
- [2] ATLAS Collaboration. “The ATLAS Experiment at the CERN Large Hadron Collider”. In: *JINST* 3 (2008), S08003. DOI: [10.1088/1748-0221/3/08/S08003](https://doi.org/10.1088/1748-0221/3/08/S08003).
- [3] S. Chatrchyan et al. “The CMS Experiment at the CERN LHC”. In: *JINST* 3 (2008), S08004. DOI: [10.1088/1748-0221/3/08/S08004](https://doi.org/10.1088/1748-0221/3/08/S08004).
- [4] K. Aamodt et al. “The ALICE experiment at the CERN LHC”. In: *JINST* 3 (2008), S08002. DOI: [10.1088/1748-0221/3/08/S08002](https://doi.org/10.1088/1748-0221/3/08/S08002).
- [5] A. Augusto Alves Jr. et al. “The LHCb Detector at the LHC”. In: *JINST* 3 (2008), S08005. DOI: [10.1088/1748-0221/3/08/S08005](https://doi.org/10.1088/1748-0221/3/08/S08005).
- [6] Stephen Myers. “The LEP collider, from design to approval and commissioning”. In: (Oct. 1991). DOI: [10.5170/CERN-1991-008](https://doi.org/10.5170/CERN-1991-008).
- [7] L Rossi. “The LHC superconducting magnets”. In: 1 (2003), pp. 141–145.
- [8] J. P. Blewett. “200-GeV Intersecting Storage Accelerators”. In: *eConf* C710920 (1971), p. 501.
- [9] Ph Lebrun et al. “Report of the Task Force on the Incident of 19 September 2008 at the LHC”. In: *CERN LHC Project Rep* 1168 (2009).
- [10] R Alemany-Fernandez et al. “Operation and Configuration of the LHC in Run 1”. In: (2013).
- [11] ATLAS Collaboration. “Observation of a new particle in the search for the Standard Model Higgs boson with the ATLAS detector at the LHC”. In: *Phys. Lett. B* 716 (2012), p. 1. DOI: [10.1016/j.physletb.2012.08.020](https://doi.org/10.1016/j.physletb.2012.08.020). arXiv: [1207.7214 \[hep-ex\]](https://arxiv.org/abs/1207.7214).
- [12] ATLAS Collaboration. “A Particle Consistent with the Higgs Boson Observed with the ATLAS Detector at the Large Hadron Collider”. In: *Science* 338 (2012), p. 1576. DOI: [10.1126/science.1232005](https://doi.org/10.1126/science.1232005).
- [13] F Bordry et al. “The first long shutdown (LS1) for the LHC”. In: (2013).

- [14] Jorg Wenninger. “Operation and Configuration of the LHC in Run 2”. In: (Mar. 2019). URL: <https://cds.cern.ch/record/2668326>.
- [15] Georges Aad et al. “ATLAS data quality operations and performance for 2015–2018 data-taking”. In: *JINST* 15.04 (2020), P04003.
- [16] ATLAS Collaboration. *ATLAS Pixel Detector: Technical Design Report*. ATLAS-TDR-11; CERN-LHCC-98-013. 1998. URL: <https://cds.cern.ch/record/381263>.
- [17] ATLAS Collaboration. *ATLAS Inner Detector: Technical Design Report, Volume 1*. ATLAS-TDR-4; CERN-LHCC-97-016. 1997. URL: <https://cds.cern.ch/record/331063>.
- [18] ATLAS Collaboration. *ATLAS Liquid Argon Calorimeter: Technical Design Report*. ATLAS-TDR-2; CERN-LHCC-96-041. 1996. URL: <https://cds.cern.ch/record/331061>.
- [19] ATLAS Collaboration. *ATLAS Tile Calorimeter: Technical Design Report*. ATLAS-TDR-3; CERN-LHCC-96-042. 1996. URL: <https://cds.cern.ch/record/331062>.
- [20] ATLAS Collaboration. *ATLAS Muon Spectrometer: Technical Design Report*. ATLAS-TDR-10; CERN-LHCC-97-022. CERN, 1997. URL: <https://cds.cern.ch/record/331068>.
- [21] ATLAS Collaboration. *ATLAS Magnet System: Magnet Project Technical Design Report, Volume 1*. ATLAS-TDR-6; CERN-LHCC-97-018. 1997. URL: <https://cds.cern.ch/record/338080>.
- [22] ATLAS Collaboration. *ATLAS Insertable B-Layer: Technical Design Report*. ATLAS-TDR-19; CERN-LHCC-2010-013. 2010. URL: <https://cds.cern.ch/record/1291633>.
- [23] J. Pequenao. *Computer generated image of the ATLAS inner detector*. 2008. URL: <https://cds.cern.ch/record/1095926>.
- [24] ATLAS Collaboration. *ATLAS Calorimeter Performance: Technical Design Report*. ATLAS-TDR-1; CERN-LHCC-96-040. 1996. URL: <https://cds.cern.ch/record/331059>.
- [25] ATLAS Collaboration. *ATLAS Level-1 Trigger: Technical Design Report*. ATLAS-TDR-12; CERN-LHCC-98-014. 1998. URL: <https://cds.cern.ch/record/381429>.
- [26] ATLAS Collaboration. *ATLAS High-Level Trigger, Data Acquisition and Controls: Technical Design Report*. ATLAS-TDR-16; CERN-LHCC-2003-022. 2003. URL: <https://cds.cern.ch/record/616089>.
- [27] Robert Blair et al. “The ATLAS High Level Trigger Region of Interest Builder”. In: *JINST* 3 (2008), P04001. DOI: [10.1088/1748-0221/3/04/P04001](https://doi.org/10.1088/1748-0221/3/04/P04001). arXiv: [0711.3217](https://arxiv.org/abs/0711.3217) [physics.ins-det].

- [28] ATLAS Collaboration. “Performance of the ATLAS Inner Detector Track and Vertex Reconstruction in High Pile-Up LHC Environment”. In: (2012). URL: <https://cds.cern.ch/record/1435196>.
- [29] ATLAS Collaboration. “Performance of the ATLAS track reconstruction algorithms in dense environments in LHC Run 2”. In: *Eur. Phys. J. C* 77 (2017), p. 673. DOI: [10.1140/epjc/s10052-017-5225-7](https://doi.org/10.1140/epjc/s10052-017-5225-7). arXiv: [1704.07983 \[hep-ex\]](https://arxiv.org/abs/1704.07983).
- [30] Azriel Rosenfeld and John L. Pfaltz. “Sequential Operations in Digital Picture Processing”. In: *J. ACM* 13.4 (Oct. 1966), pp. 471–494. ISSN: 0004-5411. DOI: [10.1145/321356.321357](https://doi.org/10.1145/321356.321357). URL: <https://doi.org/10.1145/321356.321357>.
- [31] R. Frühwirth. “Application of Kalman filtering to track and vertex fitting”. In: *Nuclear Instruments and Methods in Physics Research Section A: Accelerators, Spectrometers, Detectors and Associated Equipment* 262.2 (1987), pp. 444–450. ISSN: 0168-9002. DOI: [https://doi.org/10.1016/0168-9002\(87\)90887-4](https://doi.org/10.1016/0168-9002(87)90887-4). URL: <https://www.sciencedirect.com/science/article/pii/0168900287908874>.
- [32] ATLAS Collaboration. “Performance of the ATLAS Silicon Pattern Recognition Algorithm in Data and Simulation at $\sqrt{s} = 7$ TeV”. In: (2010). URL: <https://cds.cern.ch/record/1281363>.
- [33] ATLAS Collaboration. “Performance of primary vertex reconstruction in proton–proton collisions at $\sqrt{s} = 7$ TeV in the ATLAS experiment”. In: (2010). URL: <https://cds.cern.ch/record/1281344>.
- [34] ATLAS Collaboration. “Electron reconstruction and identification in the ATLAS experiment using the 2015 and 2016 LHC proton–proton collision data at $\sqrt{s} = 13$ TeV”. In: *Eur. Phys. J. C* 79 (2019), p. 639. DOI: [10.1140/epjc/s10052-019-7140-6](https://doi.org/10.1140/epjc/s10052-019-7140-6). arXiv: [1902.04655 \[hep-ex\]](https://arxiv.org/abs/1902.04655).
- [35] W Lampl et al. *Calorimeter Clustering Algorithms: Description and Performance*. Tech. rep. Geneva: CERN, Apr. 2008. URL: <https://cds.cern.ch/record/1099735>.
- [36] ATLAS Collaboration. “Improved electron reconstruction in ATLAS using the Gaussian Sum Filter-based model for bremsstrahlung”. In: (2012). URL: <https://cds.cern.ch/record/1449796>.
- [37] ATLAS Collaboration. “Electron and photon performance measurements with the ATLAS detector using the 2015–2017 LHC proton–proton collision data”. In: *JINST* 14 (2019), P12006. DOI: [10.1088/1748-0221/14/12/P12006](https://doi.org/10.1088/1748-0221/14/12/P12006). arXiv: [1908.00005 \[hep-ex\]](https://arxiv.org/abs/1908.00005).

- [38] ATLAS Collaboration. “Muon reconstruction and identification efficiency in ATLAS using the full Run 2 pp collision data set at $\sqrt{s} = 13$ TeV”. In: *Eur. Phys. J. C* 81 (2020), p. 578. DOI: [10.1140/epjc/s10052-021-09233-2](https://doi.org/10.1140/epjc/s10052-021-09233-2). arXiv: [2012.00578 \[hep-ex\]](https://arxiv.org/abs/2012.00578).
- [39] ATLAS Collaboration. “Muon reconstruction performance of the ATLAS detector in proton–proton collision data at $\sqrt{s} = 13$ TeV”. In: *Eur. Phys. J. C* 76 (2016), p. 292. DOI: [10.1140/epjc/s10052-016-4120-y](https://doi.org/10.1140/epjc/s10052-016-4120-y). arXiv: [1603.05598 \[hep-ex\]](https://arxiv.org/abs/1603.05598).
- [40] ATLAS Collaboration. “Recommended isolation working points”. In: (). URL: https://twiki.cern.ch/twiki/bin/viewauth/AtlasProtected/RecommendedIsolationWPs#Muon_working_points.
- [41] Ryan Atkin. “Review of jet reconstruction algorithms”. In: *Journal of Physics: Conference Series*. Vol. 645. 1. IOP Publishing. 2015, p. 012008.
- [42] ATLAS Collaboration. “Topological cell clustering in the ATLAS calorimeters and its performance in LHC Run 1”. In: *The European Physical Journal C* 77.7 (July 2017). ISSN: 1434-6052. DOI: [10.1140/epjc/s10052-017-5004-5](https://doi.org/10.1140/epjc/s10052-017-5004-5). URL: <http://dx.doi.org/10.1140/epjc/s10052-017-5004-5>.
- [43] ATLAS Collaboration. “Jet reconstruction and performance using particle flow with the ATLAS Detector”. In: *Eur. Phys. J. C* 77 (2017), p. 466. DOI: [10.1140/epjc/s10052-017-5031-2](https://doi.org/10.1140/epjc/s10052-017-5031-2). arXiv: [1703.10485 \[hep-ex\]](https://arxiv.org/abs/1703.10485).
- [44] Matteo Cacciari, Gavin P Salam, and Gregory Soyez. “The anti- k_t jet clustering algorithm”. In: *Journal of High Energy Physics* 2008.04 (Apr. 2008), pp. 063–063. DOI: [10.1088/1126-6708/2008/04/063](https://doi.org/10.1088/1126-6708/2008/04/063). URL: <https://doi.org/10.1088/1126-6708/2008/04/063>.
- [45] ATLAS Collaboration. “Jet energy scale measurements and their systematic uncertainties in proton–proton collisions at $\sqrt{s} = 13$ TeV with the ATLAS detector”. In: *Phys. Rev. D* 96 (2017), p. 072002. DOI: [10.1103/PhysRevD.96.072002](https://doi.org/10.1103/PhysRevD.96.072002). arXiv: [1703.09665 \[hep-ex\]](https://arxiv.org/abs/1703.09665).
- [46] ATLAS Collaboration. “Jet energy scale and resolution measured in proton–proton collisions at $\sqrt{s} = 13$ TeV with the ATLAS detector”. In: (2020). arXiv: [2007.02645 \[hep-ex\]](https://arxiv.org/abs/2007.02645).
- [47] ATLAS Collaboration. “Tagging and suppression of pileup jets with the ATLAS detector”. In: (2014). URL: <https://cds.cern.ch/record/1700870>.
- [48] ATLAS Collaboration. “Summary of the ATLAS experiment’s sensitivity to supersymmetry after LHC Run 1 — interpreted in the phenomenological MSSM”. In: *JHEP* 10 (2015), p. 134. DOI: [10.1007/JHEP10\(2015\)134](https://doi.org/10.1007/JHEP10(2015)134). arXiv: [1508.06608 \[hep-ex\]](https://arxiv.org/abs/1508.06608).

- [49] ATLAS Collaboration. “Combination of searches for Higgs boson pairs in pp collisions at 13 TeV with the ATLAS experiment”. In: (2018). URL: <https://cds.cern.ch/record/2638212>.
- [50] Dean Carmi et al. “Interpreting LHC Higgs results from natural new physics perspective”. In: *Journal of High Energy Physics* 2012.7 (July 2012). ISSN: 1029-8479. DOI: [10.1007/jhep07\(2012\)136](https://doi.org/10.1007/jhep07(2012)136). URL: [http://dx.doi.org/10.1007/JHEP07\(2012\)136](http://dx.doi.org/10.1007/JHEP07(2012)136).
- [51] “Performance of b -jet identification in the ATLAS experiment”. In: *Journal of Instrumentation* 11.04 (Apr. 2016), P04008–P04008. ISSN: 1748-0221. DOI: [10.1088/1748-0221/11/04/p04008](https://doi.org/10.1088/1748-0221/11/04/p04008). URL: <http://dx.doi.org/10.1088/1748-0221/11/04/P04008>.
- [52] ATLAS Collaboration. “ATLAS b -jet identification performance and efficiency measurement with $t\bar{t}$ events in pp collisions at $\sqrt{s} = 13$ TeV”. In: *Eur. Phys. J. C* 79 (2019), p. 970. DOI: [10.1140/epjc/s10052-019-7450-8](https://doi.org/10.1140/epjc/s10052-019-7450-8). arXiv: [1907.05120 \[hep-ex\]](https://arxiv.org/abs/1907.05120).
- [53] Luca Scodellaro. “ b tagging in ATLAS and CMS”. In: (2017). arXiv: [1709.01290 \[hep-ex\]](https://arxiv.org/abs/1709.01290). URL: <https://arxiv.org/abs/1709.01290>.
- [54] ATLAS Collaboration. “Optimisation and performance studies of the ATLAS b -tagging algorithms for the 2017-18 LHC run”. In: (2017). URL: <https://cds.cern.ch/record/2273281>.
- [55] “Optimisation of the ATLAS b -tagging performance for the 2016 LHC Run”. In: ATL-PHYS-PUB-2016-012 (June 2016). URL: <https://cds.cern.ch/record/2160731>.
- [56] M. Tanabashi et al. “Review of Particle Physics”. In: *Phys. Rev. D* 98 (3 Aug. 2018), p. 030001. DOI: [10.1103/PhysRevD.98.030001](https://doi.org/10.1103/PhysRevD.98.030001). URL: <https://link.aps.org/doi/10.1103/PhysRevD.98.030001>.
- [57] *Identification of hadronic tau lepton decays using neural networks in the ATLAS experiment*. Tech. rep. Geneva: CERN, Aug. 2019. URL: <https://cds.cern.ch/record/2688062>.
- [58] ATLAS Collaboration. “A search for resonant and non-resonant Higgs boson pair production in the $b\bar{b}\tau^+\tau^-$ decay channel in pp collisions at $\sqrt{s} = 13$ TeV with the ATLAS detector”. In: *Phys. Rev. Lett.* 121 (2018), p. 191801. DOI: [10.1103/PhysRevLett.121.191801](https://doi.org/10.1103/PhysRevLett.121.191801). arXiv: [1808.00336 \[hep-ex\]](https://arxiv.org/abs/1808.00336). Erratum: in: *Phys. Rev. Lett.* 122 (2019), p. 089901. DOI: [10.1103/PhysRevLett.122.089901](https://doi.org/10.1103/PhysRevLett.122.089901).
- [59] ATLAS Collaboration. “Reconstruction, Energy Calibration, and Identification of Hadronically Decaying Tau Leptons in the ATLAS Experiment for Run-2 of the LHC”. In: (2015). URL: <https://cds.cern.ch/record/2064383>.

- [60] ATLAS Collaboration. “Measurement of the tau lepton reconstruction and identification performance in the ATLAS experiment using pp collisions at $\sqrt{s} = 13$ TeV”. In: (2017). URL: <https://cds.cern.ch/record/2261772>.
- [61] M. *et. al.* Aaboud. “Performance of missing transverse momentum reconstruction with the ATLAS detector using proton–proton collisions at $\sqrt{s} = 13$ TeV”. In: *The European Physical Journal C* 78.11 (Nov. 2018). ISSN: 1434-6052. DOI: [10.1140/epjc/s10052-018-6288-9](https://doi.org/10.1140/epjc/s10052-018-6288-9). URL: <http://dx.doi.org/10.1140/epjc/s10052-018-6288-9>.
- [62] ATLAS Collaboration. “ATLAS Overlap Removal Tool: AssociationUtils”. In: (). URL: <https://gitlab.cern.ch/atlas/athena/tree/21.2/PhysicsAnalysis/AnalysisCommon/AssociationUtils/>.
- [63] ATLAS Collaboration. “Calibration of light-flavour b -jet mistagging rates using ATLAS proton–proton collision data at $\sqrt{s} = 13$ TeV”. In: (2018). URL: <https://cds.cern.ch/record/2314418>.
- [64] David Krohn, Jesse Thaler, and Lian-Tao Wang. “Jets with variable R”. In: 2009.06 (June 2009), pp. 059–059. DOI: [10.1088/1126-6708/2009/06/059](https://doi.org/10.1088/1126-6708/2009/06/059). URL: <https://doi.org/10.1088/1126-6708/2009/06/059>.
- [65] G. Abbiendi et al. “A measurement of the rate of charm production in W decays”. In: *Physics Letters B* 490.1-2 (Sept. 2000), pp. 71–86. ISSN: 0370-2693. DOI: [10.1016/s0370-2693\(00\)00971-0](https://doi.org/10.1016/s0370-2693(00)00971-0). URL: [http://dx.doi.org/10.1016/S0370-2693\(00\)00971-0](http://dx.doi.org/10.1016/S0370-2693(00)00971-0).
- [66] K.A. Olive. “Review of Particle Physics”. In: *Chinese Physics C* 38.9 (Aug. 2014), p. 090001. DOI: [10.1088/1674-1137/38/9/090001](https://doi.org/10.1088/1674-1137/38/9/090001). URL: <https://doi.org/10.1088/1674-1137/38/9/090001>.
- [67] Johannes Erdmann et al. “A likelihood-based reconstruction algorithm for top-quark pairs and the KLFitter framework”. In: *Nuclear Instruments and Methods in Physics Research Section A: Accelerators, Spectrometers, Detectors and Associated Equipment* 748 (2014), pp. 18–25. ISSN: 0168-9002. DOI: <https://doi.org/10.1016/j.nima.2014.02.029>.
- [68] ATLAS Collaboration. “Luminosity determination in pp collisions at $\sqrt{s} = 7$ TeV using the ATLAS detector at the LHC”. In: *Eur. Phys. J. C* 71 (2011), p. 1630. DOI: [10.1140/epjc/s10052-011-1630-5](https://doi.org/10.1140/epjc/s10052-011-1630-5). arXiv: [1101.2185 \[hep-ex\]](https://arxiv.org/abs/1101.2185).
- [69] ATLAS Collaboration. “Improved luminosity determination in pp collisions at $\sqrt{s} = 7$ TeV using the ATLAS detector at the LHC”. In: *Eur. Phys. J. C* 73 (2013), p. 2518. DOI: [10.1140/epjc/s10052-013-2518-3](https://doi.org/10.1140/epjc/s10052-013-2518-3). arXiv: [1302.4393 \[hep-ex\]](https://arxiv.org/abs/1302.4393).

- [70] ATLAS Collaboration. “Luminosity determination in pp collisions at $\sqrt{s} = 8$ TeV using the ATLAS detector at the LHC”. In: *Eur. Phys. J. C* 76 (2016), p. 653. DOI: [10.1140/epjc/s10052-016-4466-1](https://doi.org/10.1140/epjc/s10052-016-4466-1). arXiv: [1608.03953 \[hep-ex\]](https://arxiv.org/abs/1608.03953).
- [71] G. Avoni et al. “The new LUCID-2 detector for luminosity measurement and monitoring in ATLAS”. In: *JINST* 13.07 (2018), P07017. DOI: [10.1088/1748-0221/13/07/P07017](https://doi.org/10.1088/1748-0221/13/07/P07017).
- [72] ATLAS Collaboration. “Performance of the ATLAS muon triggers in Run 2”. In: *JINST* 15.09 (2020), P09015. DOI: [10.1088/1748-0221/15/09/p09015](https://doi.org/10.1088/1748-0221/15/09/p09015). arXiv: [2004.13447 \[hep-ex\]](https://arxiv.org/abs/2004.13447).
- [73] ATLAS Collaboration. “Performance of electron and photon triggers in ATLAS during LHC Run 2”. In: *Eur. Phys. J. C* 80 (2020), p. 47. DOI: [10.1140/epjc/s10052-019-7500-2](https://doi.org/10.1140/epjc/s10052-019-7500-2). arXiv: [1909.00761 \[hep-ex\]](https://arxiv.org/abs/1909.00761).
- [74] ATLAS Collaboration. “The ATLAS Simulation Infrastructure”. In: *Eur. Phys. J. C* 70 (2010), p. 823. DOI: [10.1140/epjc/s10052-010-1429-9](https://doi.org/10.1140/epjc/s10052-010-1429-9). arXiv: [1005.4568 \[physics.ins-det\]](https://arxiv.org/abs/1005.4568).
- [75] S. Agostinelli et al. “GEANT4 – a simulation toolkit”. In: *Nucl. Instrum. Meth. A* 506 (2003), p. 250. DOI: [10.1016/S0168-9002\(03\)01368-8](https://doi.org/10.1016/S0168-9002(03)01368-8).
- [76] Torbjörn Sjöstrand et al. “An introduction to PYTHIA 8.2”. In: *Comput. Phys. Commun.* 191 (2015), p. 159. DOI: [10.1016/j.cpc.2015.01.024](https://doi.org/10.1016/j.cpc.2015.01.024). arXiv: [1410.3012 \[hep-ph\]](https://arxiv.org/abs/1410.3012).
- [77] Richard D. Ball et al. “Parton distributions with LHC data”. In: *Nucl. Phys. B* 867 (2013), p. 244. DOI: [10.1016/j.nuclphysb.2012.10.003](https://doi.org/10.1016/j.nuclphysb.2012.10.003). arXiv: [1207.1303 \[hep-ph\]](https://arxiv.org/abs/1207.1303).
- [78] ATLAS Collaboration. “The Pythia 8 A3 tune description of ATLAS minimum bias and inelastic measurements incorporating the Donnachie–Landshoff diffractive model”. In: (2016). URL: <https://cds.cern.ch/record/2206965>.
- [79] Stefano Frixione, Paolo Nason, and Giovanni Ridolfi. “A positive-weight next-to-leading-order Monte Carlo for heavy flavour hadroproduction”. In: *JHEP* 09 (2007), p. 126. DOI: [10.1088/1126-6708/2007/09/126](https://doi.org/10.1088/1126-6708/2007/09/126). arXiv: [0707.3088 \[hep-ph\]](https://arxiv.org/abs/0707.3088).
- [80] Paolo Nason. “A New method for combining NLO QCD with shower Monte Carlo algorithms”. In: *JHEP* 11 (2004), p. 040. DOI: [10.1088/1126-6708/2004/11/040](https://doi.org/10.1088/1126-6708/2004/11/040). arXiv: [hep-ph/0409146](https://arxiv.org/abs/hep-ph/0409146).
- [81] Stefano Frixione, Paolo Nason, and Carlo Oleari. “Matching NLO QCD computations with Parton Shower simulations: the POWHEG method”. In: *JHEP* 11 (2007), p. 070. DOI: [10.1088/1126-6708/2007/11/070](https://doi.org/10.1088/1126-6708/2007/11/070). arXiv: [0709.2092 \[hep-ph\]](https://arxiv.org/abs/0709.2092).

- [82] Simone Alioli et al. “A general framework for implementing NLO calculations in shower Monte Carlo programs: the POWHEG BOX”. In: *JHEP* 06 (2010), p. 043. DOI: [10.1007/JHEP06\(2010\)043](https://doi.org/10.1007/JHEP06(2010)043). arXiv: [1002.2581 \[hep-ph\]](https://arxiv.org/abs/1002.2581).
- [83] ATLAS Collaboration. “Studies on top-quark Monte Carlo modelling for Top2016”. In: (2016). URL: <https://cds.cern.ch/record/2216168>.
- [84] D. J. Lange. “The EvtGen particle decay simulation package”. In: *Nucl. Instrum. Meth. A* 462 (2001), p. 152. DOI: [10.1016/S0168-9002\(01\)00089-4](https://doi.org/10.1016/S0168-9002(01)00089-4).
- [85] Richard D. Ball et al. “Parton distributions for the LHC run II”. In: *JHEP* 04 (2015), p. 040. DOI: [10.1007/JHEP04\(2015\)040](https://doi.org/10.1007/JHEP04(2015)040). arXiv: [1410.8849 \[hep-ph\]](https://arxiv.org/abs/1410.8849).
- [86] Emanuele Re. “Single-top Wt -channel production matched with parton showers using the POWHEG method”. In: *Eur. Phys. J. C* 71 (2011), p. 1547. DOI: [10.1140/epjc/s10052-011-1547-z](https://doi.org/10.1140/epjc/s10052-011-1547-z). arXiv: [1009.2450 \[hep-ph\]](https://arxiv.org/abs/1009.2450).
- [87] Stefano Frixione et al. “Single-top hadroproduction in association with a W boson”. In: *JHEP* 07 (2008), p. 029. DOI: [10.1088/1126-6708/2008/07/029](https://doi.org/10.1088/1126-6708/2008/07/029). arXiv: [0805.3067 \[hep-ph\]](https://arxiv.org/abs/0805.3067).
- [88] Enrico Bothmann et al. “Event generation with Sherpa 2.2”. In: *SciPost Phys.* 7.3 (2019), p. 034. DOI: [10.21468/SciPostPhys.7.3.034](https://doi.org/10.21468/SciPostPhys.7.3.034). arXiv: [1905.09127 \[hep-ph\]](https://arxiv.org/abs/1905.09127).
- [89] Tanju Gleisberg and Stefan Höche. “Comix, a new matrix element generator”. In: *JHEP* 12 (2008), p. 039. DOI: [10.1088/1126-6708/2008/12/039](https://doi.org/10.1088/1126-6708/2008/12/039). arXiv: [0808.3674 \[hep-ph\]](https://arxiv.org/abs/0808.3674).
- [90] Federico Buccioni et al. “OpenLoops 2”. In: *Eur. Phys. J. C* 79.10 (2019), p. 866. DOI: [10.1140/epjc/s10052-019-7306-2](https://doi.org/10.1140/epjc/s10052-019-7306-2). arXiv: [1907.13071 \[hep-ph\]](https://arxiv.org/abs/1907.13071).
- [91] Fabio Caccioli, Philipp Maierhöfer, and Stefano Pozzorini. “Scattering Amplitudes with Open Loops”. In: *Phys. Rev. Lett.* 108 (2012), p. 111601. DOI: [10.1103/PhysRevLett.108.111601](https://doi.org/10.1103/PhysRevLett.108.111601). arXiv: [1111.5206 \[hep-ph\]](https://arxiv.org/abs/1111.5206).
- [92] Ansgar Denner, Stefan Dittmaier, and Lars Hofer. “COLLIER: A fortran-based complex one-loop library in extended regularizations”. In: *Comput. Phys. Commun.* 212 (2017), pp. 220–238. DOI: [10.1016/j.cpc.2016.10.013](https://doi.org/10.1016/j.cpc.2016.10.013). arXiv: [1604.06792 \[hep-ph\]](https://arxiv.org/abs/1604.06792).
- [93] Steffen Schumann and Frank Krauss. “A parton shower algorithm based on Catani–Seymour dipole factorisation”. In: *JHEP* 03 (2008), p. 038. DOI: [10.1088/1126-6708/2008/03/038](https://doi.org/10.1088/1126-6708/2008/03/038). arXiv: [0709.1027 \[hep-ph\]](https://arxiv.org/abs/0709.1027).
- [94] Stefan Höche et al. “A critical appraisal of NLO+PS matching methods”. In: *JHEP* 09 (2012), p. 049. DOI: [10.1007/JHEP09\(2012\)049](https://doi.org/10.1007/JHEP09(2012)049). arXiv: [1111.1220 \[hep-ph\]](https://arxiv.org/abs/1111.1220).

- [95] Stefan Höche et al. “QCD matrix elements + parton showers. The NLO case”. In: *JHEP* 04 (2013), p. 027. DOI: [10.1007/JHEP04\(2013\)027](https://doi.org/10.1007/JHEP04(2013)027). arXiv: [1207.5030 \[hep-ph\]](https://arxiv.org/abs/1207.5030).
- [96] S. Catani et al. “QCD Matrix Elements + Parton Showers”. In: *JHEP* 11 (2001), p. 063. DOI: [10.1088/1126-6708/2001/11/063](https://doi.org/10.1088/1126-6708/2001/11/063). arXiv: [hep-ph/0109231](https://arxiv.org/abs/hep-ph/0109231).
- [97] Stefan Höche et al. “QCD matrix elements and truncated showers”. In: *JHEP* 05 (2009), p. 053. DOI: [10.1088/1126-6708/2009/05/053](https://doi.org/10.1088/1126-6708/2009/05/053). arXiv: [0903.1219 \[hep-ph\]](https://arxiv.org/abs/0903.1219).
- [98] Charalampos Anastasiou et al. “High precision QCD at hadron colliders: Electroweak gauge boson rapidity distributions at next-to-next-to leading order”. In: *Phys. Rev. D* 69 (2004), p. 094008. DOI: [10.1103/PhysRevD.69.094008](https://doi.org/10.1103/PhysRevD.69.094008). arXiv: [hep-ph/0312266](https://arxiv.org/abs/hep-ph/0312266).
- [99] J. Alwall et al. “The automated computation of tree-level and next-to-leading order differential cross sections, and their matching to parton shower simulations”. In: *JHEP* 07 (2014), p. 079. DOI: [10.1007/JHEP07\(2014\)079](https://doi.org/10.1007/JHEP07(2014)079). arXiv: [1405.0301 \[hep-ph\]](https://arxiv.org/abs/1405.0301).
- [100] ATLAS Collaboration. “ATLAS Pythia 8 tunes to 7 TeV data”. In: (2014). URL: <https://cds.cern.ch/record/1966419>.
- [101] D. J. Lange. “The EvtGen particle decay simulation package”. In: *Nucl. Instrum. Meth. A* 462 (2001), p. 152. DOI: [10.1016/S0168-9002\(01\)00089-4](https://doi.org/10.1016/S0168-9002(01)00089-4).
- [102] ATLAS Collaboration. “Measurements of inclusive and differential fiducial cross-sections of $t\bar{t}$ production with additional heavy-flavour jets in proton–proton collisions at $\sqrt{s} = 13$ TeV with the ATLAS detector”. In: *JHEP* 04 (2019), p. 046. DOI: [10.1007/JHEP04\(2019\)046](https://doi.org/10.1007/JHEP04(2019)046). arXiv: [1811.12113 \[hep-ex\]](https://arxiv.org/abs/1811.12113).
- [103] ATLAS Collaboration. “ATLAS data quality operations and performance for 2015–2018 data-taking”. In: *JINST* 15 (2020), P04003. DOI: [10.1088/1748-0221/15/04/P04003](https://doi.org/10.1088/1748-0221/15/04/P04003). arXiv: [1911.04632 \[physics.ins-det\]](https://arxiv.org/abs/1911.04632).
- [104] G. Avoni et al. “The new LUCID-2 detector for luminosity measurement and monitoring in ATLAS”. In: *JINST* 13.07 (2018), P07017. DOI: [10.1088/1748-0221/13/07/P07017](https://doi.org/10.1088/1748-0221/13/07/P07017).
- [105] T. Sjöstrand, S. Mrenna, and P. Skands. “A brief introduction to PYTHIA 8.1”. In: *Comput. Phys. Commun.* 178 (2008), pp. 852–867. DOI: [10.1016/j.cpc.2008.01.036](https://doi.org/10.1016/j.cpc.2008.01.036). arXiv: [0710.3820 \[hep-ph\]](https://arxiv.org/abs/0710.3820).
- [106] Jon Butterworth et al. “PDF4LHC recommendations for LHC Run II”. In: *J. Phys. G* 43 (2016), p. 023001. DOI: [10.1088/0954-3899/43/2/023001](https://doi.org/10.1088/0954-3899/43/2/023001). arXiv: [1510.03865 \[hep-ph\]](https://arxiv.org/abs/1510.03865).
- [107] ATLAS Collaboration. *Summary of ATLAS Pythia 8 tunes*. ATL-PHYS-PUB-2012-003. 2012. URL: <https://cds.cern.ch/record/1474107>.

- [108] Massimiliano Grazzini et al. “Higgs boson pair production at NNLO with top quark mass effects”. In: *JHEP* 05 (2018), p. 059. DOI: [10.1007/JHEP05\(2018\)059](https://doi.org/10.1007/JHEP05(2018)059). arXiv: [1803.02463 \[hep-ph\]](https://arxiv.org/abs/1803.02463).
- [109] Frédéric A. Dreyer and Alexander Karlberg. “Vector-boson fusion Higgs pair production at N³LO”. In: *Phys. Rev. D* 98.11 (2018), p. 114016. DOI: [10.1103/PhysRevD.98.114016](https://doi.org/10.1103/PhysRevD.98.114016). arXiv: [1811.07906 \[hep-ph\]](https://arxiv.org/abs/1811.07906).
- [110] M. Bähr et al. “Herwig++ physics and manual”. In: *Eur. Phys. J. C* 58 (2008), p. 639. DOI: [10.1140/epjc/s10052-008-0798-9](https://doi.org/10.1140/epjc/s10052-008-0798-9). arXiv: [0803.0883 \[hep-ph\]](https://arxiv.org/abs/0803.0883).
- [111] Johannes Bellm et al. “Herwig 7.0/Herwig++ 3.0 release note”. In: *Eur. Phys. J. C* 76.4 (2016), p. 196. DOI: [10.1140/epjc/s10052-016-4018-8](https://doi.org/10.1140/epjc/s10052-016-4018-8). arXiv: [1512.01178 \[hep-ph\]](https://arxiv.org/abs/1512.01178).
- [112] Stefan Gieseke, Christian Röhr, and Andrzej Siodmok. “Colour reconnections in Herwig++”. In: *Eur. Phys. J. C* 72 (2012), p. 2225. DOI: [10.1140/epjc/s10052-012-2225-5](https://doi.org/10.1140/epjc/s10052-012-2225-5). arXiv: [1206.0041 \[hep-ph\]](https://arxiv.org/abs/1206.0041).
- [113] “Validation of signal Monte Carlo event generation in searches for Higgs boson pairs with the ATLAS detector”. In: (2019).
- [114] Michal Czakon and Alexander Mitov. “Top++: A program for the calculation of the top-pair cross-section at hadron colliders”. In: *Comput. Phys. Commun.* 185 (2014), p. 2930. DOI: [10.1016/j.cpc.2014.06.021](https://doi.org/10.1016/j.cpc.2014.06.021). arXiv: [1112.5675 \[hep-ph\]](https://arxiv.org/abs/1112.5675).
- [115] N. Kidonakis. “Next-to-next-to-leading logarithm resummation for *s*-channel single top quark production”. In: *Phys. Rev. D* 81 (2010), p. 054028. DOI: [10.1103/PhysRevD.81.054028](https://doi.org/10.1103/PhysRevD.81.054028). arXiv: [1001.5034 \[hep-ph\]](https://arxiv.org/abs/1001.5034).
- [116] N. Kidonakis. “Next-to-next-to-leading-order collinear and soft gluon corrections for *t*-channel single top quark production”. In: *Phys. Rev. D* 83 (2011), p. 091503. DOI: [10.1103/PhysRevD.83.091503](https://doi.org/10.1103/PhysRevD.83.091503). arXiv: [1103.2792 \[hep-ph\]](https://arxiv.org/abs/1103.2792).
- [117] Nikolaos Kidonakis. “Two-loop soft anomalous dimensions for single top quark associated production with a W^- or H^- ”. In: *Phys. Rev. D* 82 (2010), p. 054018. DOI: [10.1103/PhysRevD.82.054018](https://doi.org/10.1103/PhysRevD.82.054018). arXiv: [1005.4451 \[hep-ph\]](https://arxiv.org/abs/1005.4451).
- [118] Stefano Catani et al. “Vector Boson Production at Hadron Colliders: A Fully Exclusive QCD Calculation at Next-to-Next-to-Leading Order”. In: *Phys. Rev. Lett.* 103 (2009), p. 082001. DOI: [10.1103/PhysRevLett.103.082001](https://doi.org/10.1103/PhysRevLett.103.082001). arXiv: [0903.2120 \[hep-ph\]](https://arxiv.org/abs/0903.2120).
- [119] Keith Hamilton et al. “NNLOPS simulation of Higgs boson production”. In: *JHEP* 10 (2013), p. 222. DOI: [10.1007/JHEP10\(2013\)222](https://doi.org/10.1007/JHEP10(2013)222). arXiv: [1309.0017 \[hep-ph\]](https://arxiv.org/abs/1309.0017).

- [120] Keith Hamilton, Paolo Nason, and Giulia Zanderighi. “Finite quark-mass effects in the NNLOPS POWHEG+MiNLO Higgs generator”. In: *JHEP* 05 (2015), p. 140. DOI: [10.1007/JHEP05\(2015\)140](https://doi.org/10.1007/JHEP05(2015)140). arXiv: [1501.04637 \[hep-ph\]](https://arxiv.org/abs/1501.04637).
- [121] Paolo Nason and Carlo Oleari. “NLO Higgs boson production via vector-boson fusion matched with shower in POWHEG”. In: *JHEP* 02 (2010), p. 037. DOI: [10.1007/JHEP02\(2010\)037](https://doi.org/10.1007/JHEP02(2010)037). arXiv: [0911.5299 \[hep-ph\]](https://arxiv.org/abs/0911.5299).
- [122] ATLAS Collaboration. “Measurement of the Z/γ^* boson transverse momentum distribution in pp collisions at $\sqrt{s} = 7$ TeV with the ATLAS detector”. In: *JHEP* 09 (2014), p. 145. DOI: [10.1007/JHEP09\(2014\)145](https://doi.org/10.1007/JHEP09(2014)145). arXiv: [1406.3660 \[hep-ex\]](https://arxiv.org/abs/1406.3660).
- [123] J. Pumplin et al. “New Generation of Parton Distributions with Uncertainties from Global QCD Analysis”. In: *JHEP* 07 (2002), p. 012. DOI: [10.1088/1126-6708/2002/07/012](https://doi.org/10.1088/1126-6708/2002/07/012). arXiv: [hep-ph/0201195 \[hep-ph\]](https://arxiv.org/abs/hep-ph/0201195).
- [124] D. de Florian et al. “Handbook of LHC Higgs Cross Sections: 4. Deciphering the Nature of the Higgs Sector”. In: (2016). DOI: [10.23731/CYRM-2017-002](https://doi.org/10.23731/CYRM-2017-002). arXiv: [1610.07922 \[hep-ph\]](https://arxiv.org/abs/1610.07922).
- [125] Charalampos Anastasiou et al. “High precision determination of the gluon fusion Higgs boson cross-section at the LHC”. In: *JHEP* 05 (2016), p. 058. DOI: [10.1007/JHEP05\(2016\)058](https://doi.org/10.1007/JHEP05(2016)058). arXiv: [1602.00695 \[hep-ph\]](https://arxiv.org/abs/1602.00695).
- [126] Charalampos Anastasiou et al. “Higgs Boson Gluon-Fusion Production in QCD at Three Loops”. In: *Phys. Rev. Lett.* 114 (2015), p. 212001. DOI: [10.1103/PhysRevLett.114.212001](https://doi.org/10.1103/PhysRevLett.114.212001). arXiv: [1503.06056 \[hep-ph\]](https://arxiv.org/abs/1503.06056).
- [127] Falko Dulat, Achilleas Lazopoulos, and Bernhard Mistlberger. “iHixs 2 – Inclusive Higgs cross sections”. In: *Comput. Phys. Commun.* 233 (2018), pp. 243–260. DOI: [10.1016/j.cpc.2018.06.025](https://doi.org/10.1016/j.cpc.2018.06.025). arXiv: [1802.00827 \[hep-ph\]](https://arxiv.org/abs/1802.00827).
- [128] Stefano Actis et al. “NLO electroweak corrections to Higgs boson production at hadron colliders”. In: *Phys. Lett. B* 670 (2008), pp. 12–17. DOI: [10.1016/j.physletb.2008.10.018](https://doi.org/10.1016/j.physletb.2008.10.018). arXiv: [0809.1301 \[hep-ph\]](https://arxiv.org/abs/0809.1301).
- [129] M. Ciccolini, Ansgar Denner, and S. Dittmaier. “Strong and Electroweak Corrections to the Production of Higgs + 2 Jets via Weak Interactions at the Large Hadron Collider”. In: *Phys. Rev. Lett.* 99 (2007), p. 161803. DOI: [10.1103/PhysRevLett.99.161803](https://doi.org/10.1103/PhysRevLett.99.161803). arXiv: [0707.0381 \[hep-ph\]](https://arxiv.org/abs/0707.0381).
- [130] Mariano Ciccolini, Ansgar Denner, and Stefan Dittmaier. “Electroweak and QCD corrections to Higgs production via vector-boson fusion at the CERN LHC”. In: *Phys. Rev. D* 77 (2008), p. 013002. DOI: [10.1103/PhysRevD.77.013002](https://doi.org/10.1103/PhysRevD.77.013002). arXiv: [0710.4749 \[hep-ph\]](https://arxiv.org/abs/0710.4749).

- [131] Paolo Bolzoni et al. “Higgs Boson Production via Vector-Boson Fusion at Next-to-Next-to-Leading Order in QCD”. In: *Phys. Rev. Lett.* 105 (2010), p. 011801. DOI: [10.1103/PhysRevLett.105.011801](https://doi.org/10.1103/PhysRevLett.105.011801). arXiv: [1003.4451 \[hep-ph\]](https://arxiv.org/abs/1003.4451).
- [132] M.L. Ciccolini, S. Dittmaier, and M. Krämer. “Electroweak radiative corrections to associated WH and ZH production at hadron colliders”. In: *Phys. Rev. D* 68 (2003), p. 073003. DOI: [10.1103/PhysRevD.68.073003](https://doi.org/10.1103/PhysRevD.68.073003). arXiv: [hep-ph/0306234 \[hep-ph\]](https://arxiv.org/abs/hep-ph/0306234).
- [133] Oliver Brein, Abdelhak Djouadi, and Robert Harlander. “NNLO QCD corrections to the Higgs-strahlung processes at hadron colliders”. In: *Phys. Lett. B* 579 (2004), pp. 149–156. DOI: [10.1016/j.physletb.2003.10.112](https://doi.org/10.1016/j.physletb.2003.10.112). arXiv: [hep-ph/0307206 \[hep-ph\]](https://arxiv.org/abs/hep-ph/0307206).
- [134] Giancarlo Ferrera, Massimiliano Grazzini, and Francesco Tramontano. “Associated Higgs- W -Boson Production at Hadron Colliders: A Fully Exclusive QCD Calculation at NNLO”. In: *Phys. Rev. Lett.* 107 (2011), p. 152003. DOI: [10.1103/PhysRevLett.107.152003](https://doi.org/10.1103/PhysRevLett.107.152003). arXiv: [1107.1164 \[hep-ph\]](https://arxiv.org/abs/1107.1164).
- [135] Oliver Brein et al. “Top-quark mediated effects in hadronic Higgs-Strahlung”. In: *Eur. Phys. J. C* 72 (2012), p. 1868. DOI: [10.1140/epjc/s10052-012-1868-6](https://doi.org/10.1140/epjc/s10052-012-1868-6). arXiv: [1111.0761 \[hep-ph\]](https://arxiv.org/abs/1111.0761).
- [136] Giancarlo Ferrera, Massimiliano Grazzini, and Francesco Tramontano. “Higher-order QCD effects for associated WH production and decay at the LHC”. In: *JHEP* 04 (2014), p. 039. DOI: [10.1007/JHEP04\(2014\)039](https://doi.org/10.1007/JHEP04(2014)039). arXiv: [1312.1669 \[hep-ph\]](https://arxiv.org/abs/1312.1669).
- [137] Giancarlo Ferrera, Massimiliano Grazzini, and Francesco Tramontano. “Associated ZH production at hadron colliders: The fully differential NNLO QCD calculation”. In: *Phys. Lett. B* 740 (2015), pp. 51–55. DOI: [10.1016/j.physletb.2014.11.040](https://doi.org/10.1016/j.physletb.2014.11.040). arXiv: [1407.4747 \[hep-ph\]](https://arxiv.org/abs/1407.4747).
- [138] John M. Campbell, R. Keith Ellis, and Ciaran Williams. “Associated production of a Higgs boson at NNLO”. In: *JHEP* 06 (2016), p. 179. DOI: [10.1007/JHEP06\(2016\)179](https://doi.org/10.1007/JHEP06(2016)179). arXiv: [1601.00658 \[hep-ph\]](https://arxiv.org/abs/1601.00658).
- [139] Lukas Altenkamp et al. “Gluon-induced Higgs-strahlung at next-to-leading order QCD”. In: *JHEP* 02 (2013), p. 078. DOI: [10.1007/JHEP02\(2013\)078](https://doi.org/10.1007/JHEP02(2013)078). arXiv: [1211.5015 \[hep-ph\]](https://arxiv.org/abs/1211.5015).
- [140] B. Hespel, F. Maltoni, and E. Vryonidou. “Higgs and Z boson associated production via gluon fusion in the SM and the 2HDM”. In: *JHEP* 06 (2015), p. 065. DOI: [10.1007/JHEP06\(2015\)065](https://doi.org/10.1007/JHEP06(2015)065). arXiv: [1503.01656 \[hep-ph\]](https://arxiv.org/abs/1503.01656).
- [141] Robert V. Harlander et al. “Soft gluon resummation for gluon-induced Higgs Strahlung”. In: *JHEP* 11 (2014), p. 082. DOI: [10.1007/JHEP11\(2014\)082](https://doi.org/10.1007/JHEP11(2014)082). arXiv: [1410.0217 \[hep-ph\]](https://arxiv.org/abs/1410.0217).

- [142] Robert V. Harlander, Stefan Liebler, and Tom Zirke. “Higgs Strahlung at the Large Hadron Collider in the 2-Higgs-doublet model”. In: *JHEP* 02 (2014), p. 023. DOI: [10.1007/JHEP02\(2014\)023](https://doi.org/10.1007/JHEP02(2014)023). arXiv: [1307.8122 \[hep-ph\]](https://arxiv.org/abs/1307.8122).
- [143] Oliver Brein, Robert V. Harlander, and Tom J. E. Zirke. “vh@nnlo - Higgs Strahlung at hadron colliders”. In: *Comput. Phys. Commun.* 184 (2013), pp. 998–1003. DOI: [10.1016/j.cpc.2012.11.002](https://doi.org/10.1016/j.cpc.2012.11.002). arXiv: [1210.5347 \[hep-ph\]](https://arxiv.org/abs/1210.5347).
- [144] A. Elagin et al. “A new mass reconstruction technique for resonances decaying to $\tau\tau$ ”. In: *Nucl. Instrum. Meth. A* 654 (2011), pp. 481–489. DOI: [10.1016/j.nima.2011.07.009](https://doi.org/10.1016/j.nima.2011.07.009). arXiv: [1012.4686 \[hep-ex\]](https://arxiv.org/abs/1012.4686).
- [145] Pierre Baldi et al. “Parameterized neural networks for high-energy physics”. In: *Eur. Phys. J. C* 76.5 (2016), p. 235. DOI: [10.1140/epjc/s10052-016-4099-4](https://doi.org/10.1140/epjc/s10052-016-4099-4). arXiv: [1601.07913 \[hep-ex\]](https://arxiv.org/abs/1601.07913).
- [146] François Chollet et al. *Keras*. <https://keras.io>. 2015.
- [147] Martin Abadi et al. *TensorFlow: Large-Scale Machine Learning on Heterogeneous Systems*. Software available from tensorflow.org. 2015. URL: <https://www.tensorflow.org/>.
- [148] ATLAS Collaboration. “Evidence for the Higgs-boson Yukawa coupling to tau leptons with the ATLAS detector”. In: *JHEP* 04 (2015), p. 117. DOI: [10.1007/JHEP04\(2015\)117](https://doi.org/10.1007/JHEP04(2015)117). arXiv: [1501.04943 \[hep-ex\]](https://arxiv.org/abs/1501.04943).
- [149] Ian Goodfellow, Yoshua Bengio, and Aaron Courville. *Deep Learning*. <http://www.deeplearningbook.org>. MIT Press, 2016.

Appendix A

Supplementary material for c jet calibration

A.1 Additional plots for kinematic variables

A.1.1 Standard selection

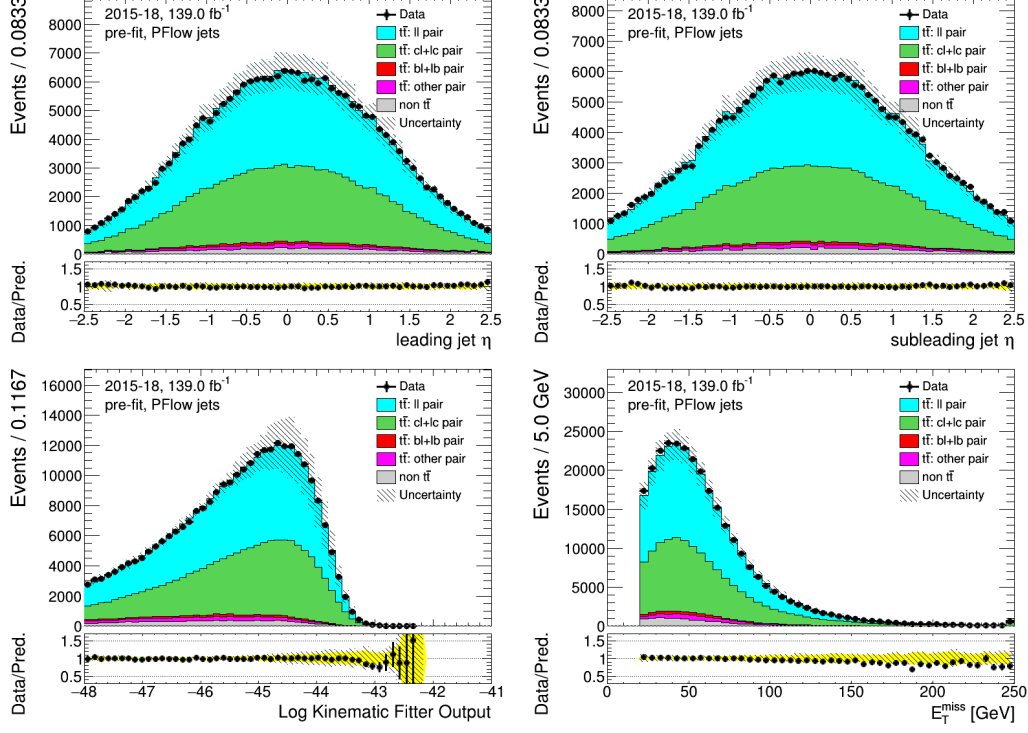


Figure A.1: PFFlow jets: distributions of the leading and sub-leading jets from W decay, KL Fitter output and the transverse missing transverse energy of the standard selection, before fitting or tagging with full uncertainties.

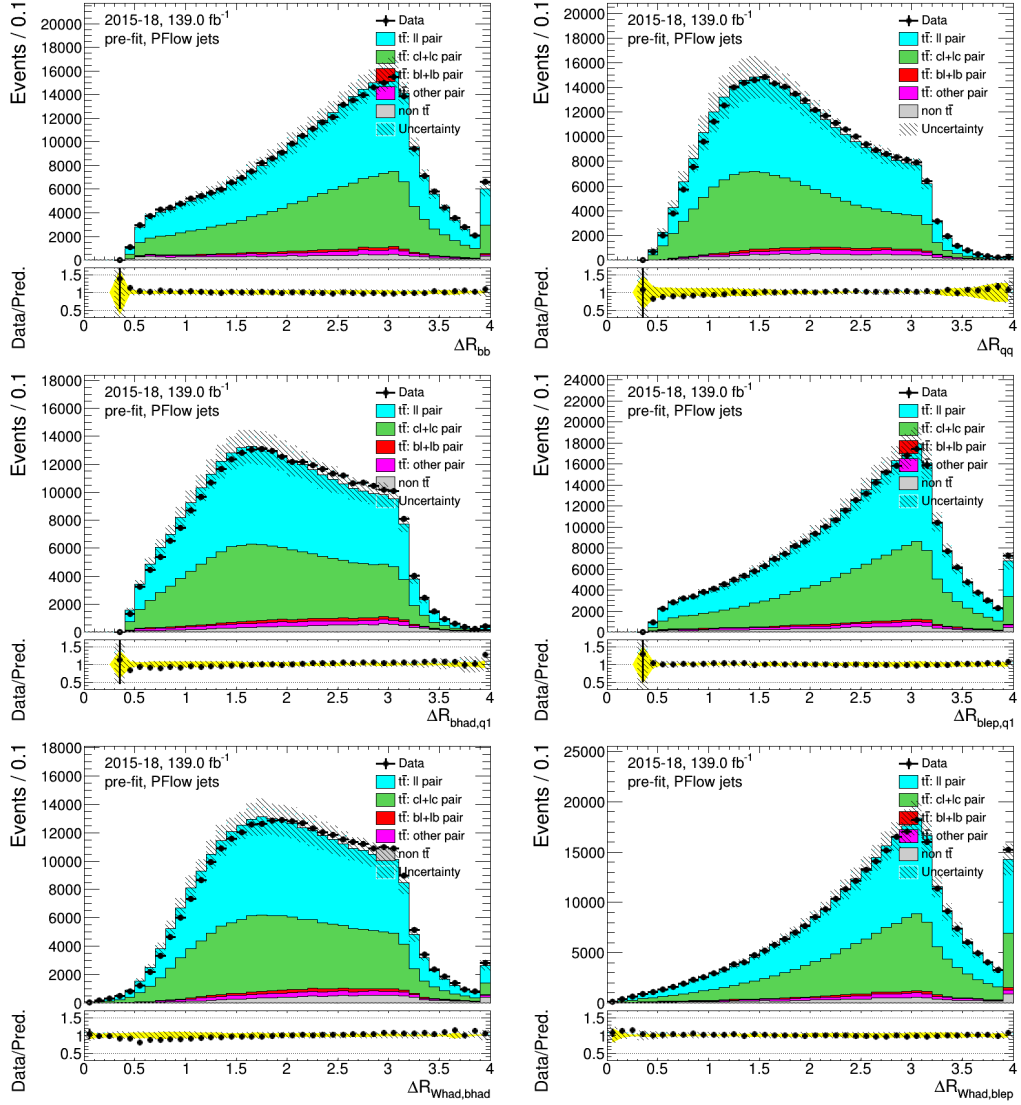


Figure A.2: PFlow jets: distributions of angle related variables of the combination of the standard selection, before fitting or tagging with full uncertainties.

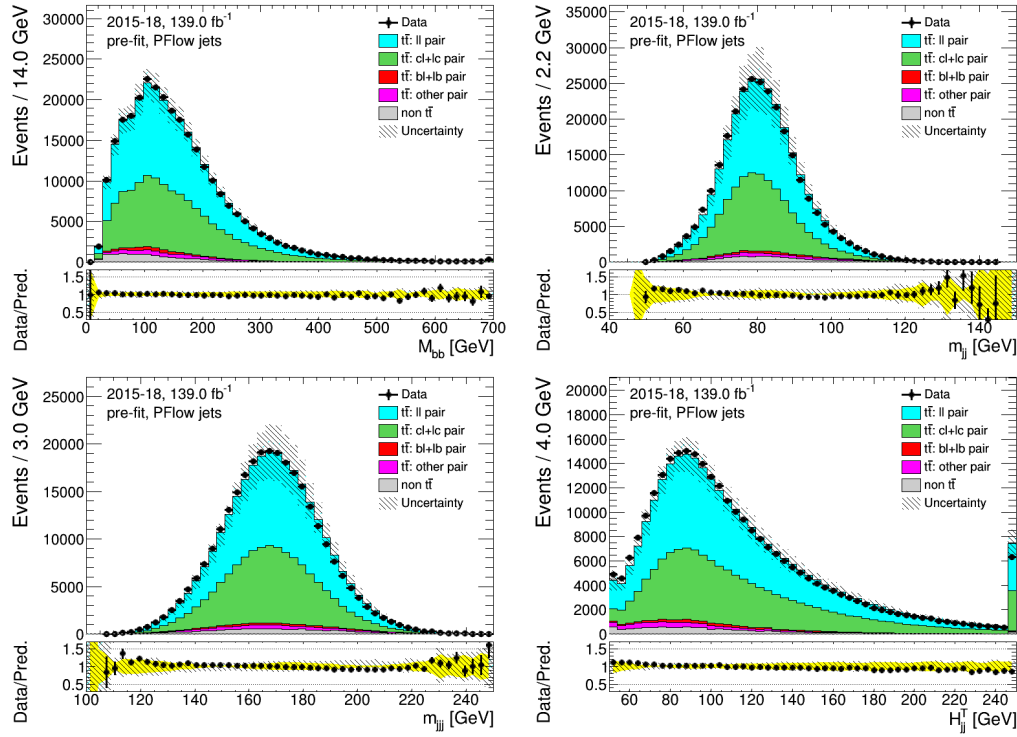


Figure A.3: PFflow jets: distributions of mass related variables of the standard selection, before fitting or tagging with stat-only uncertainties.

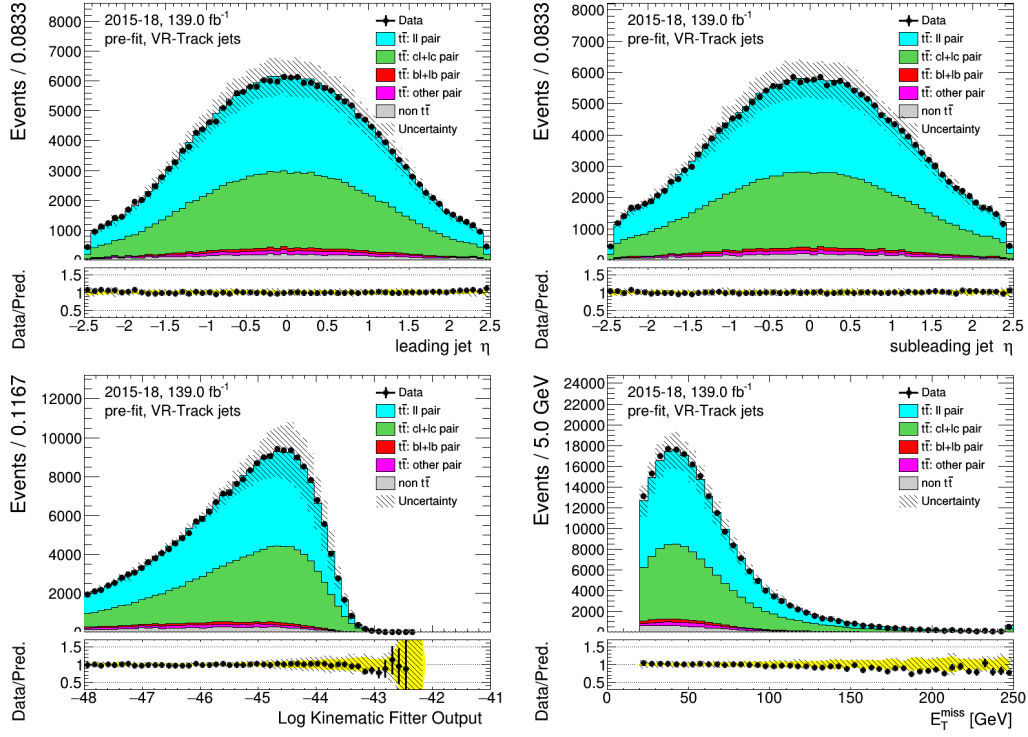


Figure A.4: VR-Track jets: distributions of the leading and sub-leading jets from W decay, KLFitter output and the transverse missing transverse energy of the standard selection, before fitting or tagging with full uncertainties.

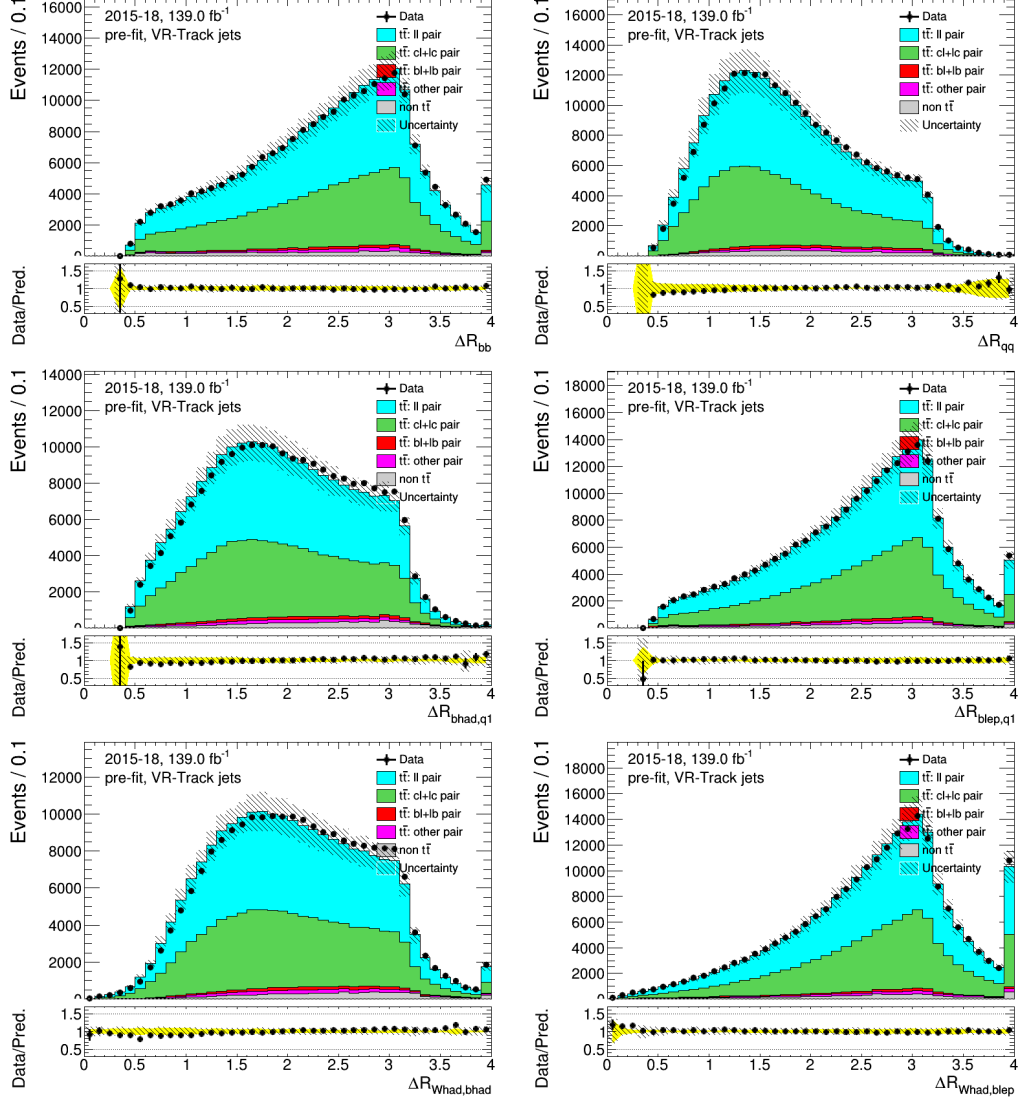


Figure A.5: VR-Track jets: distributions of angle related variables of the combination of the standard selection, before fitting or tagging with full uncertainties.

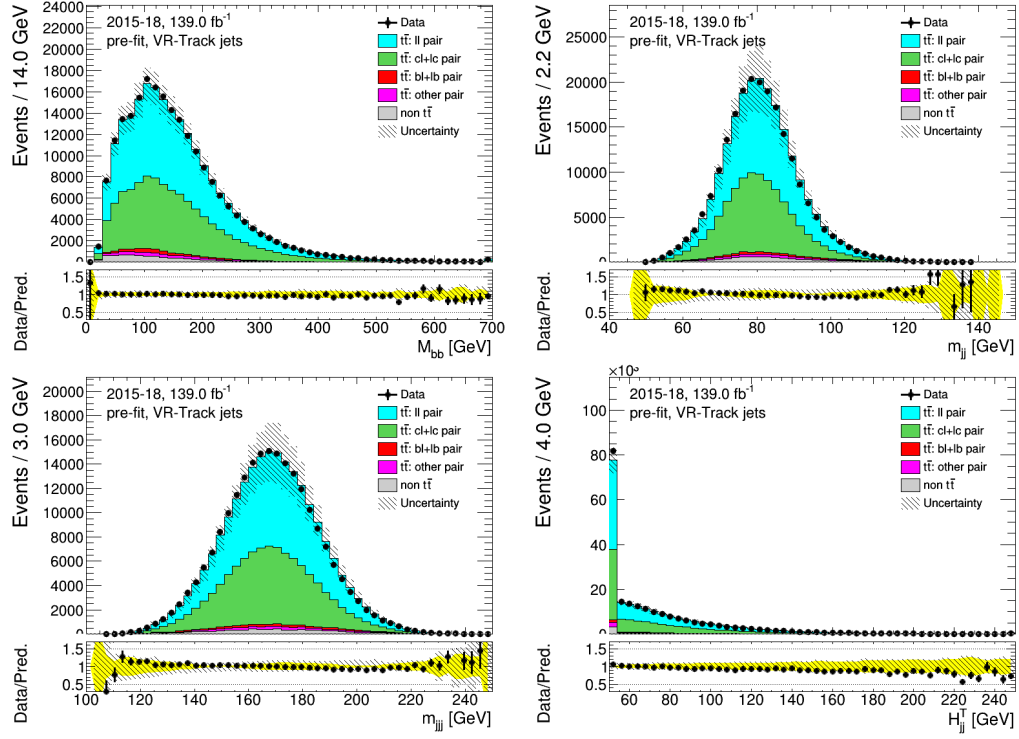


Figure A.6: VR-Track jets: distributions of mass related variables of the standard selection, before fitting or tagging with stat-only uncertainties.

A.1.2 Low- p_T selection

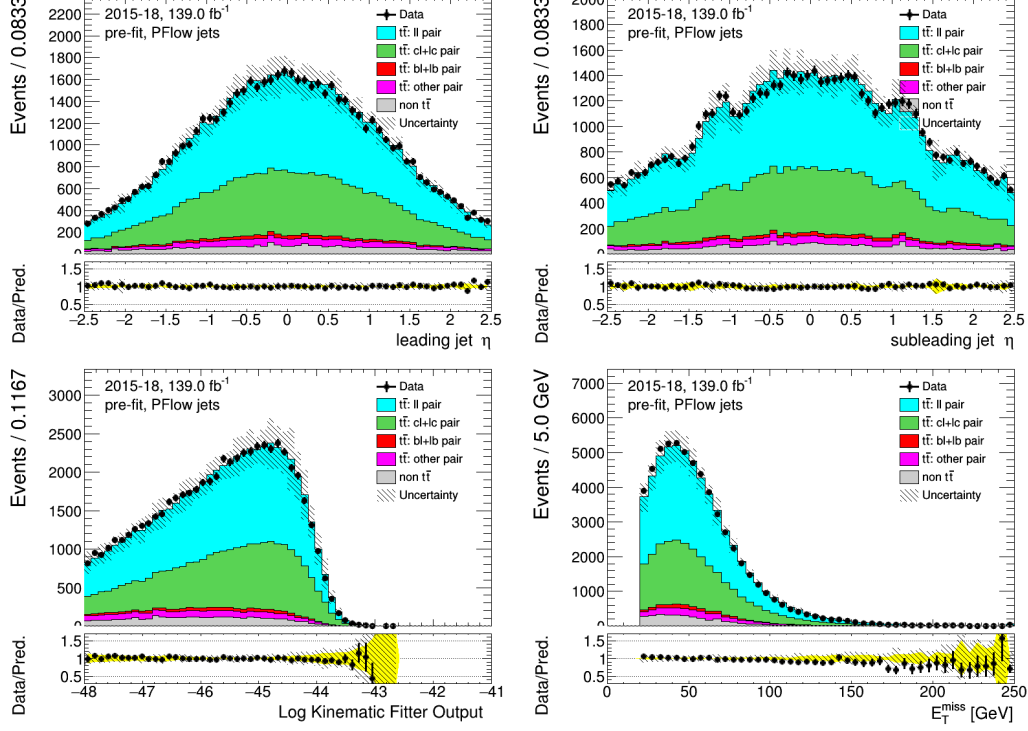


Figure A.7: PFFlow jets: distributions of the leading and sub-leading jets from W decay, KL Fitter output and the transverse missing transverse energy of the low- p_T selection, before fitting or tagging with full uncertainties.

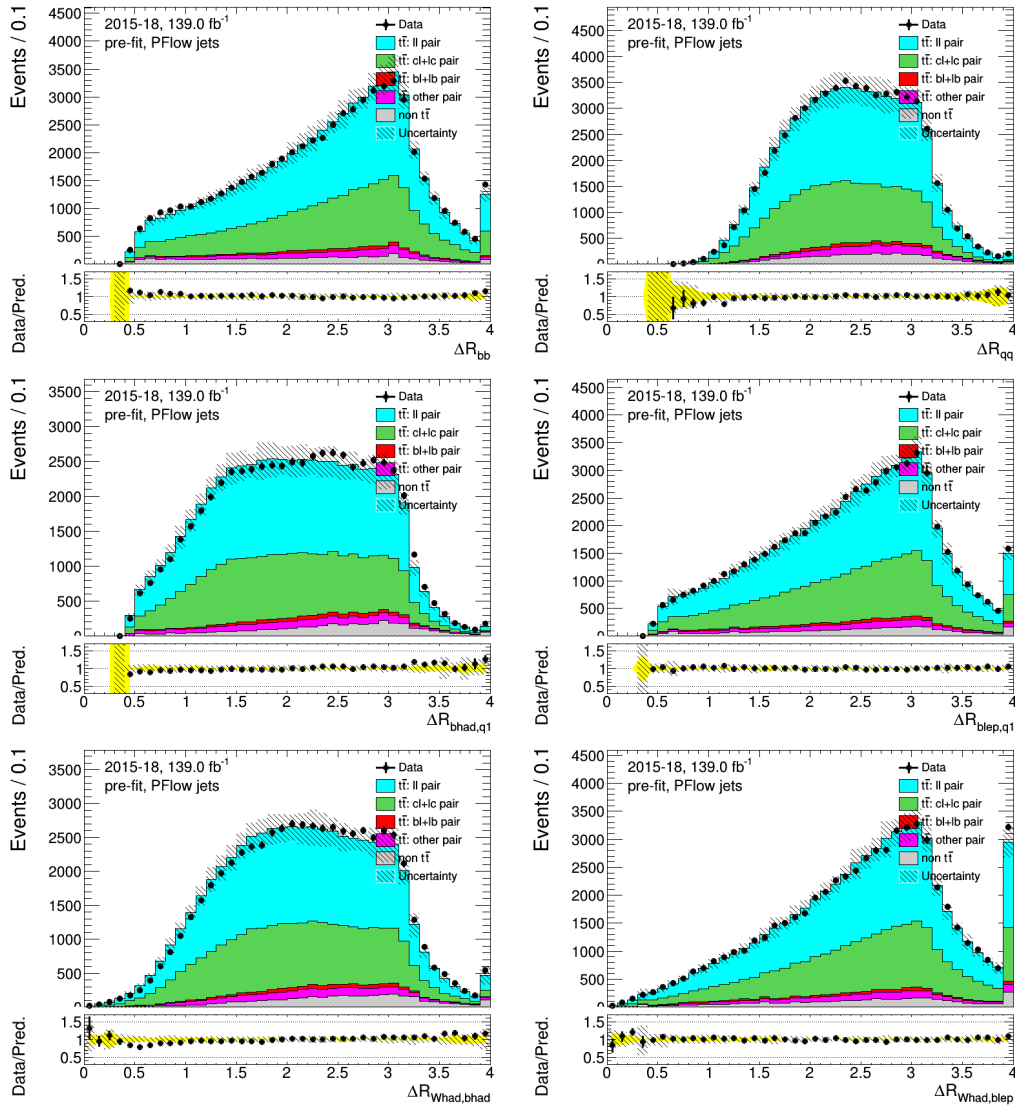


Figure A.8: PFlow jets: distributions of angle related variables of the combination of the low- p_T selection, before fitting or tagging with full uncertainties.

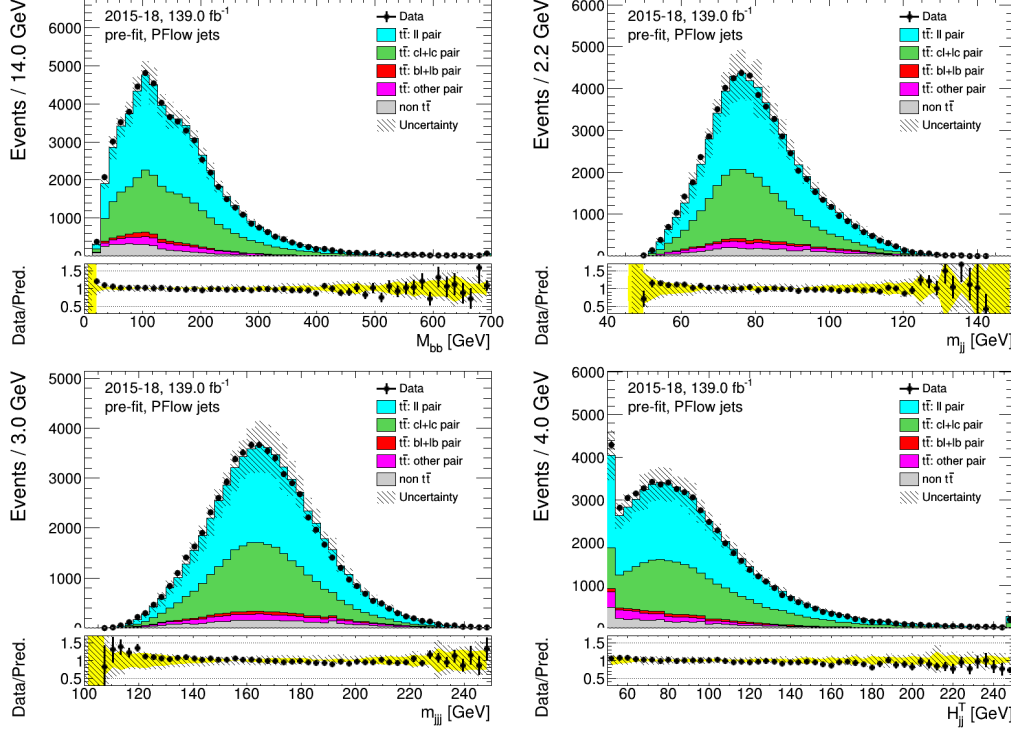


Figure A.9: PFlow jets: distributions of mass related variables of the low- p_T selection, before fitting or tagging with stat-only uncertainties.

A.2 High- p_T selection

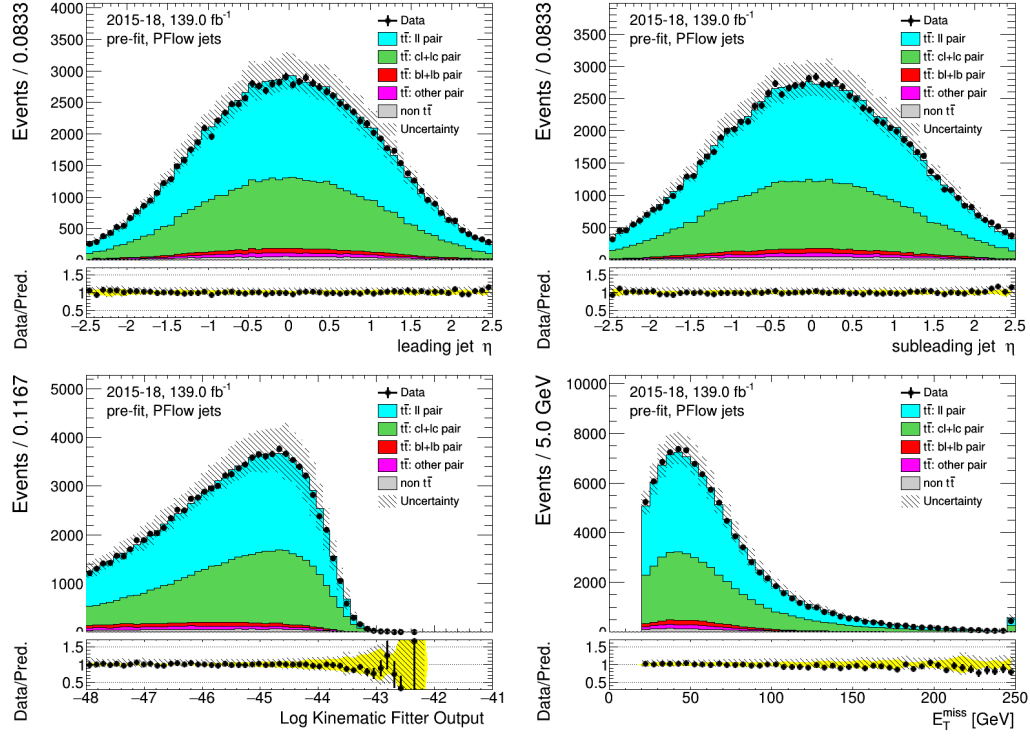


Figure A.10: PFlow jets: distributions of the leading and sub-leading jets from W decay, KLFit output and the transverse missing transverse energy of the high- p_T selection, before fitting or tagging with full uncertainties.

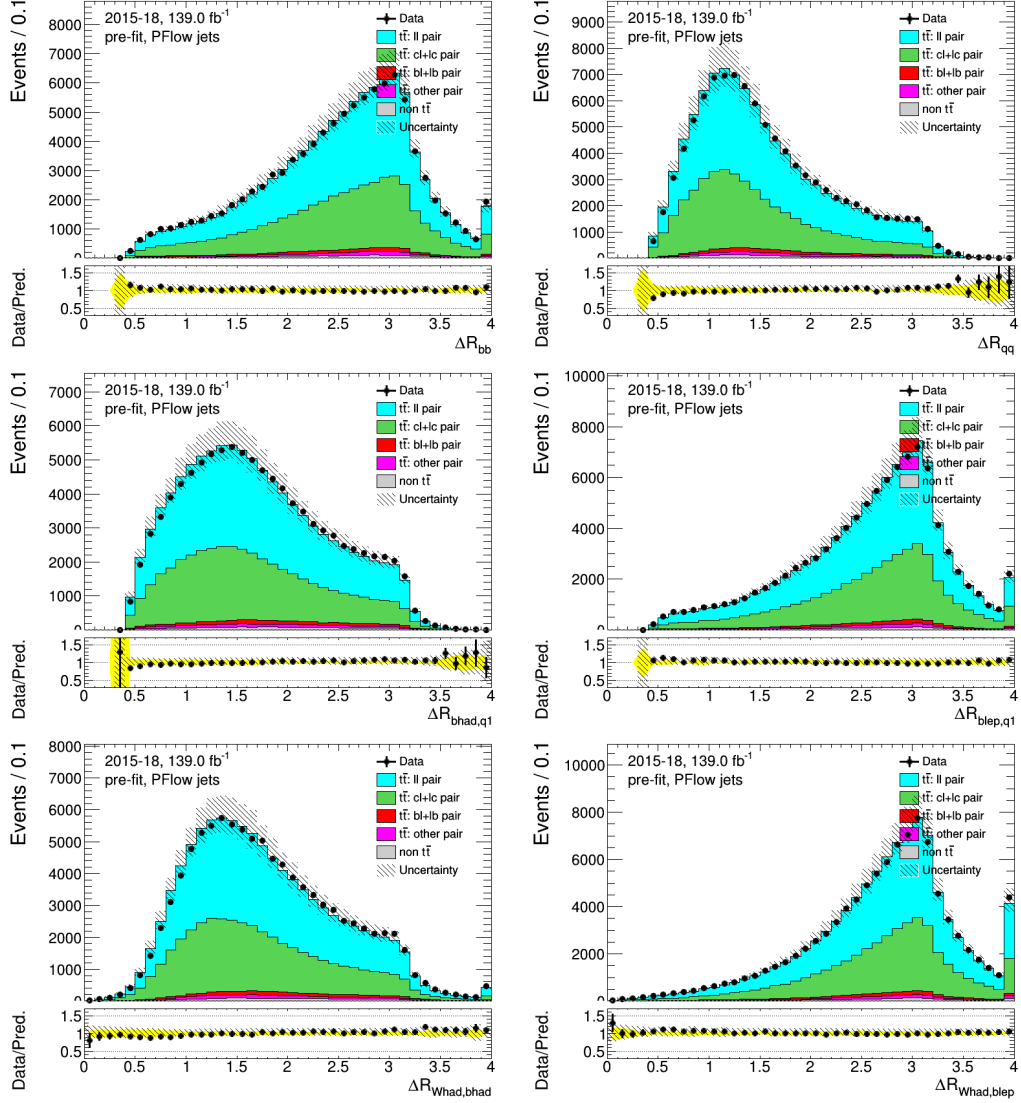


Figure A.11: PFlow jets: distributions of angle related variables of the combination of the high- p_T selection, before fitting or tagging with full uncertainties.

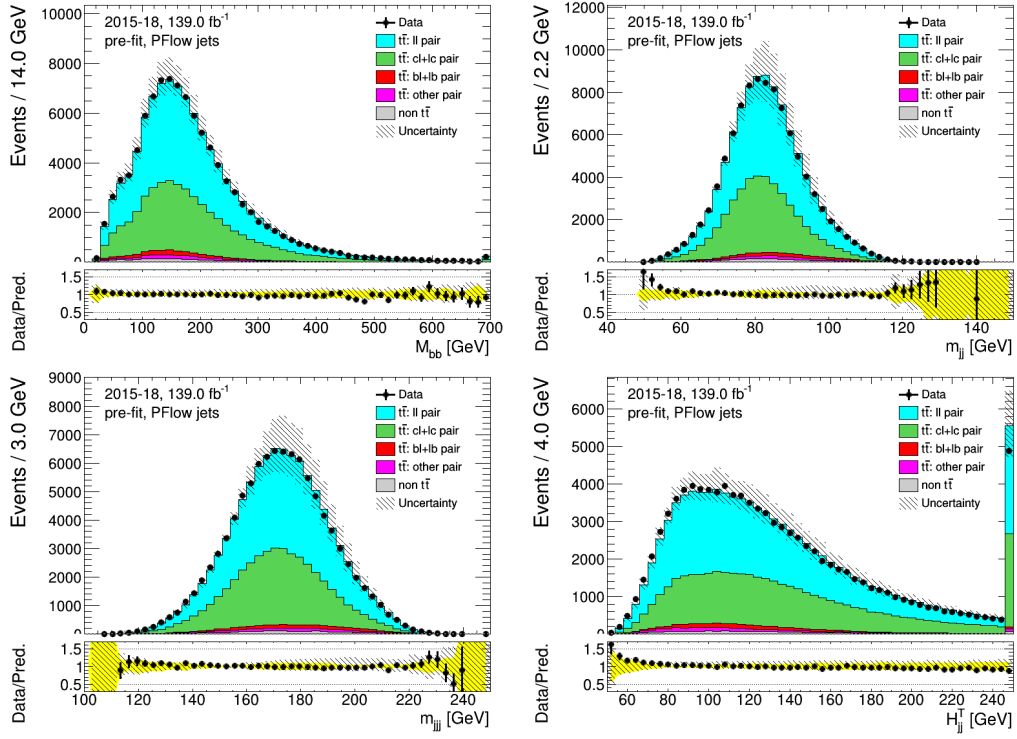


Figure A.12: PFflow jets: distributions of mass related variables of the high- p_T selection, before fitting or tagging with stat-only uncertainties.

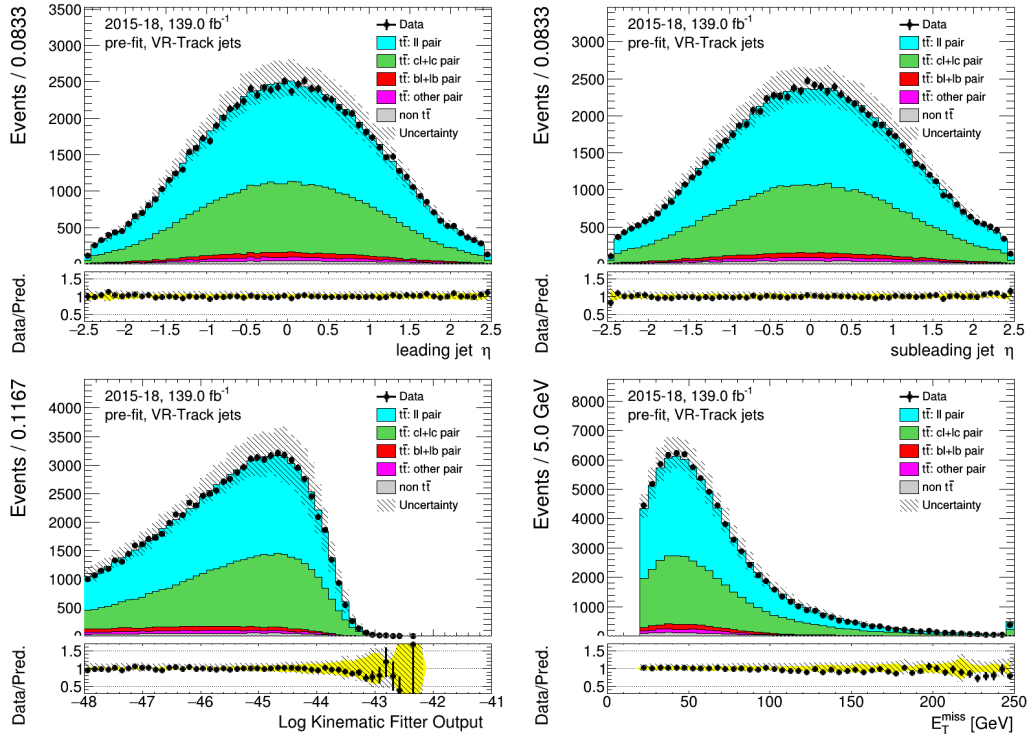


Figure A.13: VR-Track jets: distributions of the leading and sub-leading jets from W decay, KL Fitter output and the transverse missing transverse energy of the high- p_T selection, before fitting or tagging with full uncertainties.

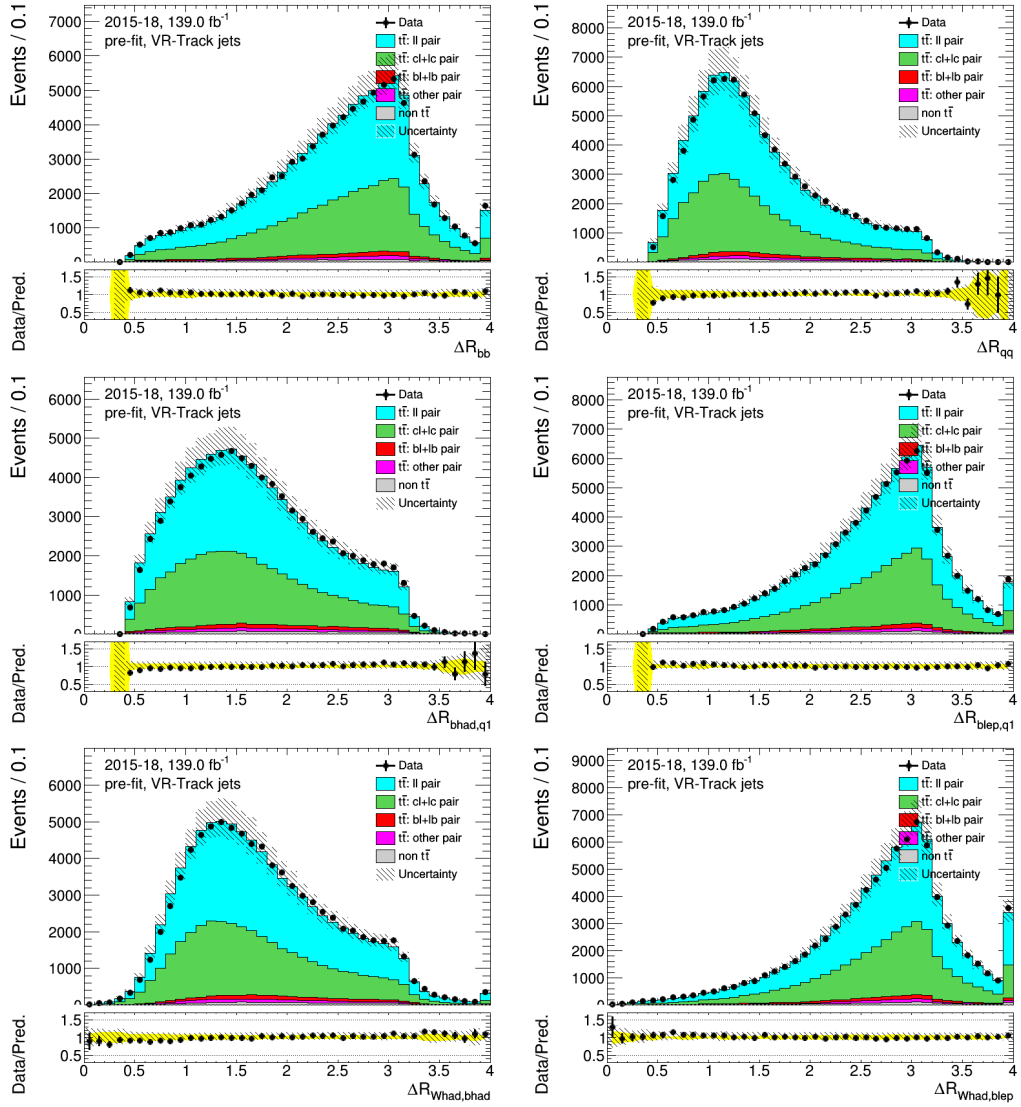


Figure A.14: VR-Track jets: distributions of angle related variables of the combination of the high- p_T selection, before fitting or tagging with full uncertainties.

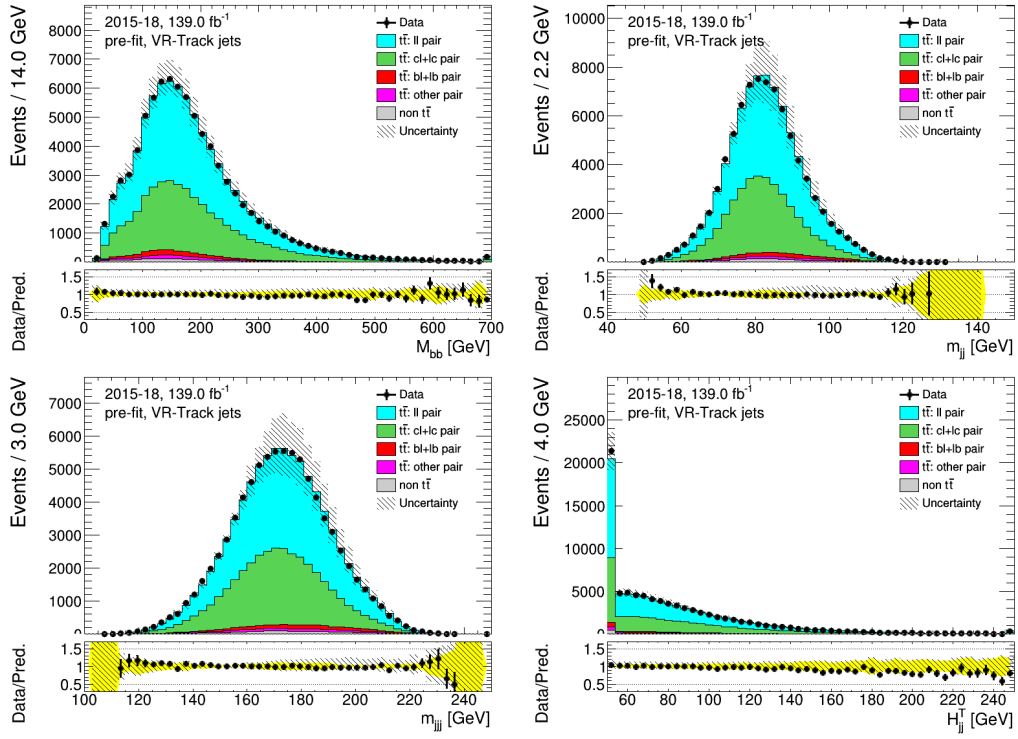


Figure A.15: VR-Track jets: distributions of mass related variables of the high- p_T selection, before fitting or tagging with stat-only uncertainties.

A.3 Combined selection

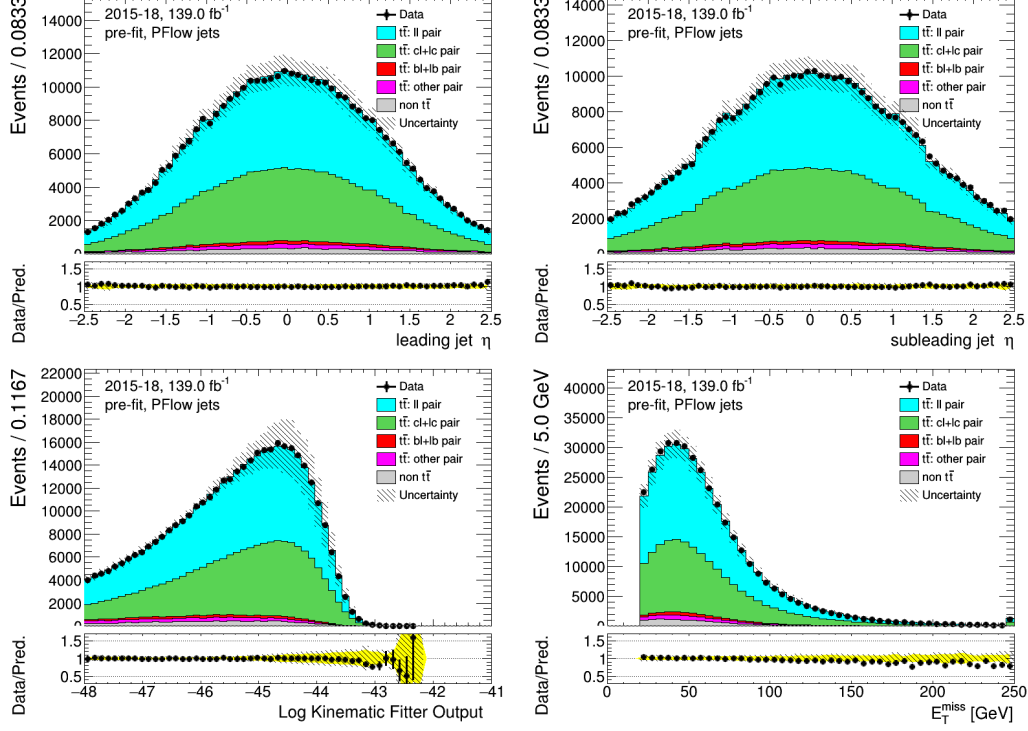


Figure A.16: PFlow jets: distributions of the leading and sub-leading jets from W decay, KL Fitter output and the transverse missing transverse energy of the combined selection, before fitting or tagging with full uncertainties.

Chapter. A

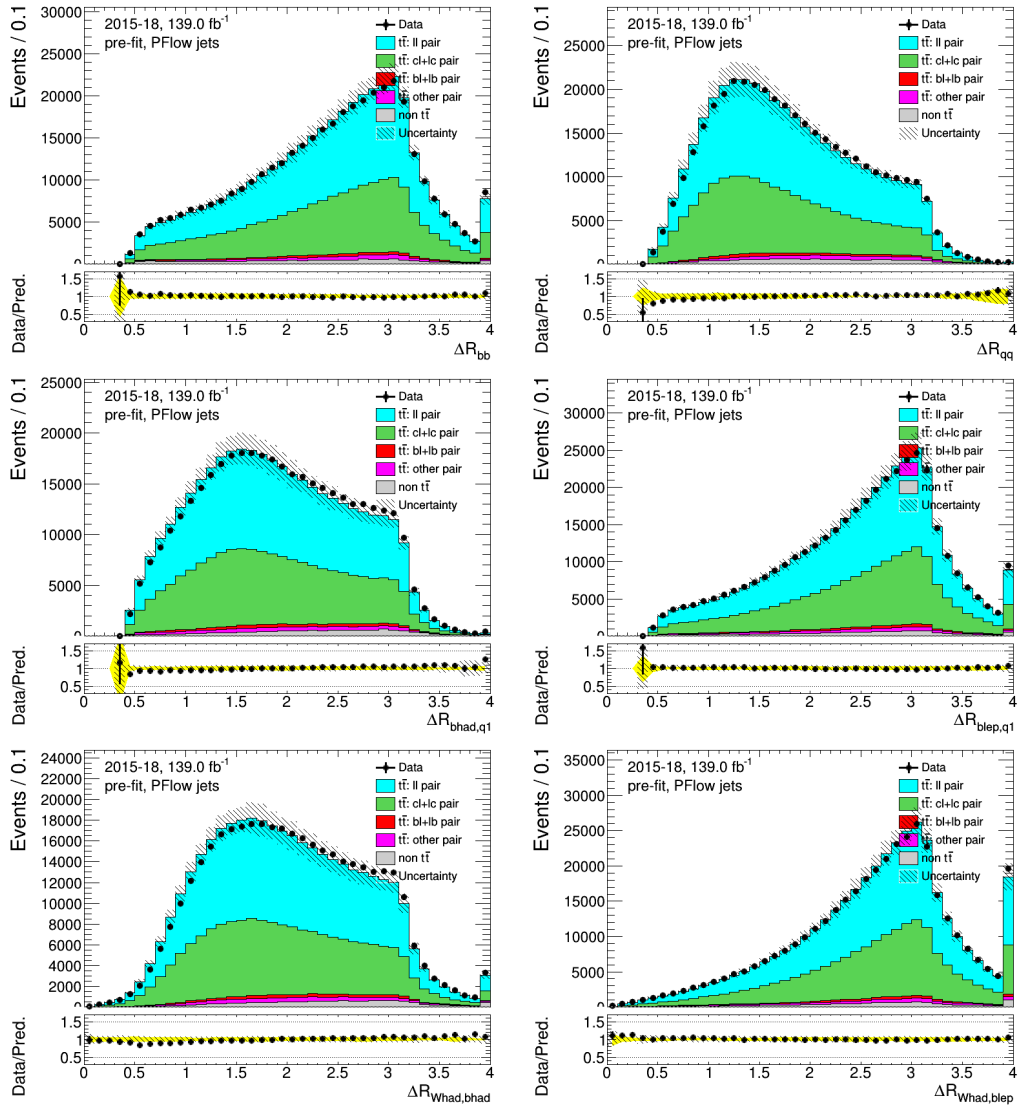


Figure A.17: PFlow jets: distributions of angle related variables of the combination of the combined selection, before fitting or tagging with full uncertainties.

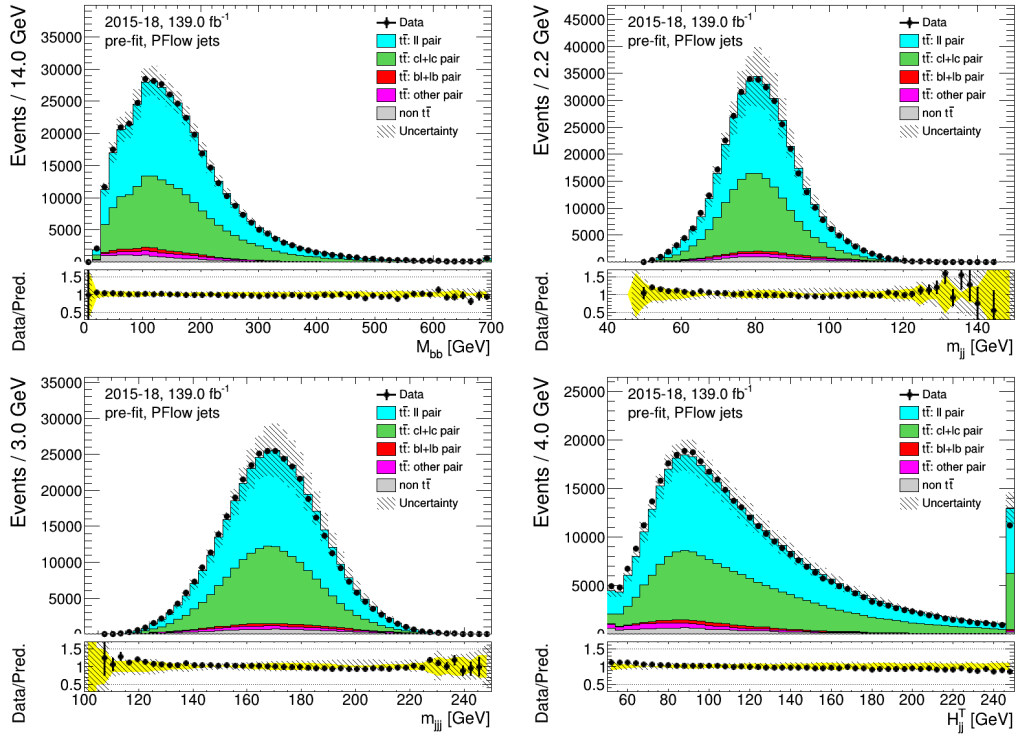


Figure A.18: PFlow jets: distributions of mass related variables of the combined selection, before fitting or tagging with stat-only uncertainties.

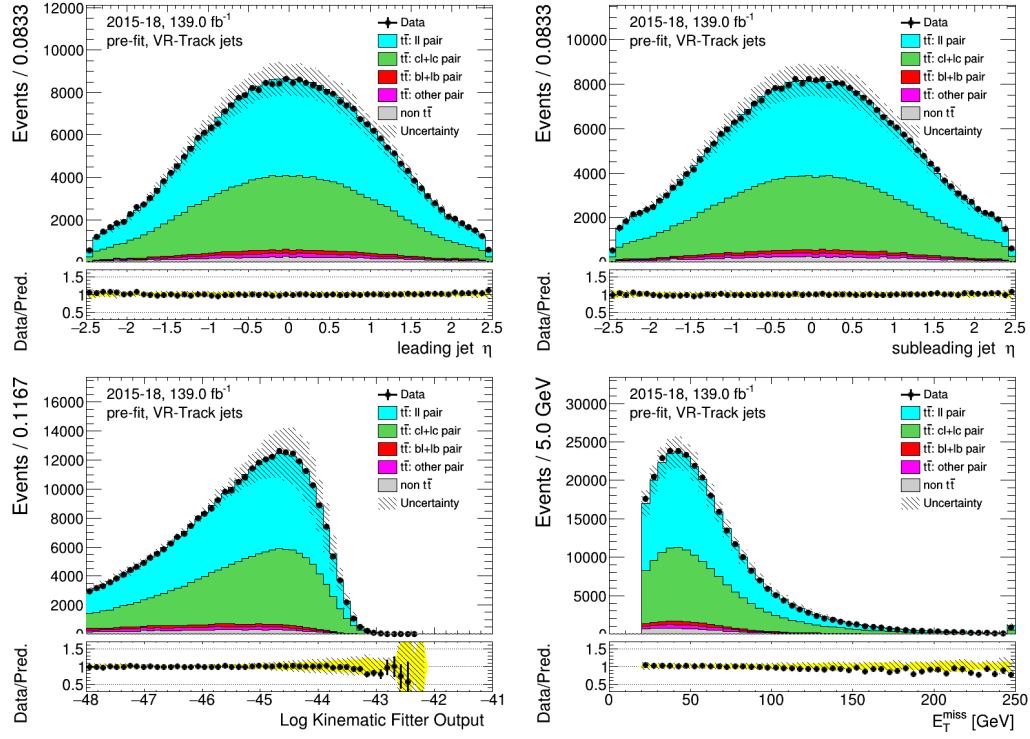


Figure A.19: VR-Track jets: distributions of the leading and sub-leading jets from W decay, KLFitter output and the transverse missing transverse energy of the combined selection, before fitting or tagging with full uncertainties.

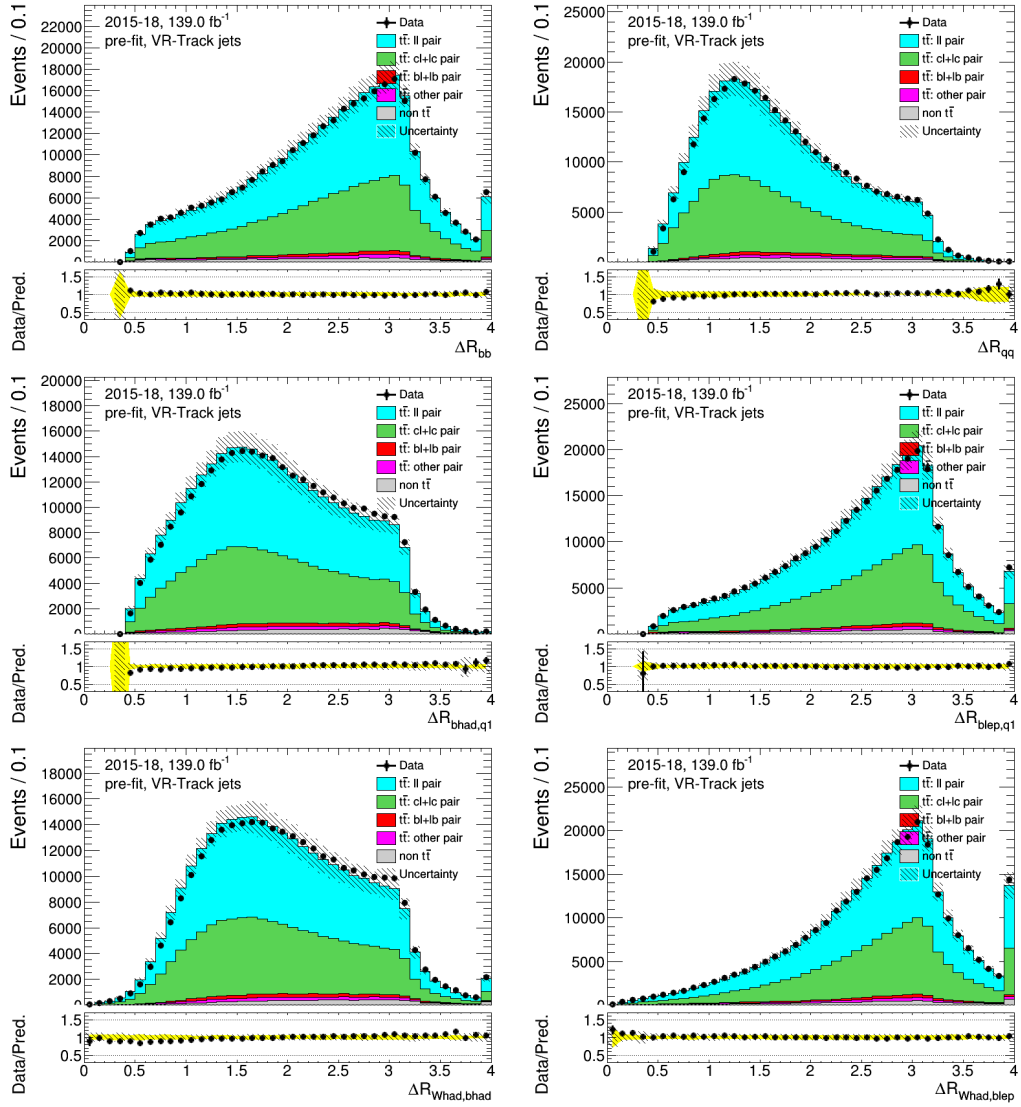


Figure A.20: VR-Track jets: distributions of angle related variables of the combination of the combined selection, before fitting or tagging with full uncertainties.

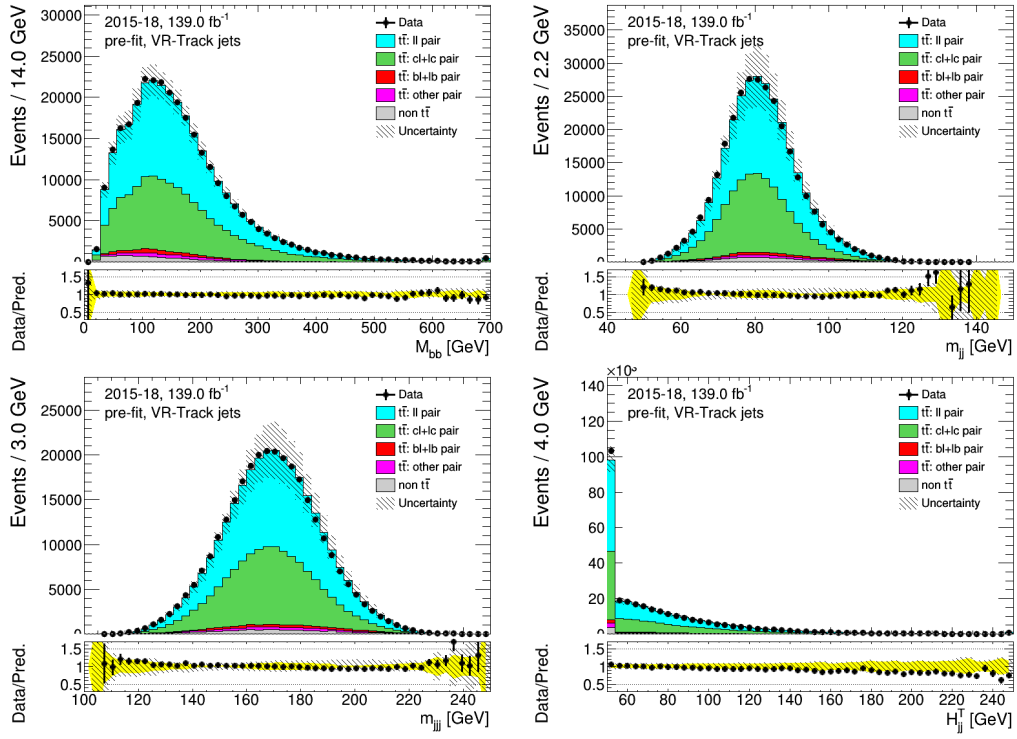


Figure A.21: VR-Track jets: distributions of mass related variables of the combined selection, before fitting or tagging with stat-only uncertainties.

A.4 Experimental uncertainties

Systematic uncertainty
EG_RESOLUTION_ALL
MUON_ID
MUON_MS
MET_SoftTrk_ResoPara
MET_SoftTrk_ResoPerp
MET_SoftTrk_ScaleDown
MET_SoftTrk_ScaleUp
JET_Pileup_OffsetNPV
JET_Pileup_RhoTopology
JET_EffectiveNP_Modelling1
JET_EffectiveNP_Modelling2
JET_EffectiveNP_Modelling3
JET_EffectiveNP_Modelling4
JET_EffectiveNP_Statistical4
JET_EffectiveNP_Detector1
JET_JER_EffectiveNP_1
JET_JER_EffectiveNP_2
JET_JER_EffectiveNP_3
JET_JER_EffectiveNP_4
JET_BJES_Response
JET_Flavor_Composition
JET_Flavor_Response

Table A.1: List of experimental systematics.